INTERNATIONAL ATOMIC ENERGY AGENCY
UNITED NATIONS EDUCATIONAL, SCIENTIFIC AND CULTURAL ORGANIZATION

INTERNATIONAL CENTRE FOR THEORETICAL PHYSICS
34100 TRIESTE (ITALY) - P.O.B. 586 - MIRAMARE - STRADA COSTIERA 11 - TELEPHONE: 2240-1
CABLE: CENTRATOM - TELEX 460392 - 1

LIBRARY

IC/87/128

WINTER COLLEGE ON

ATOMIC AND MOLECULAR PHYSICS

(9 March - 3 April 1987)

SOME APPLICATIONS OF PHOTOACOUSTIC AND RELATED SENSING METHODS RELEVANT TO AGRICULTURE IN GENERAL

D. Bicanic

Agricultural University
Wageningen
The Netherlands

SOME APPLICATIONS OF PHOTOACOUSTIC AND RELATED SENSING METHODS

RELEVANT TO AGRICULTURE IN GENERAL

Syllabus

UNESCO - IAEA Winter College on Atomic and Molecular Physics 1987

International Centre for Theoretical Physics

Trieste, Italy

by

Dane Bicanic

Agricultural University Wageningen
The Netherlands

CONTENTS

PREFACE

This syllabus has been prepared for the participants of the Winter College on Atomic and Molecular Physics organized by UNESCO and the International Atomic Energy Agency at the International Centre for Theoretical Physics in Trieste (Italy) from March 9 to April 3, 1987. Primarily it deals with the topics of photoacoustic and other related phenomena as well as with the (possible) use of these in the field of agriculture (in a very broad sense). Several excellent books and reviews on this matter have been published or are due to appear in the immediate future, as a result of the steadily growing interest for this subject. This volume is intended for those new in the field, and its content might also be useful either as a reference source or as a guide when setting up future experiments in the home countries.

Some parts of the lecture material described here are based on the results obtained by (or in conjunction with) other research colleagues from various institutes in and outside the Netherlands.

I wish to thank F. Harren, J. Reuss, C. Sikkens, F. van Rijn, E. Dicker (Catholic University Nijmegen), employees of the mechanical and electronic workshop of our department, S. Krüger (Krups Elektronik GmbH Bremen), E. Woltering (Sprenger Institute Wageningen), M. Posthumus, J. Mooi (Research Institute for Plant Protection), B. Rein (Ruhruniversität Hochum), M. Sigrist, S. Bernegger (ETH Swiss Federal Institute Zürich), F. Schiet (John Pierce Foundation, Yale University New Haven), J. Gelbawchs, S. Beck, G. Loper (Aerospace Research Corp., Los Angeles), D. Cahen, O. Canaani (Weizmann Institute of Science Rehovot), F. Lepoutre, J. Poulet (L'École Superièure pour Physique et Chimie Industrielle, Paris), B. Zuidberg (Gadjah Mada University Yogyakarta), A. Rizzarri (Universita di Roma), A. van Es, K. Hartmann (IBvL Wageningen) and V. Zharov, S. Lethokov (Moscow University) for making their data available.

My gratitude is to Mrs. J. Zeevat-van Homelen of the Department of Text Processing at the Agricultural University Wageningen, who meticulously took care of both the language and manuscript, which was typed in a record tempo.
Mr. P. van Espelo and Mr. L. Hendriks deserve the credit for the drawing and layout.
Finally thanks to the International Agricultural Centre Wageningen, Stichting Technische Wetenschappen Amsterdam, Catholic University Nijmegen, and the Agricultural University Wageningen, through whose fellowships and funding much of the work described here was made possible.

Wageningen, March 1987,

Dane Bicanic
Department of Physics and Meteorology
Agricultural University
Wageningen
The Netherlands

I PHOTOACOUSTICS IN A GAS PHASE

I.1 Basic concepts

Heating of the sample resulting in the irradiation and absorption of the modulation excitation energetic beam, gives rise to a variety of what is commonly called the photothermal effects. Some of these examples are the temperature rise (calorimetry), the production of thermal refractive index gradient in the medium (that consequently affects its own propagation, resulting in the thermal blooming or defocussing of the beam), the surface distortion and hence displacement and finally the photothermal radiometry (Fig. 1). The heating, call it photothermal heating, enables one through the use of the four mechanisms described above, to obtain, among other, the information about optical and thermal properties of the sample, hence the term photothermal spectroscopy.

There are three general classes of applications of the photoacoustics and the related above mentioned methods i.e. one spectroscopic, and the two non-spectroscopic ones (Figure 2). In the photoacoustic spectroscopy (box 1) the wavelength of the excitation source is varied while maintaining the other parameters as a constant (branching ratio, efficiency of heat and acoustic generation etc.). The recorder spectrum contains the information about the sample's absorption properties.
In addition to the heat generation (fast) there are other (slow) non-radiative processes (box 2) (such as luminescence, photochemistry, photoelectricity etc.) which compete with thermal decaying. Consequently, the photoacoustics can be used to monitor complementary relaxation channels. For example, when two mechanisms dominate (say collisional deexcitation and the luminescence) then monitoring of thermal channels will provide relevant data on luminescence. Probing of thermal (diffusivity, effusivity) and of other physical properties (phase change, thickness of layers, subsurface imaging) forms the second (box 3) class out of the group of the non-spectroscopic applications. Probing is achieved through what is called the

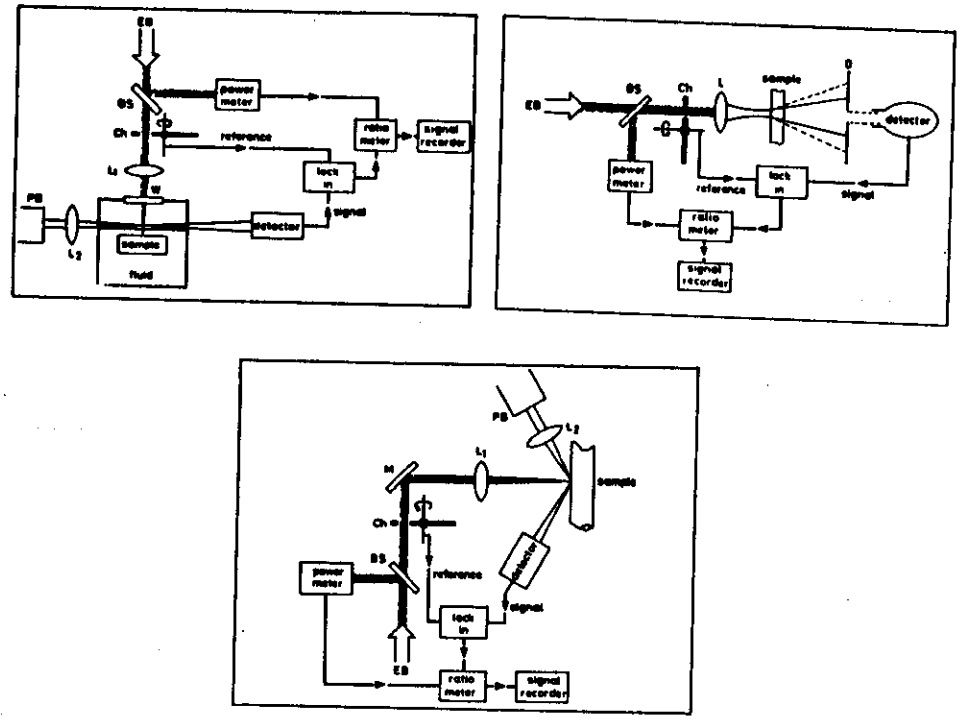

Figuur 1. Various photothermal techniques (1).

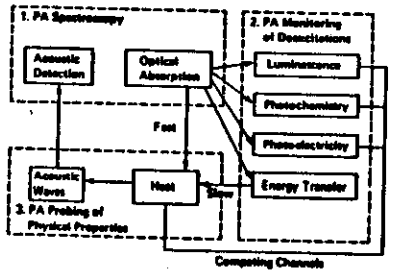

Figure 2. Three classes of applications of photoacoustic sensing (2).

frequency domain photoacoustics (or photoacoustic calorimetry) by varying the modulation frequency at the fixed excitation wavelength.

The oldest and most widespread member in the class of photothermal effects is that of photoacoustics. Besides the spectroscopic applications, the effect forms the base for investigation of specific non-radiative de-excitation processes as well as for the efficient probing of physical properties. The photoacoustic effect is in fact the generation of acoustic waves due to the deposition of heat in the sample following the absorption of energy. It was discovered in 1881 by A.G. Bell on solids, and soon after conformed by Tyndall and Röntgen on aqueous and liquid samples. In Figure 3 an early photoacoustic experiment is shown - the modulated radiation from the sun was directed into a small vessel containing, for example, a gaseous sample that is absorbing in the infra-red. Bell and contemporaries listened, by means of a stethoscope, to the the interior of the vessel and perceived the feeble sound production at a frequency that corresponded to the modulated frequency. The intensity of the sound varied from sample to sample; in certain cases the combined effect of using a vessel of specific dimensions and the modulation frequency led to production of sound that could be heard at greater distances!

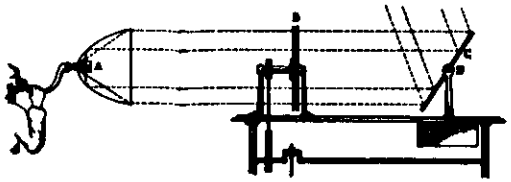

Figure 3. Early photoacoustic detector (3).

Nowadays it is understood that the optically induced sound production results from the absorption of the infra-red portion of the energy provided by the sun. Following the absorption of energy, the gas molecules from the

ground vibrational state are excited into a rotational level in the higher vibrational state and de-excitation processes will then redistribute the energy through various mechanisms (Fig. 4).

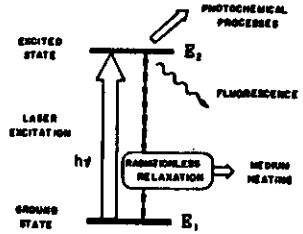

Figure 4. Redistribution of energy on absorption of radiation from the excitation beam. Radiationless relaxation gives rise to a photoacoustic signal (4).

In the infra-red region the probability for radiative decay (proportional with the third power of the absorption frequency) is small. Low quantum efficiency creates a situation in which the relaxation takes place along the non-radiative channel. For the majority of molecules the relaxation time is fast (in the order of μs) as the atmospheric pressure and the rotational translational de-exitation through collisions prevails. It causes the increase of kinetic energy of gas molecules and hence gas temperature. Consequently, in a vessel of constant volume, increase of temperature leads to the corresponding pressure increase. Thus, when the radiation source providing the allowed energy for the sample is modulated at audio frequency f_m, generated pressure fluctuations will be modulated at the same frequency. The sound wave has a phase delay with respect to the excitation beam (Figure 5) and can be detected by a transducer located in the gaseous sample. Of course, τ_m the inverse of the modulation frequency f_m must be longer than the collisional relaxation time τ_C, and the dimension of the vessel has to be so chosen that thermal diffusion to the wall (loss mechanism) characterized by the relevant time interval τ_T is not dominant.

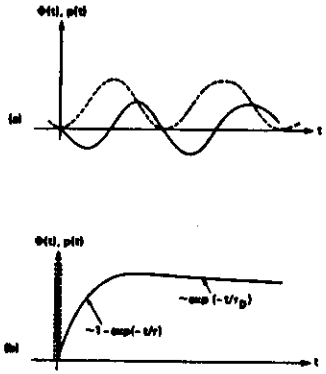

Figure 5. The sound wave (full line) p(t) has a phase delay with respect to excitation wave (dotted line) continuous mode (a) and pulsed (b) mode (2).

It is obvious, that photoacoustic effect provides the method by which the degree to which the sample has been heated on account of absorbing the radiation from the exciting beam can be measured by detecting the acoustical signals (5).

The magnitude of the generated signal is proportional to the number of absorbing molecules and the amount of power absorbed by the gas. In principle, regardless of what the excitation beam consists of (electromagnetic radiation from very short to very long wavelengths, charged particles or other) the detection principle remains the same.

Fifty years after Bell's discovery, the almost forgotten photoaccustic effect found its first application, when Viengerov constructed the spectrophone an instrument to acoustically record the spectra and later also performed the first concentration measurement. But the real revival of interest for photoacoustics was brought on by the advent of the laser. Soon after Kerr and Atwood demonstrated the usability of the laser to acoustically record the weak spectra of water vapour (6), Kreuzer used the low power He-Ne laser to investigate the methane-nitrogen mixtures in various concentrations (7). Thus, when the high power laser emitting collimated

and monochromatic light is used as the source, the photacoustic method becomes, in principle, comparable or even superior to other spectroscopic techniques. No wonder that a true upsurge of worldwide interest has been noticed in the last decade, in particular for quantitizing ultra-weak absorptions of the atmospheric and industrial pollutants. The usability of laser as the excitation source triggered much, both experimental and theoretical work, and led to numerous novel applications of this (and related) technique(s) in agriculture, medical and other life sciences, process engineering and areas of natural sciences. Four topical international conferences have already been held, the fifth one is due in Heidelberg, West Germany this summer. Excellent review articles have been written in the last few years and several books on (laser) photoacoustic spectroscopy have been or are to be published in the near future (2, 4, 8, 9, 10, 11, 11A). This contribution is only an attempt to emphasize a few specific applications of the photoacoustic spectroscopy in environmental and agricultural practice. Some theoretical background of the signal generation in gases will be given first, followed by the description and analysis of performance characteristics of the instrumental equipment needed. We will proceed with a brief review of photoacoustics for measuring absorptions in liquids and illustrate its usability in determining absorption coefficients of some strongly absorbing organic liquid. Finally basic principles of photoacoustic spectroscopy on solid samples are presented and applied to determine the thermal effusivity of glasses used as cover construction material in greenhouses.

What is the amplitude of the modulated pressure component dependent on? To find the answer to this question consider Figure 6. The rate equation for the population density N_1 of the relevant excited level is given by (12):

$$dN_1/dt = I\,S\alpha N_0/(\pi\Delta\nu) - IS\gamma N_1/(\pi\Delta\nu) - N_1/\tau_r - N_1/\tau_c \qquad (1)$$

The terms on the righthand side represent the rate of excitation, stimulated emission, spontaneous decay and collisional, non-thermal de-excitation, respectively. The total number of molecules per unit volume in higher

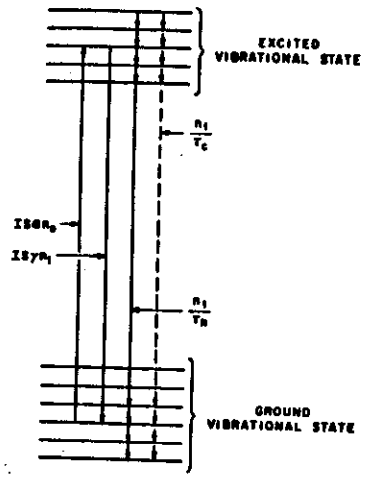

Figure 6. Schematic representation of the principle transition rates between the lower and upper vibrational states (12).

vibrational state is N_0, and $\Delta\nu$, S and I denote the linewidth of the absorption line, the line strength and the number of impinging photons per unit time and unit area. Finally symbols α, γ, τ_r and σ_c refer to the probabilities (that the molecule in the lower (higher) vibrational state is also in a rotational state which is a lower (higher) state of the transition respectively (12).

The above equation can be rewritten (using $\tau_I = \frac{IS}{\pi\Delta\nu}$) in a more simple form, after some modification:

$$dN_1/dt = N\alpha/\tau_I - N_1/\tau \qquad (2)$$

where N ($N = N_0 + N\Delta$) is the number of molecules per unit volume in both higher and lower vibrational states with the absorption frequency that

coincides to the frequency of incident ratiation and τ is given as:

$$\tau = IS(\alpha + \gamma)/(\pi\Delta\nu) - 1/\tau_C - 1/\tau_r \qquad (3)$$

The solution of the differential equation (2) has to be found for two distinct time intervals, as the gas is modulated with the angular frequency $\omega = 2\pi f_m$ and period $T = 1/f_m$. For the time interval $t\epsilon[0,T/2]$ the population density is given as a function of time through the relationship:

$$N_1(t) = \frac{N\alpha\tau}{\tau} + C_1 e^{-t/\tau} \qquad t\epsilon[0,T/2] \qquad (4)$$

with C_1 being the integration constant.
In the second half period $t\epsilon[T/2,T]$ the incident radiation beam is prevented ($I = 0$) from reaching the gas in the cell and equation (2) yields:

$$N_1(t) = C_2 e^{-(t - T/2)\tau'} \qquad t\epsilon[T/2,T] \qquad (5)$$

The time τ' is defined through: $\left(\frac{1}{\tau'} = \frac{1}{\tau_r} + \frac{1}{\tau_C}\right)$ (6)

The integration constants C_1 and C_2 are obtained from the boundary conditions $N_1(t=0) = N_1(T)$ and $N_1(T/2)^- = N_1(T/2)^+$.
The constant C_2 is only important during the second period when ($I = 0$). In order to calculate the fluctuating pressure amplitude p(t) superimposed above the equilibrium static pressure p_o it is necessary to solve the differential equation (12, 13):

$$dp/dt = \frac{2\,h\nu\,N_1}{3\,\tau_C} - \frac{(p - p_o)}{\tau_T} \qquad (7)$$

with τ_T being thermal relaxation time of the gas volume. The solution is given by:

$$p(t) = p_o + \frac{2\,h\nu\,e^{-t/\tau_T}}{\tau_C} \int_o^t N_1(t)\, e^{t/\tau_T}\, dt \qquad (8)$$

with $N_1(t)$ being given by eqn. (4). Substituting eqn. (4) for $N_1(t)$ into eqn. (8) for p(t) and evaluating the integrals one obtains: for $0 < t < T/2$:

$$p(t) = p_o + \frac{2\,h\nu\,N\alpha\,\tau\,\tau_T}{\tau_I}(1 - e^{-t/\tau_T}) + \frac{2\,h\nu\,\tau\,\tau_T}{3\,\tau_c\,(\tau_T - \tau)}\,C_1\,(e^{-t/\tau} - e^{-t/\tau_T}) \qquad (9)$$

As τ_I is much larger than τ' it follows from eqn. (6) that $\tau \approx \tau'$. Since $1/\tau' = 1/\tau_c + 1/\tau_r$ and τ_c is a few orders of magnitude shorter than τ_r, it follows that within a good approximation (12):

$$\tau \approx \tau' \approx \tau_c \qquad (10)$$

In addition τ' is much shorter than thermal diffusion time τ_T, i.e. $\tau' \ll \tau_T$.

The integration constant C_1 is obtained by substituting boundary condition $N_1)(T/2)^- = N_1(T/2)^+$ into $N_1(0) = N_1(T)$, i.e.:

$$C_1 = \frac{N\,\alpha\,\tau}{\tau_I}\left[\frac{e^{-T/2\tau'} - 1}{1 - e^{-T/2(1/\tau + 1/\tau')}}\right] \qquad (11)$$

which reduces to $C_1 = -\frac{N\,\alpha\,\tau}{\tau_T}$ upon substituting $\tau \approx \tau'$.

Correspondingly, in the relationship for p(t) from eqn. (9) some terms simplify since:

$\frac{2}{3}\frac{h\nu\,N\alpha\,\tau\,\tau_T}{\tau_c\,\tau_I}$ reduces to $\frac{2\,h\nu\,N\alpha\,\tau_T}{3\,\tau_I}$ and

$\frac{2}{3}\frac{h\nu}{\tau_c}\frac{\tau\,\tau_T}{\tau_T - \tau}\left[-\frac{N\alpha\,\tau_T}{\tau_I}\right]$ becomes $\frac{2\,h\nu\,\tau}{3\,\tau_I}$ (12)

This second term is much smaller than the first term in (12) since

$$\tau \approx \tau_c\ (1\mu\text{sec}) \ll \tau_T$$

The second term in eqn. (9) can therefore be neglected, and hence in $0 \leq t \leq T/2$:

$$p(t) = p_o + \frac{2\,h\nu\,N\alpha\,\tau_T}{\tau_I}(1 - e^{-t/\tau_T}) \qquad (13)$$

The term outside the bracket of eqn. (13) can be considered as the amplitude of the a.c. component. Realizing that $1/\tau_I = \frac{IS}{\pi\,\Delta\nu}$ one can rewrite it as

$$\frac{2\,h\nu\,N\alpha\,\tau_T}{3\,\tau_I} = \frac{2\,h\nu}{3} \cdot I \cdot N \cdot \tau_T \cdot \frac{\alpha\,S}{\pi\Delta\nu} \qquad (14)$$

This is the basic photoacoustic equation in gases, indicating that the magnitude of the modulated pressure signal is proportional to intensity of the power source I reaching the gas molecules, and the number of absorbing molecules N, thermal relaxation τ_T and the effective absorption cross section σ for the transition involved ($\sigma = \alpha S/\pi\Delta\nu$). The last term in eqn. (13) exponential term with ratio of τ/τ_T becomes $(1 - e^{-T/2\tau_T})$ at the end of the first chopping period $t = T/2$. As long as T is longer than τ_T the value of this term approaches unity. For reasons of completeness, the expression for pressure p(t) in $0 \leq t \leq t/2$ is given again:

$$p(t) = p_o + \frac{2\,h\nu}{3}\,I\,N\,\tau_T \cdot \sigma\,(1 - e^{-t/\tau_T}) \qquad Nm^{-2} \qquad (15)$$

since dimensionally:

$$\left[\frac{N}{m^2}\right] = \left[\frac{N}{m^2}\right] + [-]\,[m^{-2}\,sec^{-1}] \cdot [m^{-3}]\,[sec] \cdot [m^2]\,[-]. \qquad (15a)$$

The above statement could also be described by the requirement needed to maximize the P_{abs} power absorbed by the gas for efficient pressure generation.

The product $h\nu$ I σ N in eqn. (15) represents, in fact, the power absorbed in the sample per unit volume.

We can come to the same expression by considering the beam of radiation with power P incident on the gaseous column (assume cylindrical). Lambert Beer's law states that the power emerging out of the column of length L will be given by:

$$P_{trans} = P e^{-\beta L} \tag{16}$$

with β being the absorbance of the sample per unit length.

The power absorbed by the sample is then

$$P_{abs} = P - P_{trans} = P - P\, e^{-\beta L} \tag{16a}$$

When one deals with weak absorptions β is small and hence the eqn. (16a) becomes, after expanding into the series and neglecting higher terms (14):

$$P_{abs} = P\, \beta\, L \tag{16b}$$

The material coefficient β can also be expressed via absorption coefficient κ (atm^{1} m^{-1}) or absorption cross section σ (m^2/molecule), so that eqn. (16b) can also be written as:

$$P_{abs} = P\, \sigma\, N_a L = P\, \kappa\, p\, L \tag{16c}$$

where N_a is the number of absorbing molecules. If C is the fractional concentration (dimensionless number) of the absorbing species then $N_a = C\, N^o$ where N^o is the total gas density, the following relationship is obtained:

$$P_{abs} = P\, \sigma\, N^o\, C\, L \tag{16dc}$$

and the fractional absorption per unit length is:

$$A_{abs} = P_{abs} / L\, P = \sigma\, N^o (m^{-1}) \tag{16e}$$

Summarizing, the pressure fluctuation will produce an electrical signal S in the transducer, the magnitude of which will be dependent on the microphone sensitivity, degree of coupling and geometry of the vessel containing the gas, gas parameters and the amount of power absorbed by the gas i.e.:

$$S\ (V) = P_{abs}\ (W)\ R\ (V/W) \tag{17}$$

Where R is the term called responsivity of the detection system. Strictly speaking, the power emitted by the source and the absorption cross section are wavelength λ dependent and hence

$$S_\lambda\ (V) = P_\lambda \cdot \sigma_\lambda \cdot C\, N^o\, R \tag{17a}$$

Inspection of eqn. (17a) reveals that one can either vary wavelength λ while maintaining the constant concentration C throughout the experiment or alternatively, tune the source on transition specified by σ while maintaining varying concentration C. In the former case the obtained photoacoustic spectrum resembles the true absorption spectrum, while in the latter a gas concentration monitor is being produced. The high power available with the laser source provides large signals and therefore an increase in the sensitivity. Another important laser property, the degree of collimation, allows the deposition of excitation energy within a small volume which accomodates the gaseous sample which also facilitates the detection. In an ideal case of a strong, continuously tunable laser, it would also be possible to perfectly match the emission frequency of the monochromatic radiation source to the absorption frequency of the species, thereby ensuring very high specificity (14). Unfortunately, there is no such powerful source as yet, and in practice one relies on the near coincidences, although the conventional blackbody sources are also being used occasionally.

Experiments have shown that the linear relationships between S and C in eqn. (17a) in absence of saturation, holds true over a broad concentration range. Such a large dynamic range makes the laser a photoacoustic instrument, very usable in monitoring the changes in concentration.

The typical set for gas phase photoacoustic studies is shown in Figure 7 below and exhibits close resemblance with that of Bell. Since many molec-

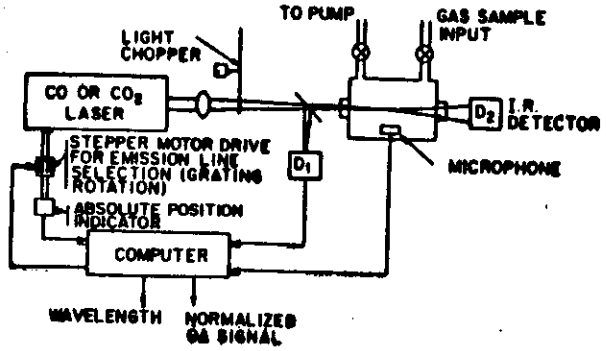

Figure 7. Schematic diagram of steps tunable CO/CO_2 laser photoacoustic spectrometer for studies on gases (15).

ules (also the pollutants) strongly absorb into the 1-20 microns anfra-red portion of the electromagnetic spectrum (Figure 8), quantitative analysis and the high resolution spectroscopy is possible. Numerous experiments have been carried out with a large variety of molecules in order to determine the absorption cross sections at infra-red laser wavelengths. The majority of work naturally concerned the powerful, but only step tunable, CO_2 laser and the CO laser to a lesser extent. Minor amounts of research have been done with moderate power colorcenter and diode leadsalt lasers, although the development of this latter category of lasers progresses at a very high rate at the moment.

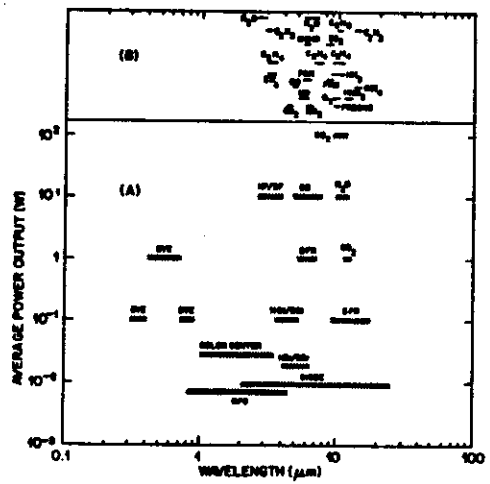

Figure 8. Typical levels of output power (W) for laser emitting in 0.1 μ to 100 μ spectral range. Some of the gases that absorb in the 1μ-10μ region is also given (16).

With laser output power levels in the order of 1 Watt it is possible to achieve the detection limit in concentration measurement of 1 ppbv and even under this value corresponding to minimum detectable density of approximately 10^{14} per m^3. In Table 1 the strongest absorption coefficient (atm^{-1} cm^{-1}) is quoted for some molecules which absorb in the CO_2 laser range (17). There were and still are, several attempts to produce a photoacoustically based monitor. Hubert claims that more than 250 gases of environmental interest, including the explosive vapours and industrial toxic substances could, in principle, be investigated with a CO_2 laser (18). The research group of Gelbawchs and Loper at the Aerospace Corporation in Los Angeles, that of Sigrist and colleagues at the Swiss Federal Institute in Zurich. Hess at Heidelberg, Patel's at the Bell Telephone Laboratory at Murray Hill (USA) and Lethokov and Zharov's at Moscow University, have been active for quite some time and have contributed to a bulk knowledge of (environmental) laser photoacoustic measurements on gases. The onset of activities in the Netherlands, were originally concentrated at the Catholic

University Nijmegen and the Agricultural University Wageningen in the summer of 1983. Since then other universities and industrial laboratories in the country have become involved and are now satisfactorily operating the photoacoustics in a number of practical applications.

Gas	Absorption cross section ($atm^{-1}cm^{-1}$)	Transition	Reference
Acrolein	2.74	10P (6)	(17a)
Trichlorethylene	14.55	10P (20)	(17b)
Vinylbromide	4.02	10P (22)	(17b)
Styrene	2.75	10P (44)	(17b)
Toluene	0.67	9P (28)	(17b)
Chlorine dioxide	1.50	10P (30)	(17c)
Ethylene	32.14	10P (14)	(17d)
Ammonia	25.80	9R (8)	(17d)
Vinyl chloride	8.80	10P (22)	(17d)
Ozone	12.00	9P (14)	(17d)
Water vapour	$2x10^{-9}$	10R (20)	(17d)
Methanol	10.61	9P (36)	(17e)
Acetonitrile	0.157	9P (16)	(17e)
Sulphur dioxyde	0.093	9R (26)	(17e)
Ethyl acetate	12.16	9P (8)	(17e)

Table 1. Absorption cross sections for some gases absorbing at CO_2 wavelengths.

I.2 Instrumentation

Once you have a strong radiation source at your disposal, it is a very important matter to properly design the photoacoustic cell, i.e. volume space that contains the gas sample and transducer. This optimization is particularly important when low level concentration measurements are concerned. The optimization refers to the geometrical design of the photoacoustic detector that would possess superior optical and acoustical characteristics (Figure 9).

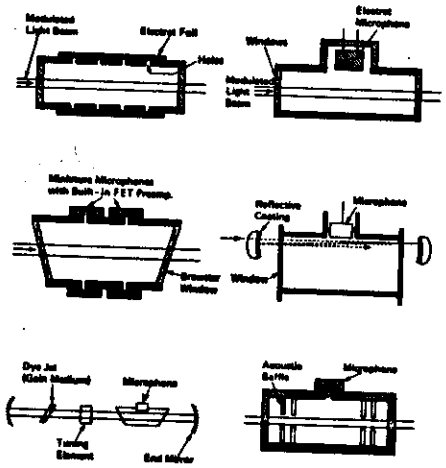

Figure 9. Several types of gas photoacoustic cells. This figure is reproduced form Tam's review in Kliger's book (2).

In general there are two types of cells distinguished with respect to their acoustical performance. The non-resonant cell is the sample space designed in such a fashion that no acoustical resonances can affect the cell response. This is contrary to the resonant cell, where the choice of proper

dimensions of the sample space just creates the resonator which amplifies the pressure fluctuations. In the non-resonant model however, the pressure builds up until an equilibrium situation is reached. This condition is characterized by equal amounts of heat deposited in the gas and the heat conducted away from the gas towards the cell wall. The non-resonant cells normally have small dimensions - in such a small volume more pronounced pressure signals will be produced much easier. However, it is not allowed to reduce the diameter at will, because the exciting radiation laser beam, having a Gaussian beam profile, has to be coupled into the sample space without hitting the cell walls. Likewise diffusion to the wall may not be a dominant process as the signal will inevitably be lost for the photo-acoustic detection.

The resonant cell system is normally a cylindrically shaped chamber. In order to excite the resonances, both the length and diameter of the cylinder are much larger than the cross section of the excitation beam. Three main spatially different types of natural resonancies f_{mnp} for cylinder length L_o and radius R, can be excited: longitudinal (index p), radial (index m) and the azimuthal mode (index n), as well as the combination of these.

The lowest radial mode (100) resonant mode causes the distribution of gas density that is largest along the geometrical axis of the cell. Efficient coupling with the beam of the incoming radiation can therefore be expected (Figure 10).

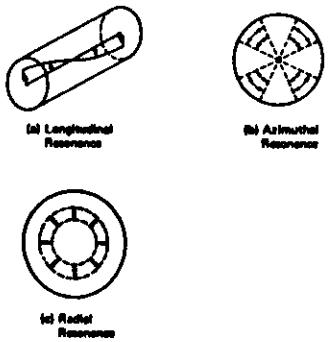

Figure 10. Three types of acoustical resonances inside a cylindrical cell (2).

The radial standing pressure wave at distance r from the axis of a cylinder with radius R (normalized to unity on the axis), that is in the phase with the amplitude of excitating beam is described by (14):

$$p(r,t) = J_o\,(3.833\ r/R)\ e^{-\omega t} \qquad (18)$$

with J_o being a Bessel function of zeroth order.

First radial resonance occurs at much higher frequency (few kHz) than longitudinal resonances (Figure 11). It is customary to associate the

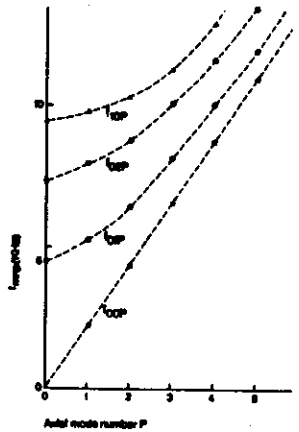

Figure 11. Resonant frequencies for a cell with diameter of 20 mm and length of 240 mm.

quality factor Q with the acoustical resonator defined as the ratio of resonant frequency f_o and the bandwidth Δf corresponding to the points at $(\sqrt{2}/2)$ of the signal amplitude at resonance on both sides of the resonant frequency f_o (Figure 12).

$$Q = (f_o/\Delta f) \qquad (19)$$

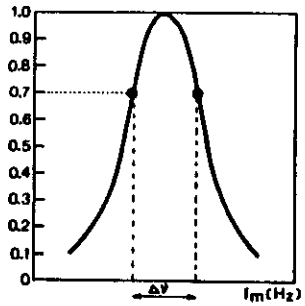

Figure 12. Quality factor oaf a resonator. Vertical axis represents relative amplitude of the photoacoustic signal. Frequency at peak response is f_0.

Resonant cells with Q factors as high as 2500 have been reported (19, 20) values of 400-500 are normally encountered. A cell with a very high Q is very sensitive to small changes in temperature which can impede its performance.

Major losss in the resonant radial cell occur on account of heat conduction from the pressure wave towards the walls and the viscous dissipation (from the radial motion of gas) at the end of the cell.

A majority of photoacoustic studies on environmental samples are done at the atmospheric pressure in the cell. If high resolution gas phase investigated is an impetus, low pressure (50 Torr or less) is suggested. Kraft and Bevan performed an evaluation to ascertain that high Q values (and response) normally attainable with resonant cells are sufficient to overcome the advantages of the small volume, but optimized non-resonant cells (21). Their experiment shows that within 760 - 5 Torr, both the signal, as well as the signal to noise ratio of small volume non-resonant cells are considerably larger than the corresponding values obtained with resonant cells. Small sample space might be an important advantage when toxic or expensive samples are to be studied.

A convenient way to increase the amplitude of the pressure wave in the photoacoustic cell is to allow the incident radiation to make several passes through the medium across the cell length instead of only once (Figure 13). This is a multipass cell geometry design contrary to the single pass type described above. Another possibility to increase the amount of absorbed power by the gas is to place the photoacoustic cell inside the cavity of the laser itself thereby making use of much higher intracavity beam power that, in such a manner, becomes available for absorption (Figure 14).

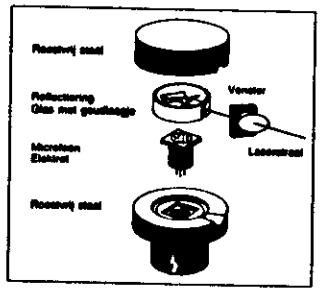

Figure 13. This photoacoustic cell, developed by K. Veeken (Catholic University Nijmegen) allows the excitation beam to make a large number of passes without ever emerging out of the sample volume (22).

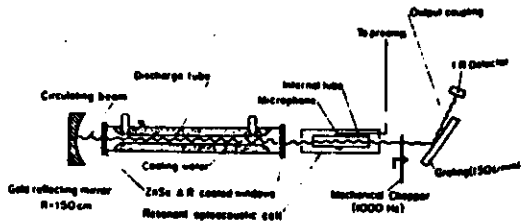

Figure 14. The principle of CO_2 laser intracavity photoacoustic detection (23).

A microphone is used as a transducer to detect the amplitude of pressure waves. Capacitor microphones used in the first experiments were gradually replaced by small size and low noise electret microphones with built-in amplifiers. Nowadays, the miniature ear-aid microphones have become popular due to their nominal high sensitivity, broad frequency response, reliability, cost aspect and broad dynamic range.

The microphone is operated in a phase sensitive detection scheme using lock in amplifiers to reduce the effective noise bandwidth, since the noise of a microphone is proportional to the square power of the bandwidth.

In any photoacoustic cell, windows and walls also contribute to the production of pressure in the sample (Bell effect) and are therefore also an adequate electric signal. The origin of this background signal is due to the absorption of radiation (and hence of heating) of the solid windows that cause (by diffusion) the transfer of heat into the adjacent layer of gas in the sample volume. Additional contribution to the background signal comes via the scattering (or reflection) loss and subsequently heating of the wall. This backround noise is sometimes called coherent photoacoustic background, since it is not caused by the bulk of the gas in the cell. However, the coherent background signal is narrowbanded, as it is modulated at the same frequency as the true signal (and is also a locked-in phase). Its magnitude which is proportional to the input laser power, cannot be reduced electronically and therefore the cell has to be designed in such a way that it would minimize the effect of a photoacoustic background. The mean value of the voltage signal (i.e. sound) caused by the modulation process in the absence of the exciting radiation is called the coherent acoustical background. Like the photoacoustic background, the coherent acoustic background is narrowbanded as it has the same frequency as the modulating source (chopper) and moreover has a fixed phase relation with the modulation. Photoacoustic background can be minimized by using windows of good optical quality and low refractive indices with the absorption coefficient as small as possible at the wavelength of interest. Mounting the windows at Brewster angle allows the use of materials with a larger refractive index. A convenient way to reduce the parasitic signal from the windows in a resonant cell is to use the baffle structure (circular plates with a hole in the

middle). In this manner the excitation beam is allowed to pass through the hole, while the background noise will be reduced due to the shielding. However, the quality factor of the resonator is affected by this obstacle resulting in lower Q values. Finally there is a random broadband noise, electronical (pick-up) or acoustical in nature, which does not have any fixed phase relationship in respect to the modulation source. The ultimate noise limit from a pressure naturally transduces stems from the Brownian motion of the molecules of the gaseous sample. In any case, since the amplitude of the background signal is independent of the sample, gas absorbance must be substracted from the measured signal in order to get a true absorption signal generated by the sample. Insulating the photoacoustic chamber acoustically from vibrations caused by a modulator, (cell separated from the modulator using a double walled structure with evacuated space in between) or selecting the optimum position of the cell in respect to the sound sources associated with the modulation source, may help in lowering the coherent acoustical background. We conclude this section by emphasizing that the cell walls should be smooth and that proper care has to be exercised in respect to the cell construction material in view of absorption and memory effects.

The remaining equipment needed for the performance of photoacoustic experiments includes the modulator source, power detector and some optical components such as a beam splitter. Lasers operating in continuous mode can be suitably modulated (in power) with a mechanical chopper. The frequency stability of the chopper must be as high as possible, since any jitter eventually results in an increased noise level. Some authors (24) shield the chopper acoustically from the cell by operating the chopper in a vacuum, or using the vibration dampers under the mount that carries it. Other schemes such as the electronic current modulation or frequency modulation (may prove more applicable to some specific problems) might turn out to be much quieter than in the case of mechanical modulation by the chopper. Experiments were also reported in which non-linear crystals were used as a low-noise electro-optical modulator. Although expensive, such modulators are nowadays available throughout the entire infra-red region.

Since the photoacoustic signal is proportional to the power absorbed by the sample (and hence also to the input power) and the concentration of the gas species it is necessary to normalize the lock-in signal when the photoacoustic absorption spectrum is recorded (Figures 15 and 16). This is easily achieved by sampling a small portion of the laser output power before it enters the photoacoustic cell. This fraction is measured by the power and is easily achieved by inserting a flat plate (beam splitter) of transparent

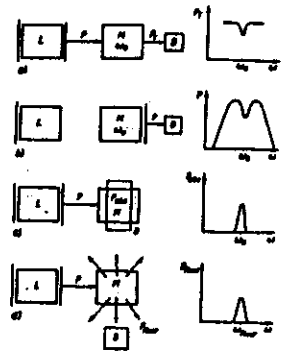

Figure 15. Various methods to measure absorption at frequency ω_0:
a. transmission; b. intracavity spectroscopy; c. photoacoustics;
d. fluorescence. (M is medium, L is laser, D is detector) (25).

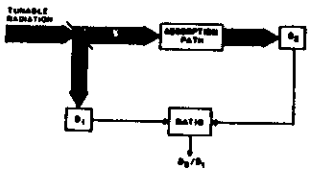

Figure 16. Principle of absorption measurement by normalization of the transmitted signal (16).

material at relevant wavelengths between the laser and the chopper at a certain angle with respect to the emerging laser beam (optical axis). The small fraction of laser output power at each emission wavelength will then be deflected by the beam splitter and its amount measured by the power detector (for example a thermopile detector). Normalization of the spectrum is achieved by dividing a d.c. signal for the lock-in detector with the d.c. signal from a thermopile using the ratio meter (voltage divider). The plot of the normalized signal versus the wavelength is the true absorption photoacoustic spectrum (including the noise) of the sample.

Pulsed mode laser operation in conjunction with the photoacoustic detector is used more frequently in studies of the relaxation processes in gases. The time duration of the pulse and its period are both much shorter than the molecular and thermal relaxation times.

The majority of the experiments on gaseous samples which have been performed so far at the universities of Wageningen and Nijmegen, are carried out in the infra-red with the CO_2 laser wavelengths.

The experimental set up (Figure 17) is built on a low cost granite plate resting on a heavy table (metal frame filled with sand). The table is supported by four shock absorbers to reduce the building vibrations.
The waveguide laser used here (50 cm discharge length) is a modified version of the model developed at the University of Pisa (..). The plasma bore (diameter 3 mm) is made out of quartz and has a cooling jacket across its entire length. The laser operates with a flowing mixture of He, Ne and CO_2 a in 6:1:1 ratio and the working pressure in the laser is about 70 Torr. Output power of the laser is about 5 W at its strongest transition. Selection of the desired wavelength is achieved by the reflection grating with 150 lines/mm and a resolution of approximately 70 GHz. The separation between two successive CO_2 laser transitions is about 60 GHz. The linewidth of the laser is about 300 MHz at working pressure of 760-Torr that is equal to the free spectral range (c/2L) of the laser resonator, which, in prin-

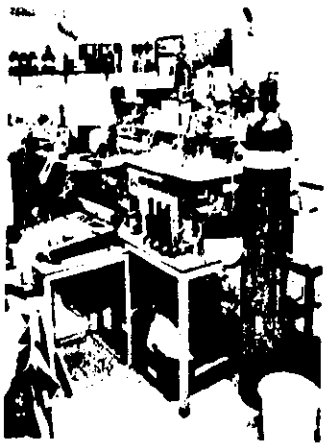

Figure 17. Photo of the set up.

ciple, enables a single mode operation. The pressure broadening (~ 5MHz/ Torr) for most of the molecules studied is about 5 GHz.

Currently the laser is stabilized actively, (using a fast response pyroelectric detector) providing $1:10^4$ long term power stability. Special attention has been paid to manufacturing a chopper blade. Significant reduction of the noise present in the photoacoustic signal has been achieved by phase stabilization of the chopper. Harren reports (26) factor 9.5 improvement in the signal to noise ratio observed in our experimental system, when using the laser and chopper stabilization (as compared to the free running operation).

The output coupling semi concave mirror is made of ZnSe and has a radius of curvature 1 m and reflection coefficient of 70%. As the emerging laser radiation has to be transported over a long distance before completing the passage through the cell, it is necessary to ensure the collimation degree of the beam reasonably well. This problem is particularly important when waveguide laser producing intrinsically divergent beams is being considered. Harren (26) uses spherical mirrors with a radius of curvature

equal to 750 mm positioned at focal distance (750 mm/2) from the output coupling hole of the laser (this mirror laser acts as a collimator). For lasers with moderate power levels (say 5 W) good operating infra-red mirrors can be made by depositing reflective coating on cheap glass lenses. Radiation spots not larger than 6 mm in diameter at a distance of 1.5 m from the laser have been achieved in such a fashion (26) allowing proper matching of the beam into the cell and its unimpeded passage.

Several types of photoacoustic cells have been tested. At present one uses the resonant single pass cell (Figure 18) which operates in the lowest

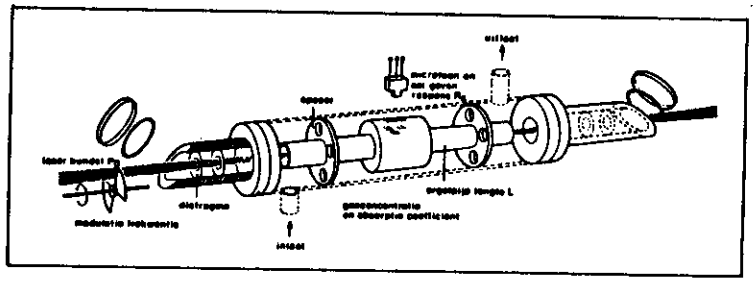

Figure 18. 'Organ pipe' model of photoacoustic cell described in the text. Symbols: EB, excitation beam; Ch, chopper; W, window; Se, seal; Dia, baffle; Sp, spacer; Mi, miniature microphone; Gi, gas input; Go, gas outlet; IT, inner tube; OT, outer tube.

longitudinal mode at about 560 Hz. The cell is an improved version of an earlier design (Figure 19) proposed by (27). It consists of an outer stainless steel cylinder 470 mm long and 60 mm in diameter, which accomodates another, shorter, coaxial cylinder 300 mm long and 9 mm in diameter also made of stainless steel. The inner tube, an actual resonator, is held in the outer tube by means of 3 equidistant teflon centering rings with a number of holes (6 mm diameter) to allow for uniform distribution of the

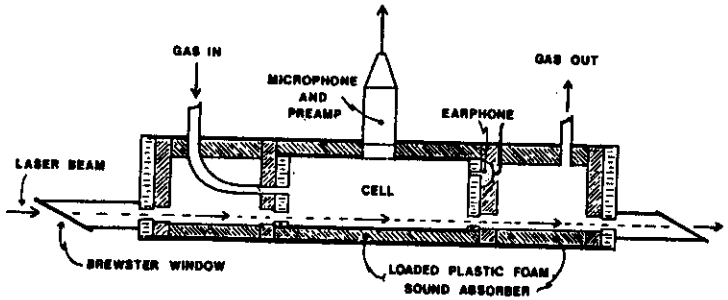

Figure 19. This photoacoustic cell was used by and for sensitive concentration measurement of atmospheric pollutants in flowing regime (27).

gas within the cell. The inner surfaces of the resonator are smooth and polished. A total of four miniature electret microphones for hearing aids provided with a hybrid integrated amplifier for low output impedance, are mounted (at 90° with respect to each other) in the teflon ring (Figure 18) with a centre hole in the diameter which is equal to the outer diameter of the resonator. This ring is pulled over the resonator. Microphones used are manufactured by Knowless (type 1760 II), and their dimension is 7.5 x 3 x 2 mm. The diamter of the membrane is 1 mm. The characteristics of this type of microphone corresponds very well with the electret microphone 32 produced by Microtel (Figure 20). The sensitivity at 550 Hz is about 60 dB relative to 1 V per 0.1 Pa. (1 Pascal = 94 dB = 1 N/m² and 1μbar = 74 dB = 0.1 N/m²).

The size of each of the four coupling holes drilled in the resonator wall is 2 mm which is 1 mm larger than the diameter of the microphone membrane (Figure 21). The microphones were mounted flush with the outer resonator wall in order to avoid the deterioration of the Q factor. We have also done some experiments using larger microphones (Philips hypercardioid electret 3922 with ½ inch diameter and a sensitivity of 10 mV/Pa) but no significant

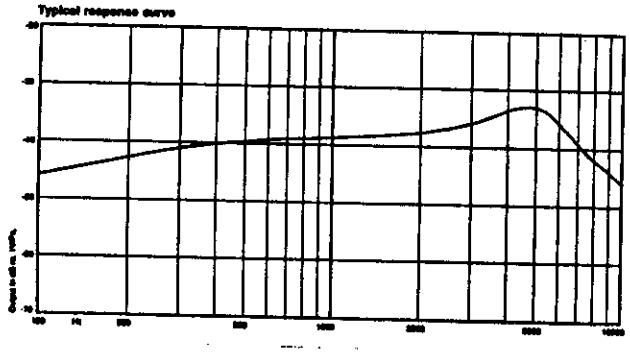

Figure 20. Frequency characteristics of miniature Microtel M32 electret microphone. Sensitivity at 550 Ht is 59 dB re. 1V/Pa; 59dB re. 1V per 0.1 N/m².

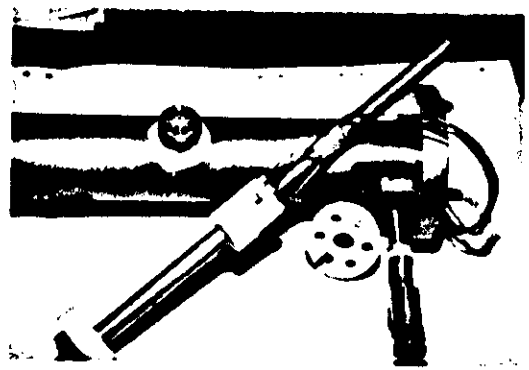

Figure 21. Photograph of the 'organ pipe' gas photoacoustic cell showing the inner tube resonator with ring (front), spacer and outer tube (background).

difference has been obtained when comparing the results collected with the miniature microphones. No definite answer can as yet be given as to what it pertains as the optimal choice of the coupling hole diameter as well as of the inner tube dimensions, and more experimental work is needed. The ring with the four microphones is placed halfway the total length of the resonator in the plane perpendicular to the longitudal axis of the resonator.
The outer cylinder can be vacuum sealed from the environmental air by two easily exchangeable end caps that carry the ZnSe windows mounted at the Brewster angle. As seen in Figure 17 the centre point of each window sis al a larger distance from the microphone unit than the end section of the inner resonator.
The theoretically obtained Q value of 28 agrees fairly well with experimentally measured Q factor of 34.

Bernegger from the Swiss Federal Institute wrote the computer program that represents three dimensional plot of the pressure amplitude per unit absorption coefficient per unit power (Figure 22) versus position coordinate and the modulation frequency for our cell (28).
The photoacoustic cell from Figure 21 is also suitable for flow measurements. The inlet and outlet gas ports (6 mm diameter) are made from stainless steel tubing. The ports protrude the outer wall and are soldered to it. The position of each port coincide with the plane accomodating the end section of the inner resonator. Resonating standing wave in the open end resonator has nodes at both ends of the tube, and hence weak coupling of the flow induced fluctuations to the main signal is expected. The outlet port (like the inlet port) is equipped with the needle valve inserted in the vacuum line to smooth the flow of the streaming gas sample. Sirgle stage rotary pump provide the vacuum needed to suck the mixture through the cell. Traps could be placed along the pumping line to eliminate, for example, water vapour or carbon dioxide from the environmental or laboratory air. Noise originating due to the gas stream was found negligible for flow rates up to 15 liters per hour (26).
The choice of cell material is of great importance in particular when low concentration is concerned. Residual traces of strange gas(es) that absorb

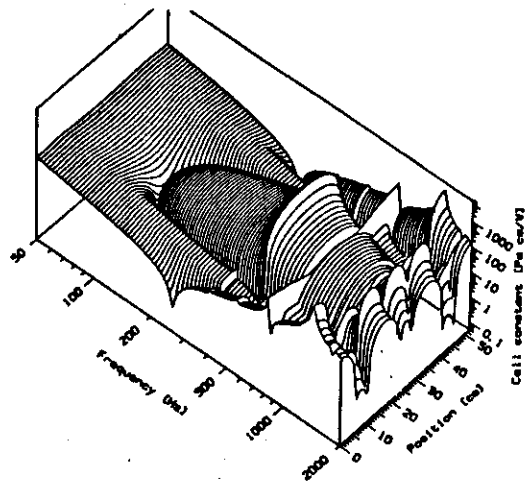

Figure 22. Three dimensional plot of signal amplitude $[\frac{Pa}{W\ cm^{-1}}]$ versus modulation frequency [Hz] and coordinate [cm] for organ pipe resonation (L = 300 mm, diameter D = 9 mm) described above (28).

at the same wavelength will contribute to the resultant signal by interference. Some gases show specific affinity for a specific surface; therefore the adsorption effect must be minimized. Loper et al. have studied the influence of cell coating on the rise time needed for the photoacoustic signal to reach the input level for several gaseous mixtures flowing through the cell (19). As seen in Figure 23 in the case of ammonia, 90% of the input level is reached in 2.8 minutes (teflon), 34 minutes (gold), 2.5 minutes (parafine) and 100 minutes for ammonia (stainless steel). Hydrazine N_2H_4 a carcinogenic substance from rocket fuel, shows the same behaviour. In the case of ethylene C_2H_4, input level is reached within about four minutes. In general, teflon material causes the least amount of adsorption; from teflon materials the blue Teflon or Kaynar seems to be the best choice.

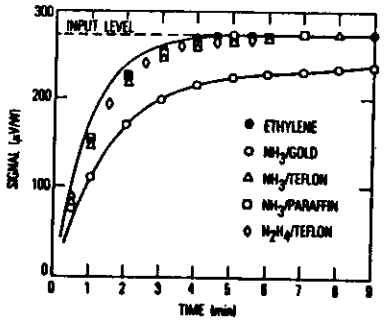

Figure 23. Photoacoustic signal is affected by adsorption effect of ethylene, ammonia and hydrazine gases on different surfaces (19).

Calibration is needed before the spectrophone can be used for practical measurements. This is done in the laboratory using the set of premade concentrations containing gas to be measured in dilluted different proportions with dry nitrogen. Normalized lock in signals at selected laser wavelengths are then plotted against the concentration - in general linear dependence is observed. The experiment is repeated, but now with the sample volume being filled with nitrogen in order to establish the background signal level. This should be subtracted from the previously obtained signal obtained with the gas species. If the noise on the top of the lock in signal is measured, it is possible to deduce the ultimate sensitivity i.e. the concentration detection for which the signal to noise ratio is unity.

In the realistic atmosphere the situation is more complicated. Since the compositon of the environmental sample is not known a priori, it is necessary to know the photoacoustic spectra of each possible constituent possibly present in the mixture. Sigrist has shown that the absorption of urban polluted air in the 10.4 microns band of the CO_2 laser is dominated by practically three components: water vapour, carbon dioxide and the hydrocarbon ethylene (29). The absorption cross sections of these constituents have also been determined by other authors. Based on these data one can select these transitions of the CO_2 laser that guarantee minimum interference. For CO_2, C_2H_4 and H_2O these are 10P (20), 10P (14) and 10R(20)

respectively. The absorption of CO_2 results in a photoacoustic signal with inverse phase with respect to the incident radiation (so called 'cooling effect'). To account for both the amplitude and the phase one can write (29):

$$S_i \cos \phi_i = \sum_{j=1}^{3} c_j S^o_{ij} \cos \phi^o_{ij} \qquad (20)$$

where the summation index runs over three constituents. The unknown concentrations c_j for three gases are obtained by solving the above equations. The term on the left hand side of the eqn. (..) represents the total additive signal (normalized) S_i and the corresponding phase ϕ_i at particular laser transition i. Symbols S_{ij} and ϕ_{ij} refer to normalized calibrated amplitude and phase produced by the C_j concentration due to the j^{th} component. In the above equation spectral interferences between the individual constituents are characterized by the non-diagonal elements of the matrix $S_{ij}\,\phi_{ij}$ $(i \neq j)$. The above linear relationship is justified if the concentration levels are low. The effect of cross sensitivity on the species to be measured can be estimated by assuming two of the three concentrations being constant at first and then calculate how the concentration of the third component will be affected if one of the two concentrations (first assumed constant) changes slightly (29). (This approach has been tested in practice by Sigrist and his colleagues (29); and excellent agreement with data collected by other control measurements has been obtained.

I.3 Applications

I.3.1 Ethylene

Netherlands is one of the well developed European countries and agriculture in general forms one of the country's most important economic post (yearly some 15 billion dollars of export). Industrial development led to increased levels of pollution with its unavoidable impact on agriculture as well. There is continuous governmental funding to stimulate the optimization of crop yield of various cultivars.

Ethylene is the major urban phytotoxicant (concentrations of 20 to 130 ppbv) with potentially hazardous effects to the vegetation. Other hydrocarbons (sulphur dioxide, nitrogen oxides, ozone) cause adverse effects at higher concentration levels.

One peculiar thing about ethylene is that the gas is also known as an endogenous plant hormone which regulates growth and ripening (all the higher plants produce ethylene). When certain harvested agricultural products sensitive for ethylene are placed within a space where ethylene is being produced, the role of ethylene will prevail above all other hormones causing an unbalanced situation and consequently damage to the products (30). Not all agricultural species produce an equal amount of ethylene (Table 2) though apple and tomato are characterized by a high production. The sensitivity to ethylene varies from sort to sort (flowers like carnations and orchidae and cereals are very sensitive, as well as tulips, potplants, cucumbers etc.) (31). The effect of ethylene on the plant is manifested on subcellular scale, but sometimes the complete ecological systems may also be affected. Briefly, the main concern of Dutch growers is to prevent quality loss resulting from exposure of some plants to ethylene and extend the tenability. This quality loss of the product is comparable to a sort of ageing syndrome - the leaves turn yellow, flowers drop off or get misformed, leaves dry up etc. (Figure 24). Discoloration is due to the formation of red pigment stimulated internally by ethylene (32). For example, carnations, one of the main export articles, reacts strongly when exposed to 100 ppb of ethylene at room temperature. In big import and export halls

Product	Ethylene production rate (kg^{-1} $hour^{-1}$)
potato, carrot, strawberry pineapple, kiwi, okra	0.01 - 0.1
cucumber	0.1 - 1
banana, mango, melon, figs, tomato	1 - 10
apple, apricot, avocado, papaya, pear, peach, plum	10 - 100

Table 2. Ethylene production per unit mass and time (hour) for several products of agricultural interest (30, 31).

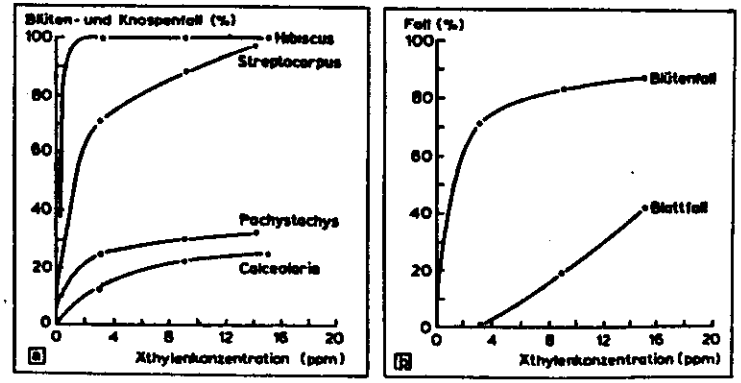

(a) (b)

Figure 24. Percentage of blossom and bud for potplants (Fig. a) and clerodendrum (Fig. b) after 1 day exposure to ethylene gas (31).

where auctions are held, ethylene sensitive and ethylene making products are often put close to each other; the same is true when they are being transported (aeroplane, trucks). The forced ventilation should then take care that the concentration remains below 100 ppbv. However, in the climatological conditions typical for Holland, large temperature differences between the outer air and the internal air from storage compartments require additional investment (heating). Moreover, the composition of air (already polluted) used for ventilation, causes additional problems.
Ethylene enters the plant through the leaves during the normal gas exchange process required for growth. Plant physiologists make distinction between three main types of injuries of vegetation. In the acute form, the net result is necrosis followed by leaf discoloration. In chronic form the injury is evidenced by long term effects without a necrosis. Then, there is also a third type of injury manifested by growth inhibition disturbances such as radial swelling and inclination towards the horizontal level. This last type of injury is thought to be caused by ethylene gas binding to some receptor cells in the plant tissue.

The natural abundance of the ethylene in the unpolluted atmosphere is constant (3 to 5 ppbv). Due to the intensive traffic combustion the ethylene concentration tends to exceed the background value by order of magnitude. Direct hormonal damage described above will then be followed by the onset of the autocatalyses leading to the accelerated production of ethylene itself (ethylene biosynthese) by the plant. This, not completely understood effect, will persist for longer intervals, even after the ethylene source causing the autocatalysis, has been removed (32). The autocatalysis eventually leads to premature riping phenomena and hence economic loss for the grower.

In some situations governed by the market situation, it may just be convenient to make use of the ripening effect of ethylene. In the Netherlands tomatoes and apples, still on the tree, are sometimes sprayed with Ethrel, an ethylene containing constituent, especially at the end of summer when light conditions are unfavorable (32). Products can be collected earlier

and get a nicer colour. Since quite recently this procedure is also applied to iris flowers.

Conclusion

From the above, it is clear that ethylene issue deserves great attention. Therefore the ethylene dose-injury relationship is needed for the specific vegetation, (Table 3). The effect of ethylene in the presence of pollut-

Response	Dosage		
	Concentration		Time
	µg/m³	ppm	
Abscission			
Cotton leaves, square	46-3,435	0.04-3.0	Not stated
Cotton leaves	685	0.6	1 month
Pepper and tomato flower buds	115	0.1	Less than 8 hr
Rose leaves	345	0.3	120 hr
	11,450	10.0	24 hr
Snapdragon petals	575	0.5	1 hr
Chlorosis on leaves			
Cotton (slight)	685	0.6	1 month
Cowpea	2,290	2.0	1 day
Rose	1,145	1.0	5 days
Death of plant			
Cowpea	2,290	2.0	10 days
Dry sepal injury			
Orchids (severe)	115	0.1	6 hr
Orchids (typical)	46	0.04	8 hr
	23	0.02	24 hr
Orchids (slight)	5.75	0.005	24 hr
	345	0.3	1 hr
	57.5	0.05	6 hr
	11.5	0.01	24 hr
Epinasty			
African marigold	1.15	0.001	20 hr
Various plants	345	0.3	24 hr
	3,435	3.0	3 hr
	2,290	2.0	10 days
Flowers do not open			
Carnation	115	0.1	3 days
Orchid	575-1,145	0.5-1.0	20 hr
Flowers close			
Carnation	115	0.1	6 hr
	575	0.5	12 hr
Growth inhibition			
Cotton	685	0.6	1 mo
	46-3,435	0.4-3.0	Not stated
Lily family	860	0.75	7 days
Various plants	2,290	2.0	10 days
Loss of apical dominance			
Cotton	46-3,435	0.04-3.0	Not stated

Table 3. Dosage-injury response of the various plants when exposed to ethylene (33).

ants has to be studied as well. This is a complicated problem since the net effect (synergisme or antagonism) is seldom a simple sum of individual effects. Some experiments indicate that combined effects are also concentration dependent. The metabolic production of ethylene by plants presents an attractive field of fundamental studies too; as shown in Figure 25.

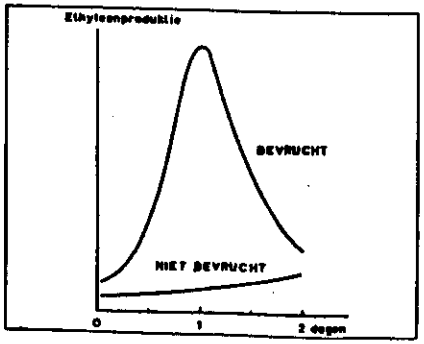

Figure 25. Difference in ethylene rate production for fertilized and unfertilized flower versus time (32).

To attack the ethylene problem one can either concentrate on performance of measurements in the laboratory (and/or in the field) under a variety of (climatological) conditions and collect as much relevant data as possible, or alternatively try to virtually eliminate ethylene. Many activities take place along the first route. For both indoor and outdoor measurements a selective, sensitive and fast detector is needed. The gaseous second route involves the use of scrubbers capable of 'killing' the ethylene in storage compartments. A few years ago catalytic oxydation, solid scrubbing materials such as active carbon and aqueous solution of potassium permangate have been tested with limited success. Recently, a biotechnological project based on scrubbing by means of bacteria was initiated in Wageningen, The

Netherlands. The idea is to use the alkene consuming Mycobacteria 2W in the bioreactor in order to eliminate ethylene in the gas phase by oxydation to water and carbondioxyde.

A need for a practical ethylene detector triggered several research projects in the Netherlands. Several months ago a prototype of a low maintenance automatic monitor was developed which meant an inexpensive apparatus for growers to be used on ships, in greenhouses, trucks etc. The operational principle is based on the interaction of ethylene with ozone (from an induction coil) producing formaldehyde. Upon excitation the formaldehyde returns to its ground state thereby emitting the amount which is proportional to ozone and indirectly to ethylene.

Simultaneously the development of the photoacoustic based sensor using the CO_2 laser as excitation source is underway. Ethylene strongly absorbs the laser emission range with the best coincidence and the largest absorption coefficient (~ 30 $atm^{-1}cm^{-1}$) at 10P(14) transition. The ratio of line strengths on the left and right of the 10P(14) line is 1:4 and 1:6 making 10P(14) suitable for monitoring purposes. The photoacoustic spectrum of ethylene dilluted in pure nitrogen is shown in Figure 25 (26). In the pres-

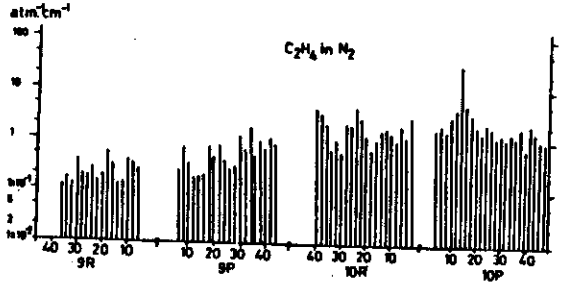

Figure 26. The CO_2 laser photoacoustic spectrum of ethylene in nitrogen (26).

	Laser transitions			
Gas	$R(20)$	$P(14)$	$P(16)$	$P(26)$
C_2H_4	1.27	29.1	4.55	2.4
CO_2	0.0022	0.0021	0.0022	0.0019
H_2O	8.36×10^{-6}	9.04×10^{-6}	8.97×10^{-6}	6.76×10^{-6}
Background	1	1	1	1

Table 4. Absorptions coefficient ($atm^{-1}cm^{-1}$) for monitoring ethylene in the realistic atmosphere using four CO_2 laser transitions.

sence of interfering components (Table 4) such as water vapour and the carbon dioxyde, the sensitivity decreases but this problem can be solved by scrubbing the flowing air sample. The extracavity sensitivity limit is presently about 0.1 ppbv for lock-in integration time of 1 sec and laser power in the order of 1 Watt. Further improvements are possible by working intracavity, and allowing longer sampling intervals. Quite recently the real-time ethylene production from several emasculated orchidae flowers has been measured (34) for the first time ever (Figure 27). Shortly after emascula-

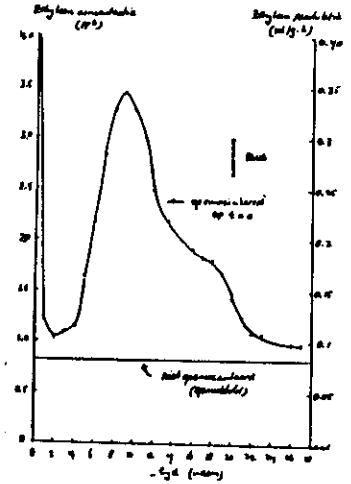

Figure 27. Ethylene production of Cymbidium flowers (nL/gh) and ethylene concentration (ppbv) in flowing air (34).

tion, ethylene production begins to rise reaching a peak of 0.35 nl/g hour, 12 hours after the starting and drops back to the original level again 12 hours later. The experiment in which production of single flower is being measured is underway.

A series of experiments in which the effect of varying concentration and dosis-effect relationship was studied on various agricultural products was performed (35, 36, 36a). Such studies are carried out using the fumigation chambers in the lab, outside air (the so-called open top chambers) and in open field. This construction (shown in Figure 28), offers the possibility

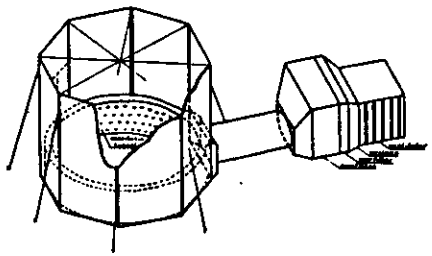

Figure 28. The open-top fumigation chambers for studies of air pollutant effects on plants. Closed chamber and field fumigation experiments are also performed (36, 37, 38).

to achieve a climatological situation normally encountered in practice while simultaneously having the possibility to filter out or add any desired proportion of the pollutant. A mobile, truck station (vane vehicle) is now under construction. Field photoacoustic measurements are already being done (Figure 29) by the Sigrist group at the Swiss Federal Institute in Zurich to determine the ethylene emission along the highways and in the cities (29). In several other places in the world (Aerospace Corp. Los Angeles, Copenhagen) attempts are now being made to fabricate a multicomponent detector capable of real-time monitoring in the ppbv (or even under) measurements in the realistic atmosphere (20). Quite recently initial steps were set to study the feasibility of photoacoustic technices (for atmospheric measurments) when installed on board of an aeroplane.

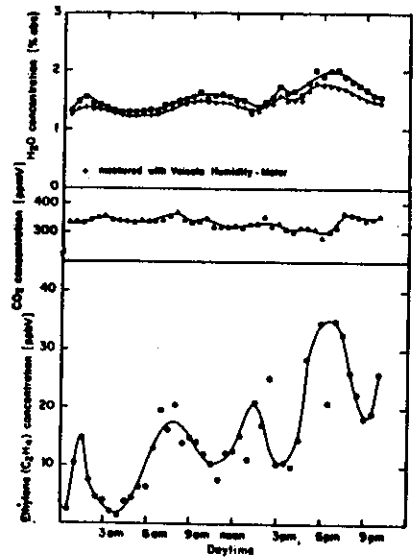

Figure 29. Variation of air component concentrations measured with the mobile CO_2 laser photoacoustic system on July 2, 1986 (location: Biel, Switzerland (29).

I.3.2 Ammonia

Ammonia is a toxic pollutant with less activity than that of ethylene In Dutch agriculture the greatest injury to plants is normally found in the vicinity of units involved with intensive livestock (these sites are rich on other phytotoxic components such as amines, organic acids, sulphides etc.). The gas penetrates the leaf stomata and the intake is a function of atmospheric concentration, stomata opening and the diffusion resistance of the leaf boundary layer. In the fumigation experiments it is observed that ammonia gas has a pronounced inhibiting role on the photosynthesis, causing decrease of carbohydrate content and growth. It is also noticed that exposure to ammonia leads to increased sensitivity of cold temperatures. The dosis-effect relationship varies from product to product: conifers are sensitive to long-time and low concentration while cauliflower and tomato

exhibit the opposite effect (high concentration during short intervals). Field experiments were carried out in Wageningen by the Research Institute for Plant Protection using the poultry and piggery farm as the measuring sites.

No difference concerning injury was observed when field measurements are compared to fumigation experiments at NH_3 concentration of 0.6 to 1 mg/m³ in the air. This confirms that ammonia is a major livestock pollutant. Furthermore, there is evidence that ammonia together with sulphur dioxide is very efficient in dissolving the waxy layer on pine trees affecting the evaporation and mould (38). With the steadily increasing degree of pollution more restrictions are being imposed by the Dutch government on farmers with respect to the amount and time interval during which manure can be deposited. With air norms in sight, there is a need for a real time ammonia concentration meter (most of the available instruments measure indirectly) as well as for an organised network of country wide stations.

Ammonia exhibits one particularly strong absorption line in the 9R of the CO_2 laser (Figure 30). It is a line that coincides with 9R(28) laser tran-

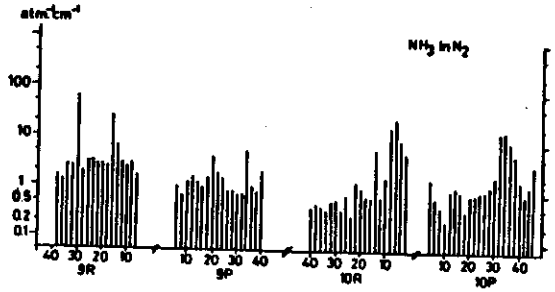

Figure 30. The CO_2 laser photoacoustic spectrum of ammonia NH_3 in nitrogen (26).

sition. The strength of the absorption line is about 80 $atm^{-1}cm^{-1}$, almost 2.5 times stronger than that of ethylene. The ratio of the neighbouring lines is favourable (20:1 and 30:1) so that this line can truly be taken as

very characteristic, easy to recognize, fingerprint of the molecule. In our initial experiments, ammonia in pure nitrogen has been used and the sensitivity limit of about 1 ppbv has been reached (26). Real atmosphere measurements of ammonia require additional precautions (water vapour and carbon dioxyde in particular) and scrubbing will then be a necessity. In particular, the CO_2 gas interference presents a problem due to the true frequency coincidences between the absorbing CO_2 molecules (hot band) and the CO_2 laser emission spectrum. Another possible manner of by-passing these sort of difficulties is to use nitric oxyde N_2O gas in the active laser gas mixture.

I.3.3 Ozone

Ozone is the most important constituent of the photochemical pollution occurring due to a complexity of reactions in the atmosphere under the influence of the sunlight. The reactions involve the oxydes of nitrogen (traffic, combustion in general), hydrocarbons (traffic and rafineries) and the oxygen. The natural concentration of ozone on earth level due to the reactions between the penetrated short wave solar flux and the nitrogen oxydes and hydrocarbons emitted by the vegetation amounts to 40 to 80 $\mu g/m^3$. The role of ozone in West Europe was underestimated until the 1970's because the solar irradiance was considered as quite low. With increasing traffic and industrialization the levels of nitrogen oxyde have changed and the damage to plants caused by ozone became evident in the Dutch climate (38, 39). The effects of ozone vary from visible damage to very fine alterations on the biochemical level. Tobacco plants in particular, but also beans and spinach are susceptible to ozone damage leading to growth deformations and yield reduction. Quantitative relationship between the dosis and the effect of ozone have been studied in Wageningen with tobacco as species (39) and is shown in Table 5. The concentration of, for example, 27 $\mu g/m^3$ causes one percent of leaf damage after 7 days. When concentration is increased to 73 $\mu g/m^3$ the above percentage rises from 1 to 10! Recent experiments have established that other agricultural products such as potatoes, onions as well as horticultural products are quite sensitive to

ozone. The CO_2 laser provides several frequencies at which ozone monitoring can be done photoacoustically.

Exposure (days)	Percentage of leaf damage (%) 1	5	10	50
1	108	212	288	708
2	66	130	177	434
3	50	98	133	327
4	41	80	109	267
5	35	68	93	228
6	31	60	82	201
7	27	54	73	178

Table 5. Relationship between ozone concentration in $\mu g/m^3$ exposure duration and the injury for tobacco plant (39).

As seen in Figure 38 the strongest absorption (approximately 10 $cm^{-1}atm^{-1}$) takes place at 9P(6) transition although the weaker 9P(26) may appear more suitable due to more pronounced finger prints there. The sensitivity of the present experimental system allows the sub ppbv detection (in dry N_2) as shown in Table 6, and further improvements are possible.

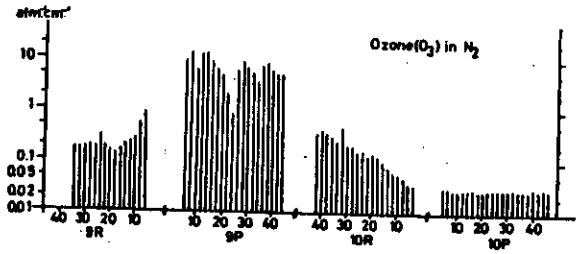

Figure 31. CO_2 laser photoacoustic spectrum of ozone in nitrogen (26).

Gas.	Abs.coef. atm^{-1}cm^{-1}	CO_2 laserline	detection limit
C_2H_4 ethylene	30.4	10P14	0.3 ppb
NH_3 ammonia	56.2	9R30	0.2 ppb
O_3 ozone	12.7	9P14	0.8 ppb
H_2S hydrogensulphide	4×10^{-3}	9R24	2.3 ppm
C_2H_3Cl vinylchloride	8.8	10P22	1 ppb
$C_4H_8O_2$ ethylacetate	12.	9P6	0.8 ppb
C_2H_4Br 1.2 dibromoethane	0.2	9R26	46 ppb

Table 6. Detection sensitivities for some pollutants achieved with the CO_2 laser photoacoustic spectrometer by Harren et al., (26). The results are valid for 1 W laser power.

I.3.4 Some other gases of relevance

Large number of pollutants have been studied with respect to the injury threshold of the plants. In Table 7 the symptoms of the concentrations and the exposure times are quoted for some cultivars (40). From those, detection of toxic hydrogen sulphide and growth inhibitor can be attempted with an CO_2 laser but the absorption coefficients at these wavelengths are in order of magnitude weaker (Figure 32) than in the case of ethylene (also

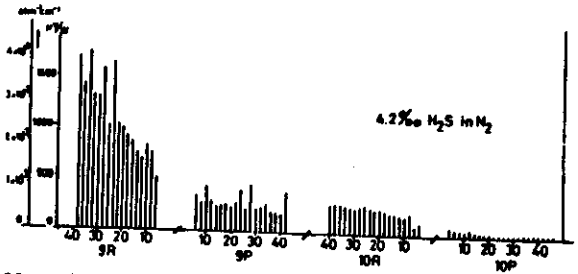

Figure 32. The CO_2 laser spectrum of hydrogen sulphide in nitrogen (26).

see Table 1). The sulphur dioxyde has no strong absorptions in the CO_2 laser region. However, the sub ppbv detection limit has been achieved (41, 42) in the near infra-red even with moderate input power levels of the diode lasers. The SO_2 penetrates the plant through the stomata openings and penetrates the intracellular space where it dissolves in water thereby producing the bisulphite HSO_3 and sulphite SO_3 ions which, in turn, affect the protein and lipid of the cell membrane causing changes in its permeability (38).

Harren investigated photacoustically the 1,2 dibromoethane $C_2H_4Br_2$ in its relationship to agriculture. This carcinogenic gas, has high vapour pressure at room temperature. There are places in the world where growers intentionally induce the chemical reaction between $C_2H_4Br_2$ on solid zinc to produce ethylene and use it thereafter for fumigation of (for commercial reasons) of citrus fruits in order to change the colour from green to orangelike. This is dangerous for humans, (through respiration) animals and plants. The CO_2 laser photoacoustic spectrum shows no specific finger print (Figure 33). Another component of interest to humans is the carcinogenic

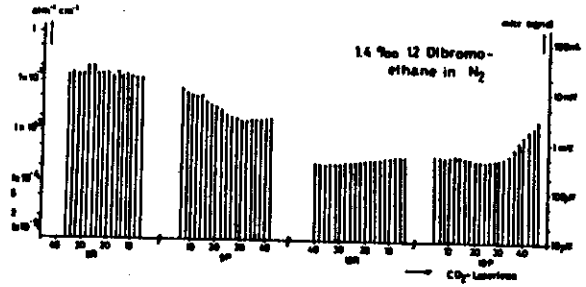

Figure 33. CO_2 laser photoacoustic spectrum of dibromoethane $C_2H_4Br_2$ (26).

monovynilchloride C_2H_3Cl: the maximum allowed concentration has recently been lowered to 50 ppbv. So far no observable effects have been found on some agricultural products in the fumigation experiments (concentrations

Pollutant	Symptoms	Maturity of leaf affected	Part of leaf affected	Injury threshold		
				ppm (vol)	µg/m³	Sustained exposure
Sulfur dioxide	Bleached spots, bleached areas between veins, chlorosis; insect injury, winter and drought conditions may show similar markings	Middle-aged most sensitive; oldest least sensitive	Mesophyll cells	0.3	785	8 hours
Ozone	Fleck, stipple, bleached spotting, pigmentation; conifer needle tips become brown and necrotic	Oldest most sensitive; youngest least sensitive	Palisade or spongy parenchyma in leaves with no palisade	0.03	59	4 hours
Peroxyacetyl-nitrate (PAN)	Glazing, silvering, or bronzing on lower surface of leaves	Youngest most sensitive	Spongy cells	0.01	50	6 hours
Nitrogen dioxide	Irregular, white or brown collapsed lesions on intercostal tissue and near leaf margin	Middle-aged leaves most sensitive	Mesophyll cells	2.5	4700	4 hours
Hydrogen fluoride	Tip and margin burn, dwarfing, leaf abscission; narrow brown-red band separates necrotic from green tissue; fungal disease, cold and high temperatures, drought, and wind may show similar markings; suture red spot on peach fruit	Youngest leaves most sensitive	Epidermis and mesophyll cells	0.1 (ppb)	0.08	5 weeks
Ethylene	Sepal withering, leaf abnormalities; flower dropping, and failure of leaf to open properly; abscission; water stress may produce similar markings	Young leaves recover; older leaves do not recover fully	All	0.05	58	6 hours
Chlorine	Bleaching between veins, tip and margin burn, leaf abscission; marking often similar to that of ozone	Mature leaves most sensitive	Epidermis and mesophyll cells	0.10	290	2 hours
Ammonia	"Cooked" green appearance becoming brown or green on drying; over-all blackening on some species	Mature leaves most sensitive	Complete tissue	~ 20	~ 14,000	4 hours
[illegible] chloride	Acid-type necrotic lesion; tipburn on fir needles; leaf margin necrosis on broad leaves	Oldest leaves most sensitive	Epidermis and mesophyll cells	~ 5-10	~ 11,200	2 hours
Mercury	Chlorosis and abscission; brown spotting; yellowing of veins	Oldest leaves most sensitive	Epidermis and mesophyll cells	< 1	< 8,200	1-2 days
Hydrogen sulfide	Basal and marginal scorching	Youngest leaves most affected		20	28,000	5 hours
2,4-Dichloro-phenoxyacetic acid (2-4D)	Scalloped margins, swollen stems, yellow-green mottling or stippling, suture red spot (2,4,5-T); epinasty	Youngest leaves most affected	Epidermis	< 1	< 9,050	2 hours
Sulfuric acid	Necrotic spots on upper surface similar to caustic or acidic compounds; high humidity needed	All	All	—	—	—

Table 7.1 The effects of some pollutants on vegetation (40).

lower than 2 ppmv were not used) performed in Wageningen. The CO_2 laser based photoacoustic monitor appears promising for the field applications with 10P(22) transition being the best choice (Figure 34).

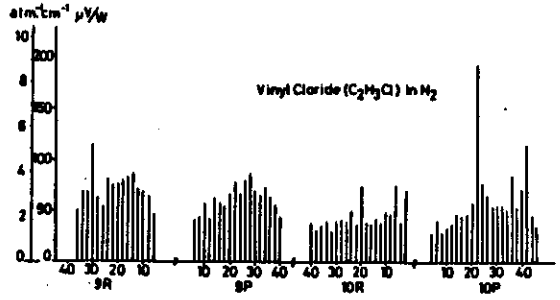

Figure 34. CO_2 laser photoacoustic spectrum of monovynilchloride C_2H_3Cl (26).

I.3.5 Sprout growth supressors

The harvested potato is a living organism implying that certain chemical processes dependent on the condition of the plant itself as well as on the environmental condition, will take place. One of such processes is sprouting. Following the harvest and prior to storage, both seed and ware potatoes exhibit a period of 'germination rest' - a dormancy phase which is species dependent.

The degree of potato sprouting potential varies spontaneously in the period following the harvest. Dormancy is interrupted at a certain moment and soon after that the phase of maximum sprouting and growth power is reached. The vitality of the tuber deteriorates in the period to follow; this is accompanied by the physiological ageing process causing quality loss of the procuct (Figure 35).

To supress the sprouting of ware and seed potatoes in the course of their storage period, various techniques are used. In recent years reasonably

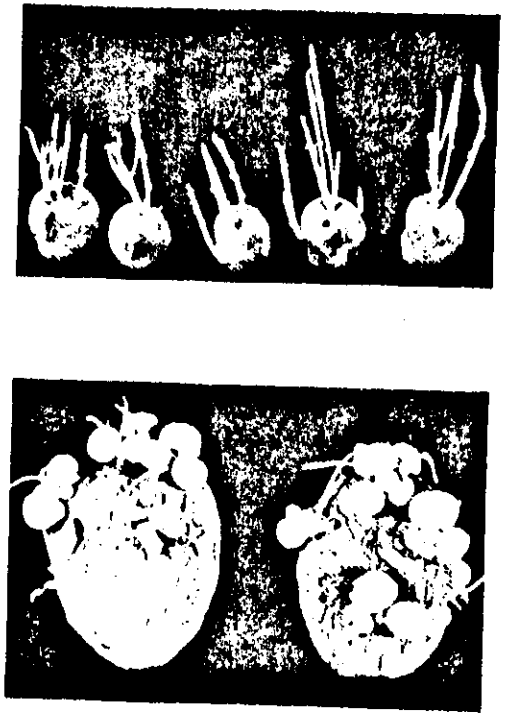

Figure 35. The effect of sprout inhibiting treatment in potatoes. The tubers in both photographs are of the same age - the tubers in a) are vital, while those in b) are physiologically 'aged' (43).

good control has been achieved with seed potatoes using the reduced storage temperatures providing seedlings that develop well after planting.

The potatoes meant for consumption undergo additonal treatment with solid or liquid sprout inhibiting chemicals. The research on volatile sprout supressants, preferred above solid and liquid ones, has been initiated several years ago in order to find their effect on the prolongation of storage life in potato tubers. This enables the grower to plant the potato

with optimal potentiality at any desireable time, instantly ready to be used in any climate.

Following the originally used chloropropham, propham and tenzacene, other, new inhibitors such as α-pinene benzothiazole, 1,4 dimethylnaphtalene, α-terpineol limonene, camphor, carvone, pulegone, borneol, emerged. The object of choosing these volatile chemicals is to ensure the minimal effect on yield performance, also for the consumer. Interestingly enough, the potato and some other products themselves, contain their own supressant substances (i.e. 1,4 dimethylnaphtalene). In practice the experimental studies are carried out in batches with potatoes stored under well defined conditions using the inhibitor at certain low concentration levels and comparing the results gathered over longer time intervals with those observed with the untreated control potatoes. The emergence scores are being recorded in order to find the average. Simultaneously the sprout length data are collected. Finally a field experiment must be carried out to establish the true usability of the inhibitor.

Carvone, pulegone, dimethylnaphtalene and benzothiazole have proven effective to some extent although much more research is needed. Possibly, the CO_2 laser in the photoacoustic detection scheme as a very sensitive on-line concentration meter, could provide more interesting information on that matter. Initial experiments performed with pulegone $C_{10}H_{16}O$ and carvone $C_{10}H_{14}O$ (vapour pressures of 18 Pa and 16.6 Pa at 25°C respectively) show sufficient number of coincidences, although no significant finger print of the molecule is seen in this spectral region. The research on this topic is in progress (43a).

I.3.6 Aerobic meat spoilage

The consumption of meat per capita in the Netherlands has increased from 38 kg in 1960 to 73 kg in 1982. In meat, like in almost all foods, the appearance, odour and tastiness deteriorates when the product is stored in air. The aerobic spoilage is a rather complicated process which involves the action of mixed bacteria flora. There is a generally recognized need for a measuring technique which would enable one to establish the criteria

for meat quality acceptance. In practice, this means identifying the spoilage compounds chemically (44) in course of time.

Currently the used spoilage analysis method involves the determination of a microbiological number count (the logarithm of bacteria count per cm^2) by means of inoculating the sterile meat sort with a known single strain of bacterial microflora (for the aerobic spoilage at lower temperature these are Pseudomonas and Brochothrix thermospacta) and by monitoring the selective count number as a function of time. But in a normal situation the meat product is contaminated by a natural way and the obtained results are misleading when compared directly to those collected with inoculated samples. Besides, the microbiological methods are inherently very slow. Another possible way to approach this problem is to try to detect the concentration of volatile compounds which are being produced during the aerobic spoilage. If the appearance (visual), smell (reception) and the count are simultaneously being evaluated, it may be possible to find the quantitative relationship between chemical change (concentration change of one or more individual components) and count number. This would greatly facilitate assessment of quality factor and allow the prediction of the meat shelf-life.

In a few experimental attempts of this kind already performed, (for some meat sorts and temperature range) mass spectrometry and gas chromatography have been used (45, 46) to detect the volatiles. Pertaining to the odour, the alterations in the sensory reception from 'fresh met' to malodours described as fatty, dairy (count) and 'fruity' (count 9) have been reported (47). The microbiological count is a non-linear function of time (Figure 36) approaching a saturation value after long exposures of concentrations.

Volatiles such as acetoine, diacetyl and 3-methyl-1-butanol show their peaks about 3 days from onset of the above experiments. In the phase to follow, esthers are formed with ethyl acetate $C_4H_8O_2$ playing a dominant role. In the last phase characterized by high count (number 10), the proteolysis takes place resulting in the emission of sulphur compounds. Finally there were some hydrocarbons (1 undecence, toluene and methylbenzene) de-

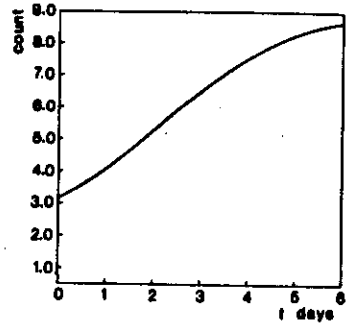

Figure 36. The microbiological count number versus the time for beef (at 5°-C) inoculated with Pseudomones fragi bacteria (44).

tected in the initial phase. The perceived odour sequence (fresh to sweet) showed a relationship in respect to the volatiles quoted above.

We have recently attempted to study the aerobic meat spoilage using the CO_2 laser photoacoustic spectroscopy, primarily because of its potentially great sensitivity and speed of response. An esther, ethyl acetate, has initially been chose as a chemical indicator (at room temperature) in beef samples inoculated with bacteria Pseudomonas fragi. The absorption cross sections of ethyl acetate have previously been determined at CO_2 laser wavelengths. Our own introductory measurements (Figure 37) on ethyl acetate

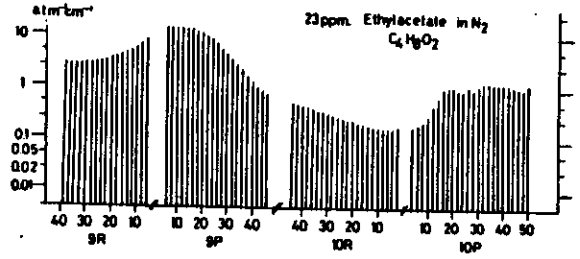

Figure 37. The CO_2 laser photoacoustic spectrum of ethylacetate in nitrogen (26).

diluted in nitrogen, reveals grasslike spectrum with the strongest photoacoustic signal at 9P(6) (absorption coefficient 12 $atm^{-1}cm^{-1}$) corresponding to detection sensitivity limit of 0.8 pbv (Table 6). Such a congested specrum is obviously not suitable for monitoring purposes and the interpretation of data is difficult. However, there is evidence for the presence of ammonia developed in the course of meat spoilage. More measurements on fish, poultry and other meat samples are also to be carried out with indicators in the near future.
In another independent experiment the possibility to analyse edible oil photoacoustically will be investigated (fatty acids). The method might also prove successful in determining the presence of polycyclic aromatics.

I.3.7 "Greenhouse" gases and carbonmonoxyde

There is a strong tendency towards optimization of crop yield through climate control by combining the knowledge on 'plant model' and that of a 'greenhouse model'. The total energy balance of the greenhouse depends on a variety of physical processes. In hermetically sealed greenhouses the temperature and humidity would increase. The concentration of CO_2 on the other hand, is known to influence the growth. Carbon dioxyde on the other hand is produced by plants and by soil fertilizers. Therefore some means of regulation is required to achieve the control of either one of the above mentioned parameters. An experiment is in progress at the moment (48) in which the ventilation rate fold (expressed in the volume of exchanged air divided by the volume of the greenhouse) is determined as a function of wind velocity, roof window opening apperture and wind direction. Nitrous oxyde is chosen as an injected trace gas because it is inert (natural abundance is very low, not toxic at low level) and heavier than air. Since N_2O does not take part in the metabolic mechanism, measurements of its concentration as a function of time, makes the determination of ventilation rates possible for a variety of experimental conditions and hence also the total amount of CO_2 exchanged. An independent, simultaneous measurement of carbon dioxyde concentration provides the information about photosynthetic activity. The commercial monitor for N_2O operates at the fundamental vibrational frequency ν_1 at 1285 cm^{-1} which is outside the CO_2 laser emission range. The 100 ppmv concentration is thought adequate for the above application. Our intention is to construct the practical CO_2 laser photoacoustic based sensor for N_2O detection. Two laser lines, namely the 10P(18) and 10P(32) produce a relatively strong signal in N_2O (49). At the time of writing this report, a concentration limit of 200 ppm has already been measured.

The photoacoustic principle was also employed to develop an automatic CO_2 gas concentration monitor for non-invasive use with humans, as well as for diagnostic of respiratory disorders, since the adequacy of ventilation is relatec to the alveolar CO_2 pressure. This apparatus operates at 4.26 microns absorption frequency using the thermal source.
Gurevich et al. (50) demonstrated the feasibility of photoacoustic techniques for accurate measurements of microconcentrations (typically 1 mg/m^3) of carbon monoxyde in a multicomponent sample from the closed ecological system (CES) atmosphere. This dangerous air pollutant is normally detected (in higher concentrations) with conventional infra-red absorption methods (suffers from N_2O interference) or (at low levels) by gas chromatography.
Amer and Gerlach (52) used continuous wave CO_2 laser operating on transitions in a 1-0 band radiation to achieve 0.15 ppm detection limit.
Sigrist et al. (29) performed diurnal variation measurement of carbon dioxyde and water vapour with a CO_2laser demonstrating the potential use of photoacoustics for reliable humidity measurements. The highly sensitive cell (Figure 38) developed by Amer and Gerlach (52) is used in their experiments. It operates with a high Q factor (2500) in the first radial mode. The absorption cross sections at CO_2 laser wavelengths have been determined for large number of industrial pollutants and some carcinogenic compounds (85).

I.3.8 More complex systems

Molecules with low molecular weight exhibit relatively simpler spectra at atmospheric pressure. The detuning shift between the laser emission and gas absorption line is sufficiently low (near coincidence) to allow for the use

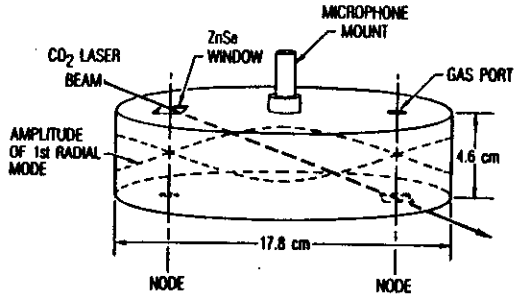

Figure 38. Resonant photoacoustic cell based on design of Gerlach and Amer (52) used by Sigrist (29) and Gelbawchs (19, 20).

of a discretely tunable source such as the CO_2 laser for excitation. However, for large molecules with many vibrational rotational transitions, selective identification of spectra in the complex mixture is very difficult as the broadening pressure will cause the overlap of adjacent individual lines (53). Such broadened spectral structures cannot, a priori, be resolved with the CO_2 laser. Lead salt (Pb Sn_xTe_{1-x}) diode lasers that operate in the 10 micron range have a typical emission linewidth of $10^{-4}cm^{-1}$ but suffer from low power drawback (about 1 mW). Kreuzer therefore suggested the use of a gas chromatograph in conjunction with the laser photoacoustic detector (Figure 39) in order to analyse complex mixtures. Upon the separation in the gas chromatograph (Figure 40) constituents are brought into a photoacoustic cell of small volume. This approach was shown to be very useful since the compounds with similar retention time can still be discriminated with respect to their absorption spectra (53). Therefore the comparison of the signals at several laser emission wavelengths facilitates the identification of the spectrum (Zharov et al.) were the first investigators to report on practical use of gas chromatograph and the set of three lasers to analyse the mixture of seventeen unsaturated and saturated hydrocarbons. Minimum detectable sensitivity of their set-up was $10^{-8}cm^{-1}$. Selective determination of various compounds is shown in the

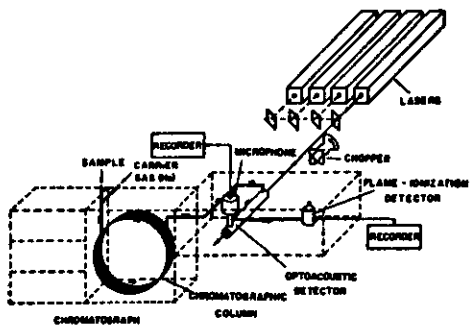

1. gas chromatograph
2. inlet gs to be studied
3. inlet carrier gas
4. chromatograph headspace
5. PA detector
6. He-Ne laser
7. modulation
8. microphone unit
9. registration unit PA signal
10. flame ionizaton detector
11. registration of chromatographic peaks

Figure 39. The combined use of gaschromatography and laser(s) photoacoustic spectroscopy (4).

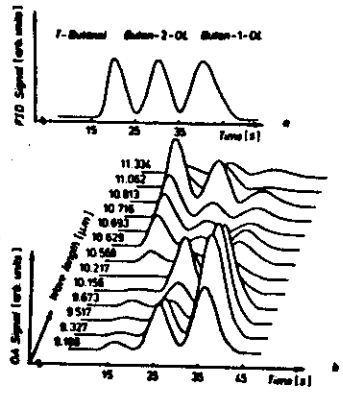

Figure 40. The spectrum of a mixture of hydrocarbons obtained by means of set shown in Figure 39.

spectrochromatogram (Figure 40) together with simultaneously measured signals by a flame ionization detector. Zharov et al. (54, 55) applied the same technique to identify the transisomers in the mixture of oleic and linoleic fatty acid esthers (food fats) and a mixture of methylcyclopentadiene positional isomers. The first process is important in the industrial food hydrogenation process of edible vegetable oil (margarine production).

Unsaturated fatty acids exhibit formation of stereoisomers (acids with cis double bonds become trans isomers) when hydrogenated.

Knowledge of time behaviour of this process and determining the content of isomeric forms is useful in controlling the hydrogenation. Experiments aimed to study the time dependent proces quantitatively in carboxyllic acids as well as to determine the concentration of fatty acids, esthers and triglycerides, are now being prepared in our laboratory. Colour center laser (2.2 to 4.4 microns) will be used for precise study of C_mH_n (laser frequency corresponds to C-H relevant vibration). The advantage of continuously tunable source and the high efficiency capillary column allows additional enhancement of the sensitivity. Use of the free jet to reduce the pressure broadening of the absorption lines will be attempted.

Recently Korobelnik et al. (56) constructed the CO_2 laser photoacoustic gas chromatographic system by connecting the photoacoustic cell at the end of the capillary column. The technique was used to analyse in real time, benzine fractions of petroleum oils originating from various depths (hence differences in composition and properties are expected). An optical parametric oscillation was achieved in $LINbO_3$ pumped by Q switched YAG: Nd^{3+} laser (57) and the spectra of some pollutants (ethane and propane) in the 2-4 microns region were recorded at atmospheric pressure and concentration level of 100 ppm. At the Technical University of Twente (Enschede, the Netherlands) efficient second generation of continious wave CO_2 laser radiation in proustite crystal has been obtained.

1.3.9 The oviposition deterring pheromone

In nature many insect species face the 'completely mixed' vegetation environment. Those insects which restrict their diet to one specific plant (or a few) must be capable of detecting their own habitat and host plant. The same is true for the egglaying female: if she fails to locate the proper site, the rate of larvae survival will be reduced. The recognition of host plants takes place along several distinct behavioural steps. Visual and olfactory stimulii are the means by which the female orientates before making contact with the plant to check whether the site is suitable for ovipositioning or not. Thus, if one is able to interfere externally in some way with the behaviour of the insect, it is possible to affect her ovipositioning behaviour (58). This in turn may result in the reduction of larval infestation level of pest insects in crop, and hence considerable economic savings.

One of the most common crop pests is the large white butterfly, Pieris brassicae, with domicle dominantly in Asian and European countries. The female butterlfy has the chemoreceptors on her legs and finds 'its sort' thanks to the presence chemical substances such as mustard oil glucosides in the plant. Also their larvae possess minute receptors on their mouthparts which are sensitive to the same substance. The caterpillars of this pest preferably feed on cultivated cabbage sorts and cause millions of dollars worth of damage throughout the world.

Towards the end of the past decade it was discovered that the ovipositioning female butterfly is able to make a clear distinction between its own egg and the eggs deposited on the cabbage by other females of the same sort (58). This is a kind of self protection to achieve the non-concurrent food position.

The experiments showed that the eggs produce a specific chemical substance called ovipositioning deterring pheromone (ODP). The ODP substance keeps other females away from the egg territory. If the ODP could be isolated and synthetically produced, one could interfere with insect behaviour. In agricultral practice this can be used to achieve a uniform egg distribution

over the available ovipositioning sites, thereby controlling the cabbage pest.

Much work aimed to study female respons to ODP, has to be carried out in the laboratory before large scale field application is anticipated. Both pre-ovipositioning and ovipositioning periods are studied under a variety of experimental conditions as well as the effect of the compound on other species.

I.3.10 Attractants as biological pest controllers

The leaf roller moth species represent a group of well known fruit orchard pests. Due to its very small size, it is very difficult to visually determine the precise moment of egg hatching. The emerging larvae search for fresh leaves and spun in leaves or fruits soon afterwards. As they are not easy to reach now, spraying is not very effective. Therefore, it seemed more appropriate to develop an alternative method to prevent excessive spraying. The summer fruit moth affecting the quality of apples and pears was the first insect subjected to a serie of experiments. In an attempt to reduce the economic damage caused in the crop by this pest, experiments were undertaken in order to find out whether interference with animal behaviour can be achieved. The tactic chosen was to interact with the male-female communication which is based on the sex pheromones released by the female (59). Two routes are possible: one can either prevent fertilization of females by male moths or alternatively, try to disrupt the mating through addition of some man-made substance which affect the mate finding ability. Both routes lead to the same end result - the reproduction will be strongly reduced and the pest can be controlled effectively. The mating takes place at night by means of very low concentration of sex pheromones released by the calling female. The chemical stimulii signals reach the male, sometimes at long distances (10-100m) from the female and guide them to their destination.

Efficient prevention of the fertilization (males are fertile a few hours per day during 14 days) can be obtained by registering (with light traps) the time interval which elapses between the onset of the male moth flight

and the moment of egg hatching. When the summer moth pheromone has been extracted and identified (positional isomers cis 9 and ciss 11 tetradecenyl acetate), light traps were replaced by sec pheromone traps.

The idea is to irreversibly catch as many males as possible into a sticky trap by manipulating with carefully selected one (or more) attractance pheromone. Minute deviations in the concentration result in a reduced catch.

Mating disruption, on the other hand, relies on a non-destructive approach, that disorients the male in the space, causing temporary adaptation of male receptors (hence the female calls will not be heard since the threshold sensitivity is lowered) or even leads to induction of permanent loss of behavioural reaction (alterations in the cerebral neural system).

In the first phase of the investigations, antipheromones were sprayed to disrupt the mating, later it turned out that the pheromone in a blend (closest to the natural pheromone) is more effective. It has now been established that effective population control can be achieved when 10% of all females mate (60).

In a recent field experiment, catch percentage as high as 96% has been obtained when pheromone, distributed in a matrix of 5 x 5 m over 400 ha (dosis 1 gram/ha) evaporated from dispensers. Higher values of catch are possible at larger concentration levels. At 10 gram/ha complete control can be established. Currently, experiments are done to study the mating and possible long-term developmental effects of the leaf roller moth. Possible application to other horticultural pests is now being studied (concentration, side effects on the environment etc.). The final goal is clear, the pheromones should act as biological control agent in the growth of fruit and other species, and should, as such, replace the chemical insecticides. Since the insect behaviour is concentration dependent, a need for low (ppbv) monitor is obvious.

I.3.11 E-β farnasene alarm pheromone

Small aphid insects spend a large part of their life on a very small area of a few mm^2. When facing a stress situation (for example visual or mechanic stimulii, or specific gas smell), the aphid produces (in syphons) a liquid, indentified as E-β farnasene. Evaporation is sensed by antennae (rhinaria) of conspecific aphids causing panic reactions.
In laboratories simulation experiments of electro-antennograms are recorded when aphids antennae are subjected to a flow of gaseous mixtures (at low concentration, ppbv level) evaporating from a pretreated strip [61]. The electroantennogram signal has an additive character, i.e. the signal is a sum of receptor potentials of individual olphactory receptors. By blocking some rhinaria, it is possible to find out which rhinaria participate in perception of the alarm pheromone. The panic reaction is accompanied by significant mobility increase of the aphids. Spraying under such conditions becomes favourable. Commercially available mixtures of pyretrum and E-β farnasene requires an approximately 10 times lower pesticide concentration than normally needed for comparable end results (61).

II PHOTOTHERMAL STUDIES ON CONDENSED SAMPLES

II.1 Basic principles of spectroscopic studies in liquids

Extension of the photoacoustics to the condensed phase is of recent origin (62). Frequently the terms photoacoustics and optoacoustics are confusingly used to indicate one and the same phenomenon. However, the original Bell's effect was called optoacoustic - it was Rosencwaig (13) who coined the word 'photoacoustics' to emphasize the absorption of radiation by the condensed phase sample followed by microphone detection in the adjacent gas medium (due to diffusion). These two steps, indirect mechanisms of detecting pressure fluctuations is not very efficient due to the acoustic impedance mismatch between the gas and liquid phase. Consequently the gas coupling detection is only suitable for strongly absorbing samples for which most energy is deposited near the surface.
The easiest way to measure weak absorption photoacoustics is to use direct detection of acoustic disturbances in the medium (liquid coupling). Piezoelectric force sensing transducers immersed in the liquid samples are much more sensitive than the microphones. The reason for the preferred use of piezoelectric detectors is due to the small amplitude Δx of the microphone membrane's motion in liquid medium with high density. In general Δx will be proportional to the pressure disturbance Δp is given by (63):

$$\Delta x = \Delta p/\pi\rho\zeta \qquad (20)$$

where ζ is the fluid kinematic viscosity. As the ratio of absolute viscosities of liquid to gas is of the order of 10^3 the amplitude motion Δx in liquid will be thousand times smaller compared to that in air.
Strauss (63) analysed the problem from an acoustic point of view. Since the compressibility of a liquid is much smaller than that of a gas, the particle velocity in liquid is much smaller (for comparable acoustic energies). The continuity requirement at the liquid-gas interface implies equal magnitudes of particle velocities in both media. Hence little of the acoustic energy is transmitted to the gas. This fact is conveniently described

by the mismatch of the acoustic wave impedance Z at the interface ($Z = \rho \cdot v_a$, with ρ = mass density and v_a = sound velocity).
The experiments with liquid samples are mainly carried out with pulsed lasers (large peak power) since the signal, like in photoacoustics on gases, is proportional to power absorbed by the sample. Furthermore it is possible to suppress the background by choosing the proper gate, to "catch" the first peak of acoustic pulse, thereby preventing the detection of parasitic signal originating at the window (..). Short pulse duration does not allow the onset of convection transfer within the medium.
In general, at room temperature, liquids have relatively strong broad absorption bands in the infra-red and weak bands in the visible and near infra-red. Inherently, high sensitivity of photoacoustic technique can be used to accurately measure weakly absorbing solution and for the analysis of highly scattering liquid systems (such as suspensions). By weakly absorbing solution is meant the weakly absorbing species in the solvent (absorbing or not). To find the quantitative relationship between the normalized piezo signal S and the absorption coefficient α_g consider the experimental situations shown in Figure (41) (64).

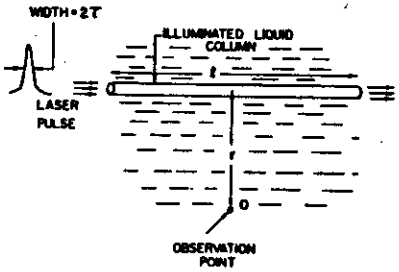

Figure 41. Piezodetection in liquids (65).

The pulse (energy E_o) of laser radiation (width $\tau_p = 2\tau$) and diameter 2R illuminates with repetition frequency f_r the cylinder of absorbing liquid (coefficient α_g and density ρ) having a length L_g. For very transparent liquids $\alpha_g L_g$ is much smaller than the unity resulting in a uniform distribution of absorbed energy across the length L_g. The piezodetector is located at observation point O placed at distance r (shortest distance to the axis of the liquid volume).

Following the excitation (pulse length selected much longer than de-excitation τ_{nr}), the cylindrical acoustic pulse will be generated so that it travels at the speed of the acoustic pulse v_a (medium dependent) across the diameter of the cylinder within the time interval $\tau_a = 2R/v_a$. The amplitude of the cylindrical wave is dependent on distance r from the axis of the illuminated column (r = 0) and is detected by a fast response piezodetector ($\tau_{piezo} \ll \tau_p$) thus: $\tau_p \gg \tau_{piezo}$, τ_{nr} and τ_a.
The amount E_{abs} of energy per pulse absorbed by the liquid column (absorption coefficient α_g and length L_g is, according to Lambert-Beer's Law:

$$E_{abs} = E_o[1 - \exp(-\alpha_g L_g)] \tag{21}$$

reducing to

$$E_{abs} \approx E_o \alpha_g L_g \tag{22}$$

for highly transparent media.

The absorbed energy E_{abs} is fully converted into the thermal energy E_{th} causing the temperature rise ΔT of the liquid volume $V = R^2\pi L_g$. As the $E_{th} = m_g c_p \Delta T$ (m_g is mass of liquid column and c_p its specific heat), one has for ΔT from eqns. (21 and 22):

$$\Delta T = \frac{E_o \alpha_g L_g}{R^2 \pi L_g \rho_g c_p} \tag{23}$$

The temperature rise results in an expansion of liquid column; the radius increases from R to R ΔR ($\Delta R \ll R$). The volume increment ΔV defined as:

$$\Delta V = (R + \Delta R)^2 L_g \pi - R^2 L_g \pi \tag{24}$$

On the other hand, the relative change in volume $\frac{\Delta V}{V}$ is expressed through the volumetric expansion coefficient of the liquid β_f and the corresponding temperature increment ΔT:

$$\frac{\Delta V}{V} = \beta_f \cdot \Delta T$$

Combining eqns. (24) and (25) one obtains for ΔR

$$\Delta R = R\beta_f \Delta T/2$$

which is based upon substitution of ΔT from eqn. (23)

$$\Delta R = E_o \alpha_f \beta_f / 2\pi R c_p \rho \qquad (26)$$

and finally

$$\frac{\Delta R}{E_o} = \alpha_f \beta_f / 2\pi R c_p \rho \qquad (27)$$

which forms the basis of quantitative pulsed studies (65).
In order to get an estimate of ΔR consider the laser output power level (per pulse) $E_o \approx 1 \times 10^{-3}$ J, incident on 1 cm long column (radius 1 mm) of water ($\alpha_f \approx 10^{-3} cm^{-1}$ in visible region, $c_p \approx 10^3$ J $kg^{-1}K^{-1}$, $\beta_f \approx 10^{-4} cm^{-1}$, $\rho = 10^3 kg\ m^{-3}$). The temperature increase ΔT (eqn. (23)) during the time τ_p is then in the order of 10^{-4}K. Likewise, the substitution of numerical values above into eqn. (26) gives $\Delta R \sim 10^{-9}$cm ($\Delta R \ll 1$ mm).
Periodic expansion and contraction produce a pressure wave that propagates outwards with a speed in (radial direction) v_a through the medium. The amplitude of pressure wave depends on the frequency of acoustic pulse $f_a = \frac{1}{\tau_a} = \frac{v_a}{2R}$ and displacement Δx (64) (proportional to ΔR):

$$p = 2\pi f_a \Delta x \rho v_a \qquad (28)$$

i.e.

$$p = \text{const}\ \Delta R\ 2\pi f_a \rho v_a \qquad (29)$$

Substitution for ΔR from eqn. (26) into eqn. (29) yields

$$p = \text{const}\ \frac{E_o \alpha_f \beta_f v_a}{c_p} \left(\frac{f_a}{R}\right) \qquad (30)$$

For constant f_a and R eqn. (30) becomes:

$$p = \text{const}^* \frac{E_o \beta_f \alpha_f v_a}{c_p} \qquad (31)$$

For good piezoceramic detectors [sensitivity10^{-2} to 1 mv/Pa, usable over a wide frequency range (even 100 MHz)] the pressure wave will produce a voltage output signal proportional to the pressure, i.e.

$$V_{piezo} = K^* p = K^* \text{const}^* E_o \beta_f \alpha_f v_a / c_p \qquad (32)$$

with K^* being a constant depending on geometry and response of the transducers. The linear relationship between the piezoelectric signal (generated charge when piezo material is subjected to mechanical stress) and the absorption coefficient is valid for weak absorptions only. The generated charge however, is proportional (63) to the amplitude of the pressure wave causing the deformation (piezoelectric charge coefficient times the deformation area).

Since β_f, v_a and c_p are constant for a given liquid sample, the normalized signal S_n can be written as:

$$S_n = \frac{V_{piezo}}{E_o} K \alpha_f \qquad (33)$$

with K being the proportionality constant.
As seen in eqn. (33) the normalized piezosignal S_n is linearly dependent on the absorption coefficient α_f making the pulsed photoacoustics of liquids indeed a very suitable technique for studying weakly absorbing liquids.
The value of K in eqn. (33) is determined by calibration measurements of V_{piezo}/E_o using the samples with known α_f.
Figure 42 displays a typical design of photoacoustic cell for studies on liquids (4). The material used for cell fabrication should not be be reac-

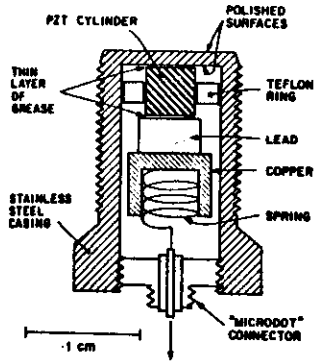

Figure 42. Piezotransducer used by Patel and Tam for studies of weakly absorbing liquids (2).

tive (chemically) with the liquid under investigation and must have negligable adsorbance affinity. As a transducer, a zirconate-titanate-lead ceramics is used in the so called 'enclosed' geometry configuration. This arrangement reduces the influence of signals originating from the light scattered from the bulk (..) that interferes with true signals produced by bulk absorption. In practice the piezoceramics and liquid sample are separated by a thin polished membrane (polished side faces the sample) to reflect all the unwanted bulk scattered light. This membrane is in contact with the piezoceramics to translate the acoustic signals.

Figure 43 displays a liquid photoacoustic cell suitable for rapid studies of flowing samples (66). The cell is mounted in such a way that the influence of external acoustic disturbances is minimized. An inexpensive piezoelectric detector (hydrophone) for efficient transmittance of photoacoustic signals along the preferred polarization direction (chosen during the fabrication) is used. The piezo is separated from the bulk of liquid by means of a thin membrane and a teflon ring. The visible radiation of a laser is coupled into the cell volume through the flat polished side cut in a cylinder wall. Care has to be exercised to prevent the occurence of air bubbles in the cell. The sensitivity of piezo hydrophone is 5 pico Coulomb per unit force, while its internal resistance is 3×10^9 ohms.

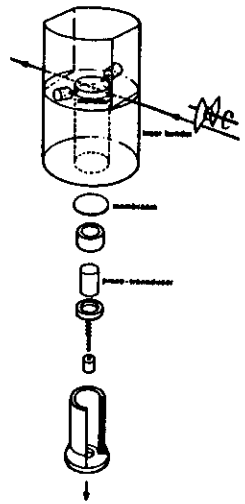

Figure 43. Simple cell with piezotrandsucer for photoacoustic studies of flowing liquid samples (66).

The analysis of signal detection in the case of the modulated continuous excitation is quite complicated and will be omitted here. We shall further discuss the periodic irradiation of liquids when dealing with the technique of mirage spectroscopy. Extensive analysis of optimizing the cell and beam geometrical conditions for detection in liquids is given by Kitamori et al. (67). The group of Sawada at the Tokyo University performed the study of frequency characteristics of the photoacoustic signals directly generated in liquids (68) and discovered the existance of $1/f_m$ dependence (f_m is the modulated frequency).

Main practical application of photoacoustic studies so far has been the ultra low trace detection in various solvents. Table 8 on the next page shows the relevant data gathered with different laser sources (4). Tam even reports detection of eight harmonic overtones of the C-H stretch in benzene (69). Such high sensitivities allow detection in the pptv (1 part in 10^{12}) range. Accurate spectra of liquid water have been determined

Detected component	Solvent	Laser	Absorption coefficient[mol^{-1}cm^{-1}]	Threshold of detection for S/N=1	
				ppt*	ng/ml
β-carotene	chloroform	Ar laser λ=488 nm and 514.5 nm J=0.7 W	$1.82 \cdot 10^5$ $3.7 \cdot 10^4$	12	0.66
cadmium	chloroform	Ar laser λ=514.5 nm J=0.5 W	$7.8 \cdot 10^0$	7	0.01
UO_2^{++}	water	Ar laser λ=514.5 nm	$1.8 \cdot 10^3$		3
benzene	CCl_4	pulsed dye laser λ=607.1 nm		0.15	
vitamin A	H_2O	pulsed H_2 laser λ=0.33 μm		1	$2 \cdot 10^{-3}$
hematoporphyrin	ethanol				0.3
protoporphyrin	ethanol				0.09
chlorophyll b	ethanol				0.3
U(IV)	H_2O	dye laser λ=0.414 μm			$8 \cdot 10^{-7}$ M/L
U(VI)	H_2O	dye laser λ=0.66 μm			10^{-6} M/L

Table 8. Some of the results obtained with the direct piezo detection (4).

(69). This is several orders of magnitude better than $\alpha_g L_g = 10^{-3}$ cm^{-1} sensitivity limit (see Figure 44) normally achievable with the conventional techniques (2). Source sensitivity is obtained with the indirect [piezo → gas) detection in the c.w. modulated laser excitation.

At the moment sensitivity for absorption of $\alpha_g L_g$ as small as 10^{-7}. This also implies that the measurements of heavily absorbing samples ($\alpha_g \approx 10^3$cm^{-1}) can be performed with a very thin monolayer ($L_g = 10^{-10}$m!) when a pulsed laser is used. For weakly absorbing species ($\alpha_g \approx 10^{-7}$cm^{-1}), relatively long sample lengths ($L_g = 1$ cm) are allowed.

Additional sensitivity improvement (to 10^{-9}) is possible before the limiting electrostriction background signal becomes dominant.

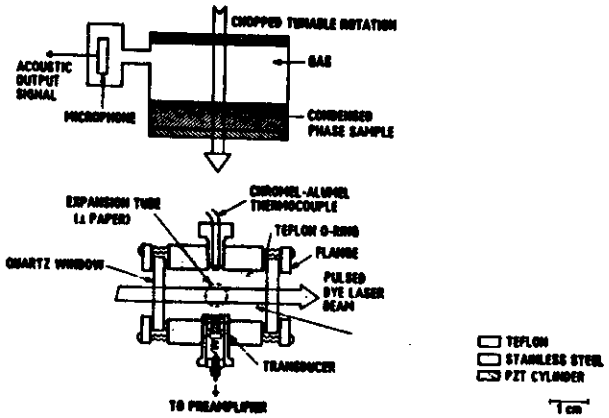

Figure 44. Indirect (a) and direct (b) photoacoustics of condensed phase samples (2).

II.2 Mirage or photothermal deflection technique

In recent years a novel spectroscopic technique has received widespread attention (analytical experimented studies and theory) for analytical studies. It is a method based on generation of photothermal effects - i.e. the occurence of refractive index gradients in the liquid sample due to the temperature rise following the absorption of radiation from a periodically interrupted beam. The heating (and hence the temperature and refractive index gradient) with a 'pump' laser. The magnitude of the refractive effect is then sensed by another probe beam of an optical laser undergoing deflection. Some simple calculations (70) will help us to deduce the magnitude of the photothermal effect produced for absorbing (infra-red) molecules such as benzene ($\rho = 0.88 \times 10^3$ kgm^{-3}, $c_p = 1.72 \times 10^3$ J kg^{-1}k^{-1}, $\alpha_g \approx 10^{-3}$cm^{-1}) illuminated by laser power of $P_o^s = 10^{-2}$W. Sample volume V is specified by length of benzene column (radius R = 10^{-3} m and length $L_g = 10^{-2}$ m)

i.e. $V = 3.14 \times 10^{-8} m^3$. Assuming no other energy dissipation but the thermal one, the amount of power deposited in the sample $P^*_{abs} = P^*_o \alpha_\ell I_\ell = 10^{-8} W$ and hence the resulting rate of temperature increase

$$\dot{T} = \frac{\Delta T}{\Delta t} \quad \frac{10^{-8}}{V\rho\, c_p} = 2.1 \times 10^{-4}\ K\ sec^{-1} \qquad (34)$$

This rise causes the outward heat transfer $\dot{Q}_{out}$ from the heated volume to the surrounding region. The magnitude of flow is given by Fourrier law for conductive transfer:

$$Q_{out} = - \frac{A\ \Delta T}{\Delta x} k_\lambda \qquad (35)$$

where k_λ, A and Δx indicate the thermal heat conduction coefficient of liquid ($k_\lambda = 0.143\ W\ m^{-1}K^{-1}$ for benzene), effective surface ($2\pi RL_\ell = 6.28 \times 10^{-8} m^2$) and thickness across which ΔT is set up. It is clear that the temperature of the sample will tend towards some final value determinec by the equal rates of energy gain (heat input) and loss (heat conduction for the system, i.e.

$$P^*_{abs} = \dot{Q}_{out},\ \text{giving}\ \Delta T/\Delta x = \frac{10^{-8}}{0.143 \times 6.28 \times 10^{-8}}\ Km^{-1} \qquad (36)$$

i.e. temperature gradient equals $1.11\ Km^{-1}$. In practice main portion of the temperature gradient is developed across a distance that equals the laser beam radius: $\Delta x \approx R$. This approximation enables one to calculate $\Delta T = 1.1 \times 10^{-3}$ K (for $\Delta x = 1$ mm).

As the rate of temperature increase is $2.1 \times 10^{-4}\ K\ sec^{-1}$ (see above), the time interval needed to reach $\Delta T = 1.1 \times 10^{-3} K$ is $1.1 \times 10^{-3}/2.1 \times 10^{-4}$ i.e. 5.4 seconds (so called response time). Since $\frac{\Delta T}{\Delta x}$ is inversely proportional to the size of the area A participating in radial heat convection, it is necessary to focus the pump radiation if fast response is required.

The refractive index n of sample is, in general, weakly temperature dependent. Hence, the temperature change ΔT as calculated above, will cause a slight change of the sample itself (or alternatively in another medium in thermal contact with the sample on account of the diffusion process). The use of a beam of radiation which is not absorbed by the sample, allows the probing of the heated sample volume. The most commonly used method is to send the laser beam of visible light (He-Ne at 0.63 μ) through the region of interest (perpendicular to direction of pump beam). In optical portion of electromagnetic spectrum the temperature coefficient $\frac{dn}{dT}$ of the refractive index varies according to (70)

$$\frac{dn}{dT} = \left[\frac{\partial n}{\partial T}\right]_p + \left[\frac{\partial n}{\partial \rho}\right] \cdot \left[\frac{\partial \rho}{\partial T}\right] \qquad (37)$$

For benzene the above equation becomes $\frac{dn}{dT} = -3.9 \times 10^{-4} K^{-1}$ when first term is neglected. For change Δn in the refractive index n, it follows

$$\Delta n = \left[\frac{dn}{dT}\right] \Delta T \qquad (38)$$

giving $\Delta n = -4.3 \times 10^{-7}$ for $\Delta T = 1.1 \times 10^{-3} K$. (The negative sign indicates the expansion of liquid when heated i.e. $\partial\rho/\partial T < 0$). The absorbing liquid behaves as a negative lens with a periodically (at modulation frequency) changing refractive index. The probe beam undergoes the corresponding deflection which can be measured with a position sensitive detector. Variations in thermally induced deflections as small as 10^{-9} radians have already been measured (62). In actual mirage experiments the optically

proved distribution of refractive index in the medium with known $\frac{dn}{dT}$ enables the calculation of the temperature distribution within the sample. However, the temperature is related to the sample absorbance through the thermal properties of the sample and hence its absorption coefficient can be calculated.

II.3 An example: transverse mirage of heavily absorbing liquids

We shall illustrate this approach by describing the mirage spectroscopic studies of organic liquid performed recently in our own laboratory (71).

Consider absorbing liquid samples enclosed in the cell (Figure 45). Periodically modulated "pump" radiation with intensity $I_o(t) = \frac{1}{2}I_o[1 + \exp(i\omega t)]$ irradiates the sample through the transparent window in the positive ℓ direction. The temperature gradient is formed solely in ℓ direction and for such one-dimensional case the temperature oscillation $T(x,t)$ at some distance and certain time instant is given as a sum of two terms: the spatial, time dependent $\bar{T}(x)$ and the fluctuating component $\delta\bar{T}(x,t)$, i.e.

$$T(x,t) = \bar{T}(x) + \delta T(x,t) \tag{39}$$

The a.c. component (modulated at angular frequency ω) satisfies the general heat diffusion differential equation:

$$\rho c \left[\frac{\partial}{\partial t}\right] \delta T(x,t) - k_\lambda \left[\frac{\partial^2}{\partial x^2}\right] \delta T(x,t) = \delta Q_s(x,t) \tag{40}$$

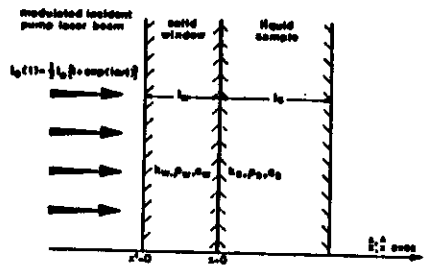

Figure 45. The modulated radiation passes through the transparent window on its way to absorbing liquid sample (71).

where the symbols ρ, c, k_λ and Q_s are used to define density, specific heat conduction coefficient and heat source.
The heat source term Q_s satisfies the equation:

$$Q_s(x,t) = -(\partial/\partial x)\, I(x,t) \tag{41}$$

where $I(x,t)$ is the intensity in the sample at distance related to the intensity $I_o(t)$ through:

$$I(x,t) = I_o(t) \exp(-\beta_s x) \tag{42}$$

with β_s being the sample's absorption coefficient.

Combination of eqns. (41) and (42) gives

$$Q_s(x,t) = Q_s(x) \exp(i\omega t) \tag{43}$$

with

$$Q_s(x) = \tfrac{1}{2} I_o \beta_s \exp(-\beta_s x) \text{ for } o \leq x \leq \ell_s \tag{44}$$

$$Q_s(x) = 0 \text{ elsewhere}$$

In eqn. (44) l_s is the cell length. Likewise, the term $\delta T(x,t)$ can, in general be represented as a product of two independent terms:

$$\delta T(x,t) = \theta(x) \exp(i\omega t) \tag{45}$$

For each of the two regions in Figure 45 (i.e. window and sample indicated by subscripts ω and s) the spatial term in eqn. (45) can be written as:

$$\theta_s(x) = A_s \exp(\sigma_s x) + B_s \exp(-\sigma_s x) + C_s \exp(-\beta_s x) \tag{46}$$

and

$$\theta_w(x) = A_w \exp(\sigma_w x) + B_w \exp(-\sigma_w x) \tag{47}$$

The constant C_w is zero, since there is no absorption in the window. Parameters σ_w and σ_s are imaginary, and their numerical values are equal to the inverse of the thermal diffusion length μ_w and μ_s:

$$\sigma_s = (1 + i)\, \omega/2a_s$$
$$\sigma_w = (1 + i)\, \omega/2a_w \tag{48}$$

with a_s and a_w being thermal diffusivity coefficients ($m^2 sec^{-1}$):

$$a_s = (k^s_\lambda/\rho_s c_s)$$
and
$$a_w = (k^w_\lambda/\rho_w c_w) \tag{49}$$

The constant C_s is obtained by substitution of eqn. into eqn. (40).

$$C_s = -\tfrac{1}{2} I_o \left[1 - (\sigma_s/\beta_s)^2\right]^{-1} (k^s_\lambda \beta_s)^{-1} \tag{50}$$

The remaining four constants A_s, B_s A_ω and B_ω are to be determined from boundary conditions

$$\theta_w(x' = o) = o$$
$$\theta_w(x' = l_w) = \theta_s(x = o)$$
$$\theta_s(x = l_s) = o \tag{51}$$

and
$$- k^w_\lambda \Delta\theta_w(x = l_w) = - k^s_\lambda \nabla\theta_s(x = o)$$

where separate coordinate systems ($\hat{x}'$ and $\hat{x}$) have been chosen for window and sample (l_w is the window thickness). Alternatively, if the front side of the sample is taken as the common origin, the boundary conditions are as follows:

$$\theta_w(x = -l_w) = o$$
$$\theta_w(x = o) = \theta_s(x = o)$$
$$\theta_s(x = l_s) = o \tag{52}$$

and
$$- k^w_\lambda \nabla\theta_w(x = o) = - k^s_\lambda \nabla\theta_s(x = o)$$

Solving the eqns. (45) to (47) with boundary conditions provides a complete expression for the temperature amplitude $\theta_s(x)$ in terms of experimental parameters l_w, l_s, a_s, a_w, β_s, I_o, ω and x:

$$\begin{aligned}\theta_s(x) = {} & \tfrac{1}{2} I_o \{k^s_\lambda \sigma_s [1 - (\sigma_s/\beta_s)^2]\, [1 - \exp(-2\sigma_s l_s)]\}^{-1} \\ & \{[\exp(\sigma_w l_w) - \exp(-\sigma_w l_w)]\, [\exp(-\sigma_s x) - \exp(-\sigma_s(2\, l_s - x))] \\ & [(1 - \exp(-2\sigma_s l_s)) - (\sigma_s/\beta_s)\, (1 + \exp(-2\sigma_s l_s) - \\ & - 2 \exp(-l_s)\, (-\sigma_s + \beta_s)]\, [\exp(\sigma_w l_w) - \exp(-\sigma_w(l_w)) \\ & (1 + \exp(-2\sigma_s l_s)) + \varepsilon\, (\exp(\sigma_w l_w) + \exp(-\sigma_w l_w) \\ & (1 - \exp(-2\sigma_s l_s))]^{-1} + [\exp(-\sigma_s x) - \exp(-\sigma_s(2\, l_s - x)) + \\ & + (\exp(\sigma_s x) - \exp(-\sigma_s x))\, \exp(-l_s(\sigma_s + \beta_s)) - \\ & - (1 - \exp(-2\, l_s \sigma_s))\, \exp(-\beta_s x)]]\end{aligned} \tag{53}$$

In eqn. (53) g is dimensional ratio of thermal effusivities ($Wm^{-2}K^{-1}sec^{\frac{1}{2}}$)

$$g = (k_\lambda^w c_w \rho_w / k_\lambda^s c_s \rho_s)^{\frac{1}{2}} \tag{54}$$

Now let us concentrate on heavily absorbing liquids. For thermally thick samples $|\exp(-2\sigma_s \ell_s)| \ll 1$.
Furthermore, on physical grounds for the heat flux F_w

$$\delta F_w(x,t) = -k_\lambda^w \nabla \delta \theta_w(x,t) = -k_\lambda^w \nabla \theta_w(x) \exp(i\omega t) \tag{55}$$

Therefore it holds true that

$$|\delta F_w(x = o)/\delta F_w(x = \ell_w)| \ll 1 \tag{56}$$

from which $|\exp(-2\ell_w \sigma_w)| \ll 1$ (57)

with the approximations (57), the following relationship for $\theta_s(x)$ is obtained:

$$\theta_s(x) = \frac{I_o}{2 k_\lambda^s \sigma_s [1 - (\sigma_s/\beta_s)^2]} \{\exp(-\sigma_s x)(1 - \sigma_s/\beta_s)(1 + g)^{-1} + \exp(-\sigma_s x) - \exp(-\beta_s x)\} \tag{58}$$

By introducing dimensionless variables $\epsilon = x/\mu_s$ and $\kappa = \mu_s \beta_s$ it becomes easier to group real and imaginary terms in the above equation.
The magnitude of $\theta_s(x)$ is then:

$$|\theta_s(x)| = I_o \mu_s \exp(-\epsilon)/2^{3/2} k_\lambda^s (1 + g)(1 + 4\kappa^{-4})]$$
$$\{(2 + g - \kappa^{-1})^2 + (\kappa^{-1})^{-2} + (1 + g)^2 \exp(2\epsilon) \exp(-2\beta_s x) +$$
$$+ 2(1 + g) \exp(\epsilon) \exp(-\beta_s x)[\kappa^{-1} \sin\epsilon - (2 + g - \kappa^{-1}) \cos\epsilon]\}^{\frac{1}{2}} \tag{59}$$

In photothermal detection scheme, the angle of deflection is proportional to a temperature gradient. The heat flux through the sample is governed by:

$$\delta F_s(x,t) = -k_\lambda^s \nabla\theta_s(x) \exp(i\omega t) \tag{60}$$

Using eqn. (53) for $\theta_s(x)$ and the approximations

$|\exp(-2\sigma_w \ell_w)|$ and $|\exp(-2\sigma_s \ell_s)| \ll 1$
and

$$\nabla \theta_s(x) = -\frac{I_o}{2}[1 - (\sigma_s/\beta_s)^2]\{1 + \exp(-\sigma_s x)(1 - \sigma_s/\beta_s)/(1 + g) - \exp(-\beta_s x)\beta_s/\sigma_s\} \tag{61}$$

Substituting again $\epsilon = x/\mu_s$, $\kappa = \mu_s\beta_s$ and eqn. (48) for σ_s into above equation, the magnitude of temperature gradient is:

$$|\nabla \theta_s(x)| = [I_o/2 k_\lambda^s (1 + 4\kappa^{-4})^{\frac{1}{2}}]\{[(2 + g - \kappa^{-1})^2 + \kappa^{-1})^2] \exp(2\epsilon)/(1 + g)^2 + \tfrac{1}{2}\kappa^2 \exp(-2\beta_s x) + \exp(-\epsilon) \exp(-\beta_s x)/(1 + g)[\sin\epsilon - \cos\epsilon - (2 + g - \kappa^{-1})\kappa (\sin\epsilon + \cos\epsilon)]\}^{\frac{1}{2}} \tag{62}$$

It is not trivial to express the absorption coefficient β_s from eqn. (62) in terms of gradient $|\nabla\theta_s(x)|$.
In order to deduce somewhat simpler equation, we rewrite the eqn. (62) as a sum of three terms S_2, S_5 and S_6 multiplied by a constant factor C_1, i.e.:

$$|\nabla \theta_s(x)| = C_1 (S_2 + S_5 + S_6)^{\frac{1}{2}} \tag{63}$$

with

$$C_1 = I_o/2k_\lambda^s (1 + 4(\mu_s\beta_s)^{-4})^{\frac{1}{2}}$$
$$S_2 = [(2 + g - (\mu_s\beta_s)^{-1})^2 + (\mu_s\beta_s)^{-2}] \exp(-2x/\mu_s)/(1 + g)^2$$
$$S_5 = \tfrac{1}{2}(\mu_s\beta_s)^2 + \exp(-2\beta_s x) \quad \text{and}$$
$$S_6 = (1 + g)^{-1}) \exp(-x/\mu_s) \exp(-\beta_s x)[\sin(x/\mu_s) - \cos(x/\mu_s) - (2 + g + (\mu_s\beta_s)^{-1})\mu_s\beta_s (\sin(x/\mu_s) + \cos(x/\mu_s))] \tag{64}$$

From these terms S_5 is the most convenient to work with. To make it dominant S_5 must be much larger than S_2 and S_6. Under these conditions, the eqn. (63) reduces to

$$| \nabla \theta_s(x) | C_1 S_5^{\frac{1}{2}} = C_1 (0.5)^{\frac{1}{2}} \beta_s \mu_s \exp(-\beta_s x) \quad (65)$$

or

$$| \nabla \theta_s(x) | = \Psi(\beta_s, \omega) \exp(-\beta_s x) \quad (66)$$

The function $\Psi(\beta_s, \omega)$ is dependent on modulation frequency $\omega = 2\pi f_m$ and absorption coefficient β_s.
Due to the proportionality of normalised deflection signal $S_n(x)$ at some distance x and the temperature gradient $| \nabla\theta_s(x) |$ we can write:

$$S_n(x) \sim \Psi(\beta_s, \omega) \exp(-\beta_s x) \quad (67)$$

When the cell with the sample is displaced through a distance Δ, to a new location $x + \Delta$ and other experimental conditions remain the same, the normalized photothermal deflection signal is

$$S_n(x + \Delta x) \sim \Psi(\beta_s, w) \exp[-\beta_s (x + \Delta)] \quad (68)$$

By taking the ratio of two signals function $\Psi(\beta_s, w)$ is cancelled out and the absorption coefficient β_s is given by

$$\beta_s = (\Delta)^{-1} \ln S_n(x)/S_n(x + \Delta) \quad (69)$$

The absorption coefficient of the material sample can, this particular case, be determined by mirage technique if the two normalized signals and the relative distance between the two locations at which the sampling takes place, are known.

The validity of the theoretical expression derived above will now be tested in a spectroscopic study of methyl alcohol in the CO_2 laser emission wavelength range. The experimental set up used in this study is shown in Figure 46. A CO_2 waveguide laser operating in free running mode delivers about 2W at its strongest transition (linearly polarized). About 10% of the emerging laser power is sampled out for monitoring (power detector PM) and normalization purposes by the ZnSe beam splitter BS. The remaining laser power impinges on the spherical mirror with focal length L_1 of 550 mm which focusses the pump radiation onto the sample S (the induced photorefractive effect is inversely proportional to the volume of the heated region). On its way to the sample in the measuring cell, the beam is interrupted by a mechanical chopper (long term stability $1:10^4$) that could be adjusted to any frequency within 0 and 3.5 kilohertz. In order to prevent spatially non-uniform effects (multimoding or two line oscillation at the same time) in the sample that could lead to uncontrolled perturbation and erroneous interpretation, diffusing structure Dif was inserted between the chopper and the sample. It is a 8 x 6 x 65 mm hollow piece of brass which has been sand blasted (on its inner walls) and then coated with gold to ensure good reflectivity. The axis of a diffuser subtends an angle of 23° with respect to the direction of the incident pump beam. The mirror L_1 focusses the CO_2 laser radiation (at wave length of interest) on the vertical wall of the diffuser in the immediate vicinity of the front opening so that a sufficient number of diffuse reflections are made across the diffuser length. Of course, diffusing the beam will provide uniform intensity across the heated surface of 6 x 6 mm in the sample, but the power per unit area will simultaneously decrease, which in turn limits the sensitivity.
The back opening of the diffuser was positioned against the ZnSe window W of the sample cell (box with top side open) made of clear glass plates (2 mm thick) which were glued together. The window, 2 mm thick and 25 mm in diameter, is glued to the inner wall of the cell to cover a 20 mm diameter hole drilled in the glass. The cel, is held in a holder affixed to the top plate of the rotating stage which is mounted on the pillar resting on the carrier and optical bench (see Figure 47). The carrier could be displaced in a direction perpendicular to the bench longitudinal axis by means of

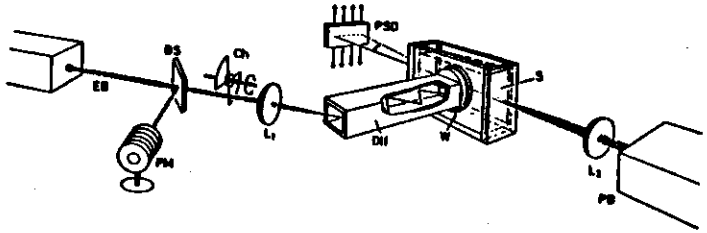

Figure 46. Experimental arrangement mirage spectroscopic study on liquids (71).

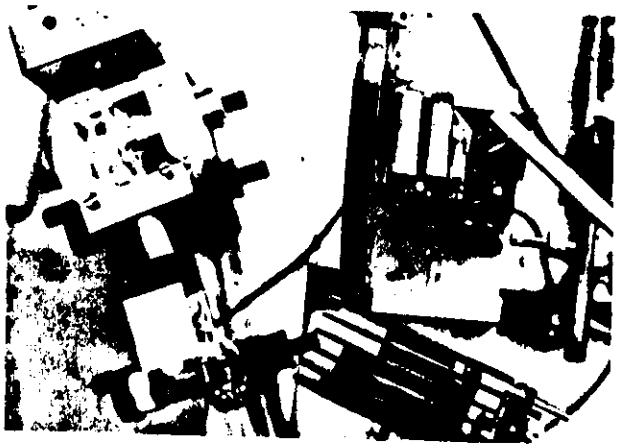

Figure 47. Photograph (from above) of the experimental system. Showing the probe laser beam and position sensitive reflector.

positional micrometer providing the resolution of 5 microns. In such a way the entire cell assembly could be moved without changing the angle between the laser beam and diffuser axis A NEC GLG - 5012 He-Ne laser (also positioned on the same bench as the measuring cell) of good pointing stability served as the probe beam PB. Its radiation was sent from the air through

the glass plate at right angles to the pump beam. The visible radiation of the laser is collected by a lens with a focal length of 40 mm to form a small spot in the sample volume behind the window. The probe beam is thus coplanar with and orthogonal to the modulated pump beam.

The magnitude of deflection of the He-Ne laser beam is detected with a phase sensitive lock-in amplifier at the modulated frequency using the PIN LSC/5D lateral position sensitive diode PSD manufactured by the United Laser Technology (Figure 48) that converts the deflection into voltage.

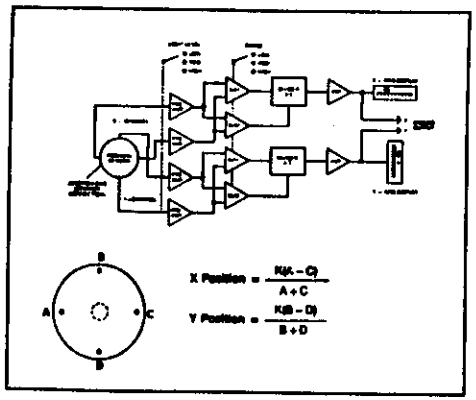

Figure 48. Circuit diagram for characterizing light spot position on a lateral diode (United Laser Technology).

This diode is shielded for stray light and mounted on the stack of horizontal and vertical positioning stages placed again on the same optical bench. In an actual measurement the cell is displaced parallel to the window (in direction perpendicular to the window plane), so that the distance between the probe beam and the window increases with each successive measurement. At given sampling distance x, the position of PSD was adjusted (with laser radiation blocked) to compensate for a d.c. heating effect - this was taken as a zero deflection signal. For each x the phase of the signal is optim-

ized - the procedure is repeated when the laser is tuned into another emission line. The output voltage of the lock-in power amplifier at specific laser wavelength is recorded simultaneously with the power measured at the PM detector. By rationing the two d.c. voltages normalized signal $S_n(x)$ is obtained. When the cell is displaced through a distance Δ, measurement is, reported at identical experimental conditions, yielding $S_n(x + \Delta)$. The value of β_s is then found from eqn. (69). In this experiment the absolute value of x is not measured - instead only Δ is relevant and can be found from the two readings of the sampling distances. However, the choice of the range of x values is not arbitrary, as the above expression for β_s is valid only for the situations for which $S_5 >> S_2$ and S_6. Thus there will be, in general, a range of allowed x values (above some critical onset value) depending in principle on the modulation frequency, f_m and the absorption coefficient β_s.

The relevant thermophysical properties of methyl alcohol and the window needed to calculate the terms S_5, S_2 and S_6 are as follows: l_s = 18 mm l_w = 2 mm, k_λ^s = 0.2023 $Wm^{-1}K^{-1}$, k_λ^w = 16.75 $Wm^{-1}K^{-1}$, ρ_s = 0.79 x $10^3 kgm^{-3}$, ρ_w = 5.72 10^3 kgm^{-3}, c_s = 2.55 x 10^3 J $kg^{-1}K^{-1}$, c_w = 0.327 x 10^3 J $kg^{-1}K^{-1}$. From these values one calculates for thermal diffusion coefficients a_s = $k_\lambda^s / \rho_s c_s$ = 1 x $10^{-7} m^2 sec^{-1}$ and a_w = 89.6 x $10^{-7} m^2 sec^{-1}$. Likewise for thermal effusivities $k_\lambda^w \rho_s c_s)^{1/2}$ = 639 $Wm^{-2}K^{-1}sec^{1/2}$ and $(k_\lambda \rho_w c_w)^{1/2}$ = 5600 $Wm^{-2}K^{-1}sec^{1/2}$ giving for g factor a value of 8.76. In our calculations for terms S_2, S_5 and S_6 we assume the output laser power of 2 W and the spot size of 5 mm immediately near the output hole of the laser which gives a power (intensity) I_o = 1 x 10^3 Wm^{-2}. The intensity of the laser radiation per unit surface at the measuring plane (behind the window) is much smaller (some constant factor) but it is not measured.

Figures 49a to 49d shows the values of S_2, S_5 and S_6 versus a distance x for the sample with absorbtion coefficient β_s of 0.1 x $10^6 m^{-1}$ (100 cm^{-1}) for the range of modulation frequencies from 50 Hz to 2kHz. The plot along

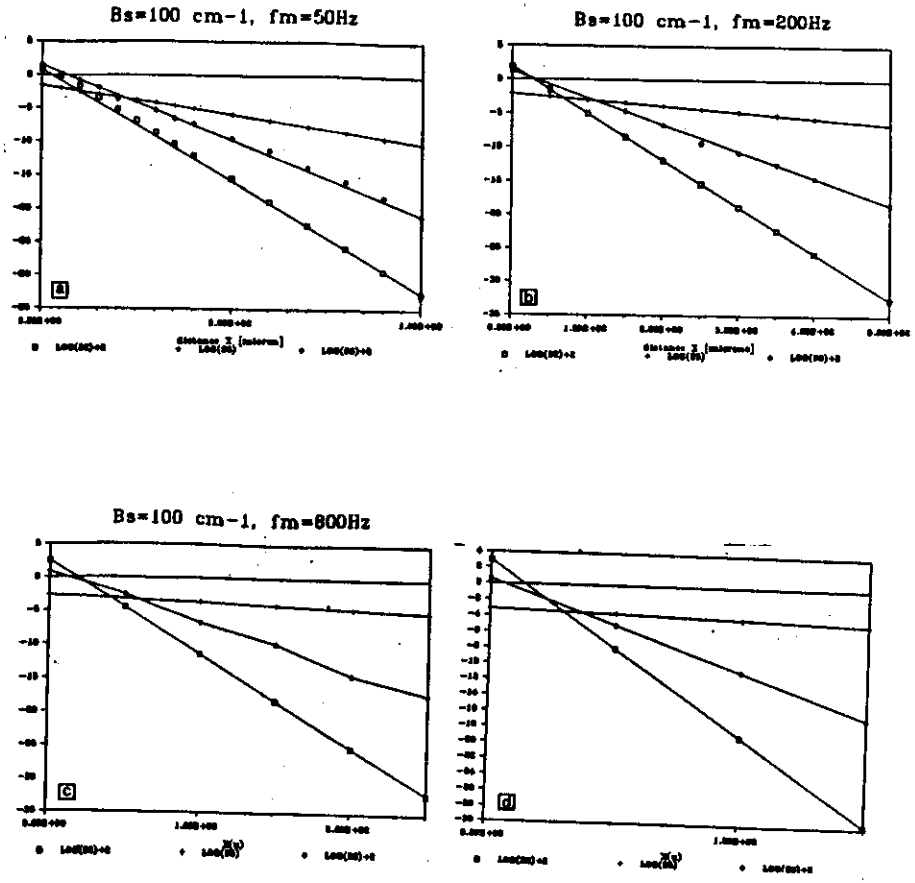

Figure 49. The magnitude of terms S_2, S_5 and S_6 from eqn. (64) versus distance x for sample with absorption coefficient β_s = 100 cm^{-1} at 50Hz (a), 200 Hz (b), 800 Hz (c) and 2000 Hz (d) (71).

the Y-axis is a logarithmic one, since we are interested in the regions of x for which $S_5 >> S_2$ and S_6 (here chosen as $S_5 \geq 100\ S_2$ and $S_5 \geq 100\ 100\ S_6$. In a similar fashion plots for larger β_s (800 cm^{-1}), are produced for the same range of modulation frequencies (see Figures 50A to 50d). All plots indicate that in general the range of x values decreases with increasing modulation frequency for a given sample with given β_s.
The functional dependence of temperature gradient $|\nabla\theta_s(x)|$ on the distance x in the sample was calculated using eqn. 66) for sample with β_s = 100, 200, 400 and 800 cm^{-1} and the modulation frequencies of 50, 200, 800 and 2000 Hz. (Figures 51a to 51d). To get the strong photothermal deflection signals, the value of $|\Delta\theta_s(x)|$ should be as large as possible. We therefore introduce the additional criterion stating that only those x values for which $|\Delta\theta_s(x)| \geq 10^{-2}K\ mm^{-1}$ will be considered.

The analysis of plots in Figures 49a to 49d reveals the following: at a given β_s (for example $\beta_s = 0.1 \times 10^6 m^{-1}$) the distance x (onset value) at which the S_5 is greater than 100 times S_2 and S_6, reduces from 150 microns (at 50 hz) to 40 microns (at 2000 Hz). The same tendency is observed for larger β_s as well. However, the onset value at large β_s is always larger than the corresponding value at low β_s irregardless the modulation frequency f_m. Although there is a broad range of locations within the sample for which $S_5 \geq 100\ S_2$ and $100\ S_6$ the second requirement i.e. $|\Delta\theta_s(x)| \geq 10^{-2}K\ mm^{-1}$ must be met as well. For example in the case of the sample with absorption coefficient $\beta_s = 0.1 \times 10^6 m^{-1}$ (100 cm^{-1}) the range of allowed x values with regard to $|\Delta\theta_s(x)|$ may not exceed 500 microns (at 50 Hz) and 25 microns (at 2000 Hz). This range becomes even shorter at increasing β_s values [at β_s = 800 cm^{-1}: 110 microns (at 50 Hz) and about 15 microns from the window at the modulation frequency of 2 kHz)]. This all leads to the conclusion that for practical reasons the measurements will be limited to the samples having absorption coefficients that are no larger than 0.3×10^6 m^{-1}(300 cm^{-1}).

We have selected two CO_2 laser lines where a reasonable amount of power is available: the 10 P (20) at 10.59 microns and 10 R(20) at 10.26 microns

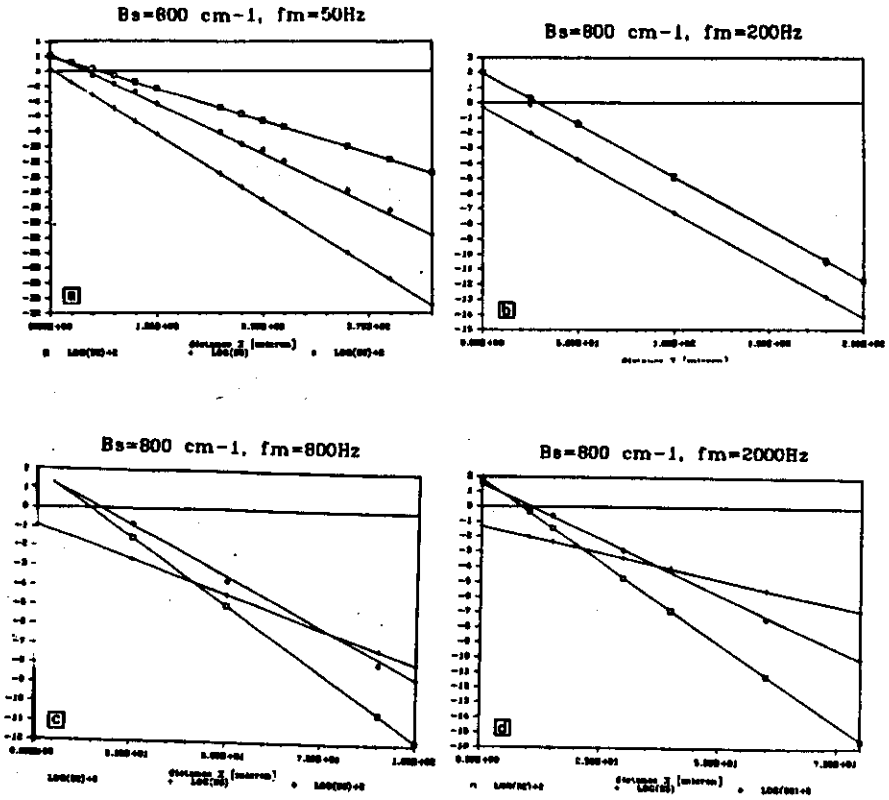

Figure 50. The magnitude of terms S_2, S_5 and S_6 versus distance x for samples with absorption coefficient of 800 cm^{-1} at 50 Hz (a), 200 Hz (b), 800 Hz (c) and 2000 Hz (d) (71).

both in the central portion of the 10P and 10R band respectively. The absorption coefficient of methyl alcohol at these wavelengths are 0.12 x 10^4 and 0.175 x $10^6 m^{-1}$ as found in the product catalogue data (49). The modulation frequency of 240 Hz was chosen. The inspection of Figure 49b for

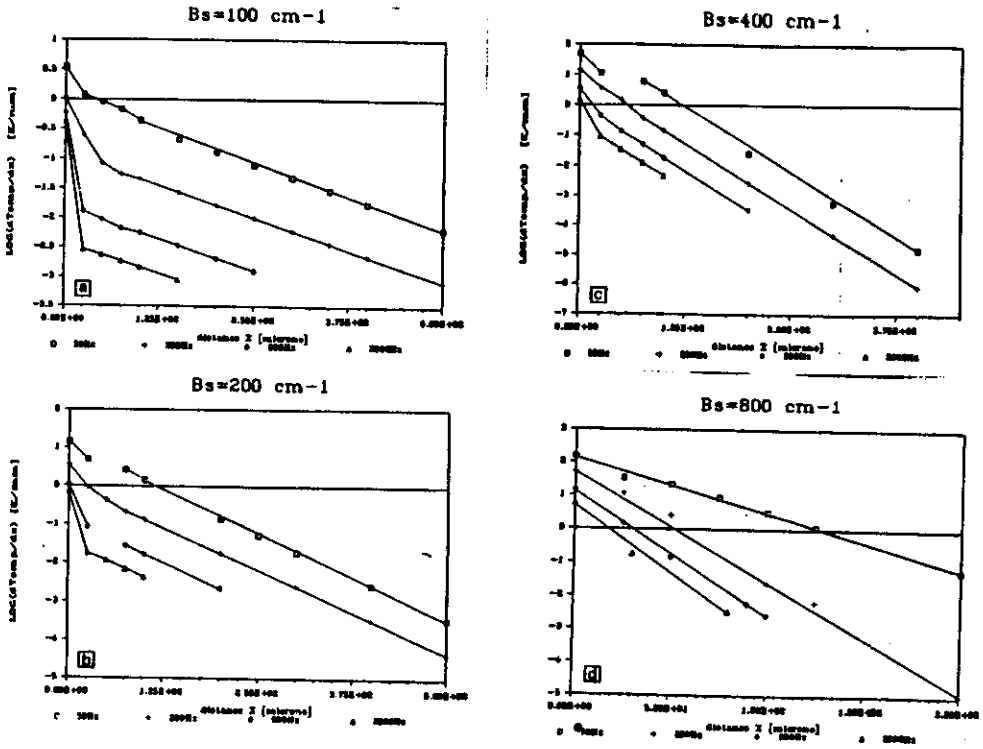

Figure 51. Temperature gradient $|\nabla\theta_s(x)|$ versus distance for four distinct values of modulation frequencies 50 Hz, 200 Hz, 800 Hz and 2000 Hz respectively (eqn. (65)). The absorption coefficient β_s of the sample is 100 cm^{-1}(a), 200 cm^{-1}(b), 400 cm^{-1}(c) and 800 cm^{-1} (d) (71).

β_s = 100 cm^{-1} and f_m = 200 Hz, which is close to our situation, reveals that the S_5 term is dominant at x > 110 microns. On the other hand $|\Delta\theta_s(x)| > 10^{-2}$ K mm^{-1} for 110 μm < x < 250 μm thereby specifying the allowed region as 110 μ < x < 250 μm.

The normalized photothermal deflection signals were recorded (starting from the onset reference position that should be within 150 and 250 μm from the window) at the increment of Δ = 10μm. The mean value was obtained by averaging the ratios (for example $[S_n(x)/S_n(x + 10\ \mu m)$, $S_n(x)/S_n(x + 20\ \mu m)$, $S_n(x)/S_n(x + 30\ \mu m)]$ etc. The cell was manually displaced by means of the micropositioner (resolution 5 μm).

The experimentally determined absorption coefficients were (0.122 ± 0.010) x $10^3 m^{-1}$ 10P(20) and 0.162 ± 0.017) x $10^3 m^{-1}$ at 10R(20) in good agreement with the expected values. Unfortunately, the power of the laser in the 9 micron range was, under the given conditions, not sufficient to produce measurable deflection.

We have also done some measurements on distilled water samples ($\beta_s \approx 0.9$ x $10^3 m^{-1}$) but only on few trials were the measured values close to those we expected. The main reason for these kind of difficulties is that the allignement as well as the placing of the He-Ne laser probe beam within the allowed region, becomes steadily narrower and shifts towards the window surface with increasing β_s. Focussing the probe beam to a smaller spot may help to aleviate this problem.

II.4 Soilless growth

Water is a biological liquid of great importance frequently used as a solvent in agricultural practice. In many of the applications the aqueous solution has to be analysed specroscopically. Although water is practically transparent in the visible, its absorption increases rapidly at wavelengths larger than 4 microns. Near the 10 microns the absorptia coefficient has a value close to 1000 cm^{-1} making the spectroscopic studies in the infra-red

only possible for very thin fluid films (several microns thick). One practical sample of infra-red analysis of aqueous solutions is the investigation of water soluble, ionic inorganic compounds used as nutrients for plants. During the last five years a number of experiments have been carried out in the field of the so-called 'soilless growth'. Instead of growing in the conventional soil, tomato plants grow on a substrate (Rockwoll) cube which contains all the necessary nutrients (micro and macro elements in a certain proportion) supplied in the streaming or closed circulation regime, of water (one controls the mineral content at will).
The pH factor of the solution is measured and computer controlled. For optimal growth selective concentration measurements of sulphates, carbonates, phosphates etc. are preferred. Phosphates and sulphates have relatively strong absorption bands in the region covered by the CO_2 laser emission. For practical application analysing the solutions with transmittance spectroscopy (very thin films) is not very attractive for on-line measurements. Mirage photothermal deflection method does not suffer from this intrinsic limitation. Although all the mirage physics take place within a very small region behind the window, there is enough room to manipulate the probe beam.

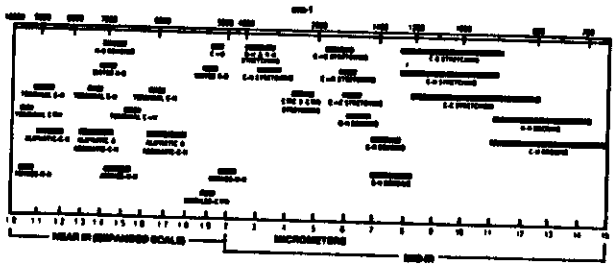

Figure 52. The functional group chart throughout the infra-red region (72).

The above mentioned example is certainly not the only application. Other possible applications involve monitoring (on stream analysis) of concen-

tration of components such as sugar, inorganic compounds such as sodium lauryl sulphates in shampoos, carbohydrates, fat or protein in food processing plants (72). Other organic compounds that have characteristic bands (Figure 52) in the infra-red can be studied as well (information of transisomer in vegetable oil dehydrogenation process). Recently an apparatus Liquid analyser monitor LAN-I based on the infra-red absorption by total cylindrical internal reflection scheme (Figure 53) has been brought on the market.

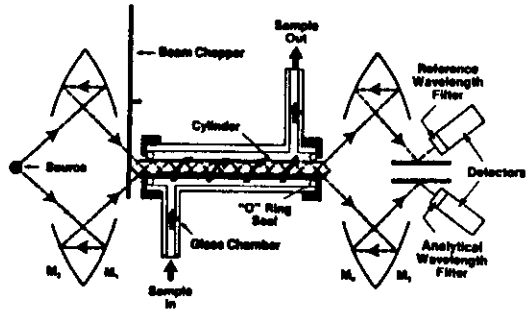

Figure 53. LAN-I liquid infra-red analyser (for flowing liquid samples) operating on the principle of total internal reflection (72).

Initial measurements performed with LAN-I analyser indicated that 1 moler solution of KNO_2 and $KHPO_4$ in water could readily be detected even when both are simultaneously present as shown in Figure 54 Concentrations in the range of 10 mmole/liter are considered as a practical limit in this approach.

Nordal and Kanatad (4) studied the spectra of aqueous solutions of (distilled, deionised water) glucose and the ammonium sulphate with a pulsed CO_2 laser and identified the ν_1 mode of SO_4 mode in ammonium sulphate. In particular $(NH_4)_2SO_4$ is important in its relationship to the water pollution. The authors used photoacoustic differential detection technique and achieved a detection limit of 100 mg $(NH_4)_2SO_4$/kg solution.

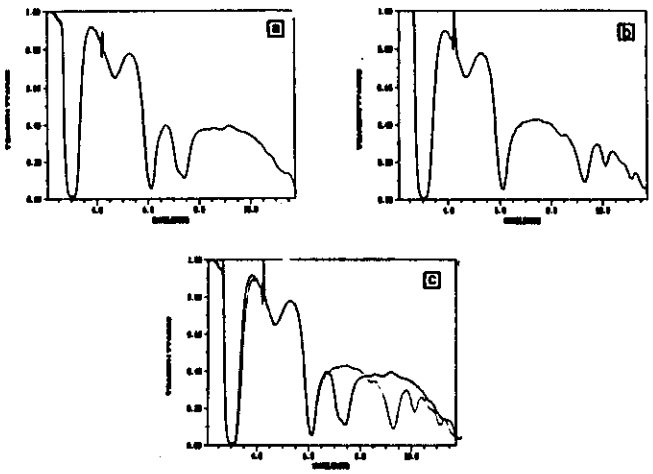

Figure 54. The LAN spectrum of aqueous solution of phosphates and nitrates. Left: 1 molar aqueous solution of KNO_2, midd. 0.6 molar aqueous solution of K_2HPO_4. Right: both solutions together (73).

II.5 Modified mirage

Mirage spectroscopy, actually a laser induced crossed-beam thermal lens, is designed to probe small volumes. An important advantage above the other absorbance measurements is that the signal generation takes place within the volume formed by two focussed intersecting laser beams. The high spatial resolution and sensitivity potentially attainable by this method was used in conjunction with liquid (capillary separation) chromatography on the detection side. Instead of monitoring deflection, one can also measure the effect of cylindrical lenslike elements (absorbing sample) on the probe beam detecting the changes in the far field intensity (by means of a pin hole of the beam along the axis (Figure 55).

In deflection technique the temperature rise formed by the chopped beam is probed off axis at the maximum of the temperature gradient, and the beam is

deflected away from the heated region. This in contrast to the modified mirage approach where the temperature rise is probed on the axis at the minimum of the temperature as a result the beam will be defocussed (negative lens) equally on both sides of the heated region. The complete theory for this method providing linear measure of sample's concentration and absorbivity is given by Dovichi et al (76). With such a modified mirage method Nolan and Dovichi report detection limit as on average 120 iron-1,10 phenathroline molecules within 0.2 pL probe volume using a 100 mW pump laser beam (77). Recently the same authors (78) separated dimethylaminoaxobenzene sulfonyl (DABYLS) derivates of amino acids (molar absorbivity 3 x 10^4 $LM^{-1}cm^{-1}$ at Argon laser pump wavelength] with subfemtomole detection limit.

Dovichi also developed the differential thermal lens calorimetry with reference and unknown samples located on opposite sides of the beam waist and applied the crossed beam thermal lens technique to probe the flow velocity in 0.2-30 mm/sec in liquid streams (76). In the near future an experimental attempt will be made to use photothermal deflection to study the phenomenon of biofouling associated with absorption of proteins from aqueous solutions (biofluids) at specific surfaces (79). In many medical and technical applications, proteins are adsorbed first, and subsequently

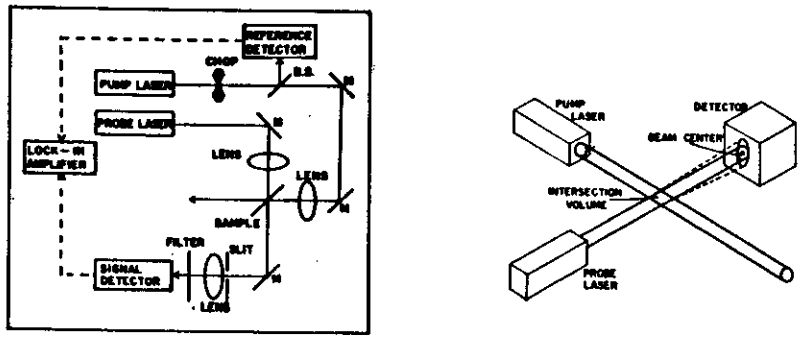

Figure 55. Detection of the far field intensity changes of the probe beam: general set up (a), geometry of two crossed (b) beams (75).

biological cells (bacteria) may adhere on top of the adsorbed layer (food processing equipment, ship hulls, artificial kidneys, thrombus development). Also determination of the thermal conductivity coefficients of organic liquid is generally quite tedious, and worth trying by mirage spectroscopy.

II.6 Mirage on solids

Mirage technique is easily extended to solids as well (Figure 56). The

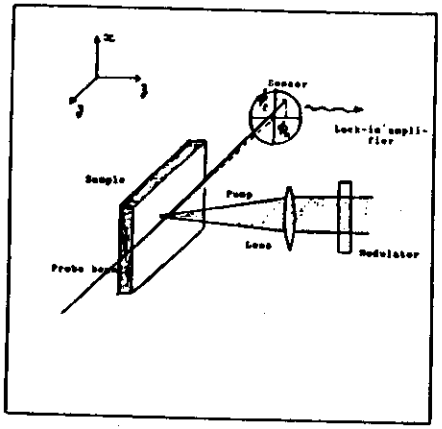

Figure 56. Vector deflection of beam probing the temperature gradient induced by the pump radiation (62).

'pump radiation' from dispersive system or a laser is absorbed by a sample and produces, in general, a time dependent temperature distribution (and hence of refractive index n) around the pump beam that is sensed by the probe beam (sent along ϑ direction). The thermally induced deflection vector has two components i.e. tangential ϕ_t and normal ϕ_n (with respect to the propagation direction), the magnitudes of which are given by (62):

$$\phi_t = \int_{\ell_i} \frac{1}{n}\left[\frac{dn}{dT}\right]\cdot\left[\frac{dT}{dx}\right] dy \qquad (70)$$

and

$$\phi_n = \int_{\ell_i} \frac{1}{n}\left[\frac{dn}{dT}\right]\cdot\left[\frac{dT}{dz}\right] dy \qquad (71)$$

Both integrals are taken along the interaction length ℓ_i (overlapping region between the two beams). Experimentally, the least complicated configuration (ϕ_n deflection will be in the ϑ-z plane) is that of transverse deflection in which the probe beam senses the thermal gradient in adjacent, transparent gas layer (Figure 57). Since the angular deflection depends on $\frac{dn}{dT}$ it is, for higher sensitivity, more convenient to probe in organic liquid medium than in gas (for chloroform CCl_4 $n = 1.45$ and $\frac{dn}{dT} = 5.8 \times 10^{-4}$, hence $\frac{1}{n}\frac{dn}{dT} = 4 \times 10^{-4}$, compared to $n = 1$, $\frac{dn}{dT} = 10^{-6}$ giving $\frac{1}{n}\frac{dn}{dT} = 1 \times 10^{-6}$ for air).

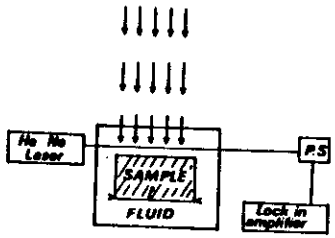

Figure 57. Transverse mirage detection applied to solid samples (80).

The magnitude of ϕ_n component is obtained from the above equation (71).

$$\phi_n = \frac{\ell_i}{n}\frac{dn}{dT}\cdot\frac{dT}{dz} \sim \frac{\ell_i}{n}\frac{dn}{dT}\cdot\frac{\Delta T}{\mu_f} \qquad (72)$$

where μ_f is the thermal diffusion length in the probed fluid at the modulation frequency $w = 2\pi f_m$ given by:

$$\mu_f = \sqrt{\frac{k_\lambda^f}{\rho_f c_f \cdot \pi f_m}} = \sqrt{\frac{a_f}{\pi f_m}} \qquad (73)$$

(k_λ^f, ρ_f and c_f, a_f are thermal conductivity coefficient, density, specific heat and thermal difusivity of the fluid). At frequency of 10 Hz for example, μ_f in air is 1.2 mm compared to 44 microns in chloroform. As the position sensitive devices capable of detecting 10^{-9} radians are available, the limiting temperature difference is from eq. (72)

$$\Delta T_{min} \sim \phi_n \, n \, \frac{dT}{dz} \cdot \frac{\mu_f}{\ell_j} \qquad (74)$$

giving 10^{-3}K in air and ~10^{-7}K in chloroform if ℓ_j = 1 cm.

For optically thin sample (absorption (β_s) is considerable, i.e. $1/\beta_s$ is smaller than the physical length ℓ_s of sample) the deflection is directly proportional to $\beta_s \ell_s$ for thermally thin sample ($\mu_s < \ell_s$) and to $\beta_s \mu_s$ for thermally thick samples. Sensitivity limits $\beta_s \ell_s$ reached by transverse deflection are about 10^{-4} (for gas fluid) and ~10^{-6} (for liquid as probing fluid) for 1 watt of incidental power (62).

Colinear mirage approach allows, in principle, long interaction lengths ℓ_j (not equal to ℓ_s) enhancing the sensitivity $\beta_s \ell_j$. For optically thick samples (weak absorbing) ($\beta_s >> \ell_s$) deflection is proportional to $\beta_s \ell_j$. Mirage method has two significant advantages above the photoacoustics: a) it does not require placing of the sample in a specially suited cell (no scattering background) and b) optical detection allows the operation at high modulation frequencies (62). The ultimate limitation on the sensitivity is imposed by the noise produced by vibrations and the pointing noise of the probe beam. Table 9 displays some of the experimental data gathered with mirage spectroscopy on samples in the condensed phase (62) as compared to other techniques.

Technique	Samples Already Studied	Experimental Set Up	Sensitivity $(\alpha\ell)_{min}$ a Pump Power (W)^a	Probe Beam	Sensitivity to Scattered Light	Special Features
TL	Liquids	Difficult to align	10^{-7} - 10^{-8}	Sensitivity to pointing and intensity noise	No	No mechanical contact. Permits hostile environment and in situ measurements.
Microphone PAS	Solids (bulk, powder), liquids, & gases	Simple to align	~10^{-6} - 10^{-5} solids 10^{-3} gases		Yes	Sensitive to mechanical and accoustical noise
PZT PAS	Solids (bulk) liquids	Simple to align	~10^{-3} (10^{-9} J pulsed)		Yes	Sample attachment difficult.
Collinear PDS	Optically clean transparent solids, liquids & gases	Difficult to align	~10^{-7} -10^{-8} (10^{-10} J pulsed)	Sensitivity to pointing noise Sample transparent to probe	No	No mechanical contact. Permits hostile environment and in situ measurements.
Transverse PDS	Condensed phase samples	Simple to align	~10^{-5}	Sensitivity to pointing noise	No	No mechanical contact. Permits hostile environment and in situ measurements
Interferometry	Liquids & solids	Difficult to align	~10^{-7} -10^{-8}	Sensitive to intensity noise Sample transparent to probe beam	No	No mechanical contact. Permits hostile environment and in situ measurements.

Table 9. Comparison of thermal lensing (TL), photoacoustics (PAS), piezotransducer detection (PZT) and the mirage (PDS) (62).

II.7 Photoacoustic spectroscopy of solid samples

Consider the solid material sample (length L) and gas layer on top of it (Figure 58). The solid material has an absorpotion coefficient β_s and the gas is considered to be transparent (optically). This two-layered structure is illuminated by modulated beam (frequency $\omega = 2\pi f_m$) of radiation: $I(t) = I_o \sin\omega t$ (Figure 59a). Solid layer absorbs the radiation according to Lambert Beers law ($I(x) = I_o e^{-\beta_s |x|}$. Collisional de-excitation mechanism gives rise to a generation of heat in the sample, modulated at the same frequency ω. Periodic heating of the sample takes place within the length $\mu_s = 1/\beta_s$ (physically, optical amplitude has dropped to $1/e^2$ of the initial value). The deposited heat produces a thermal wave (Figure 59b), and the temperature distribution in solid is given by:

$$\theta_s(x,t) = \theta_o \, e^{-|x|/\mu_s} \cos(\omega t + |x|/\mu_s) \qquad (75)$$

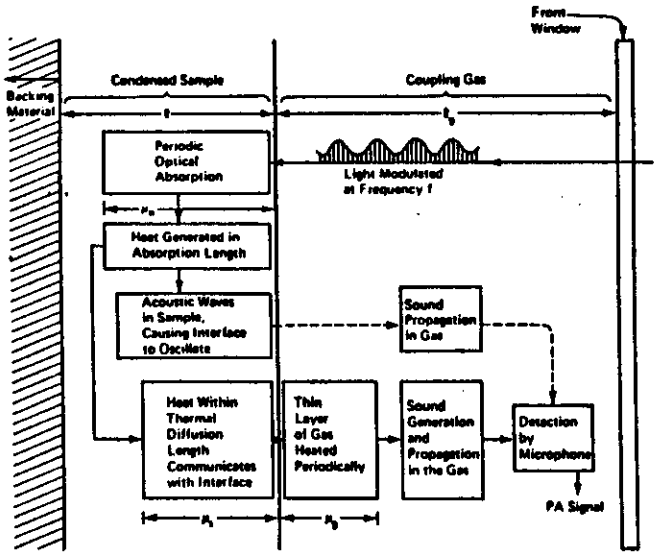

Figure 58. Generation of photoacoustic signal in the solid (2).

satisfying the boundary condition

$$\theta_s(o,t) = \theta_o \cos \omega t \qquad (76)$$

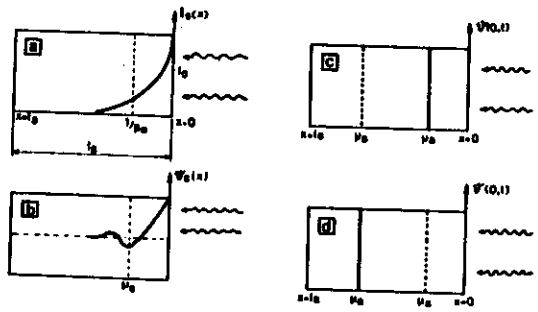

Figure 59. Distribution of optical beam in the solid (a) and the temperature wave (b) modulated surface temperature for $\mu_s > \mu_a$ (c) and $\mu_a > \mu_s$ (d).

satisfying the boundary condition

$$\theta_s(o,t) = \theta_o \cos \omega t \qquad (76)$$

The parameter μ_s is the diffusion length of the sample, that depends on its thermal diffusivity a_s ($m^2 sec^{-1}$) since:

$$\mu_s = \left[\frac{2\,a_s}{\omega}\right]^{\frac{1}{2}} \qquad (77)$$

The 'range' of temperature θ_s (defined as a difference between the maximum and minimum of the thermal wave at given depth) in the sample is

$$\theta_s^r(x) = 2\theta_o \exp\left[-|x|\left(\frac{\omega}{a_s}\right)^{\frac{1}{2}}\right] \qquad (78)$$

and is related to the magnitude of the photoacoustic signal detected in the cell (Figure 60). The coefficient a_s is related to thermal conductivity k_λ^s,

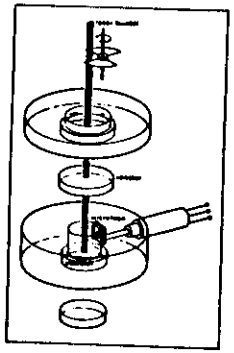

Figure 60. An example of photoacoustic cell for studies on solid samples.

density ρ_s and the specific heat c_s:

$$a_s = k_\lambda^s / \rho_s c_s \qquad (79)$$

Although a_s is a derived quantity, it is an important parameter in heat flow studies, as it determines the rate of transient heat propagation through the sample (81). Equation (77) can now be written as:

$$\mu_s = \left[a_s / \pi f_m \right]^{\frac{1}{2}} \qquad (80)$$

Physically μ_s is a distance at which the thermal wave is considerably damped ($1/e^2$) from its initial value θ_0 at the surface. Hence only waves that originate from depths smaller than one diffusion length μ_s are expected to contribute to the generation of photoacoustic signal by communicating thermally with the gas layer that is μ_g thick. Consequently, this layer will be heated periodically, (expand and cool) thereby producing a pressure wave at the same modulation frequency.

The observed photoacoustic signal is a complex quantity that depends on the absorption coefficient β_s, thermal properties (μ_s, μ_g), modulation frequency ω thermal properties of backing layer (μ_b), the intensity of incoming radiation (the surface temperature θ_0). Relative magnitudes of three relevant sample's lengths, namely diffusion length μ_s, absorption length μ_a, and the physical length L affect the expression of the photoacoustic signal. Rosencwaig analysed various conditions specified below (bracket μ_s, μ_a, L means $\mu_s > \mu_a > L$) and obained the expressions given in Table 10, where factor F is defined as:

$$F = \frac{1}{4\sqrt{2}} \gamma \frac{\mu_g}{l_g} \frac{p_o}{T_o} I_o \qquad (81)$$

(γ is a ratio of specific heats for coupling gas, while p_o and T_o are ambient pressure and temperature of the gas; the factor F is only dependent on gas).

Frequently encountered spectroscopic application of the gas coupling photoacoustics of solid samples is that of non-destructive depth profiling. The basic idea is to vary the thermal diffusion length μ_s by changing the modulation frequency ω. Since the thermal diffusion length is the characteristic 'attenuation length' of the thermal wave, it is possible to connect or disconnect the absorbing centres (or thermal inhomogenities) existing at certain depth from the surface of the solid (2). The efficient thermal coupling between the solid and the gas layer takes place between μ_s and μ_g. Thermal diffusion length μ_s depends on the modulation frequency f_m as $f_m^{-\frac{1}{2}}$: low frequencies will allow the probing of deeper lying layers while high modulation frequency enables the analysis of the subsurface layers.

If the sample is optically thick (β_s is large, thus ($\mu_a = 1/\beta_s$) is short) and besides the physical length of the sample L is much longer than μ_a) $\mu_a << L$, two different situations can occur depending on the magnitude of thermal diffusion length. At low chopper frequencies f_m, μ_s can be made larger than μ_a (as $\mu_s \sim f_m^{-\frac{1}{2}}$): $\mu_s > \mu_a$ i.e. all the heat generated within μ_a communicated with coupling gas. The modulated part of the solid surface

Table 10. Six possible expressions for photoacoustic signal generated in coupling gas (2).

condition	physical situation	photoacoustic signal proportional to
(μ_s, μ_a, L)	thermally thin optically thin	$(1 - i)\beta_s(\mu_b/k_\lambda^b)$ F
(μ_a, μ_s, L)	optically thin thermally thin	$(1 - i)\beta_s(\mu_b/k_\lambda^b)$ F
(μ_a, L, μ_s)	optically thin thermally thick	$-i\ \beta_s\mu_s(\mu_s/k_\lambda^s)$ F
(μ_s, L, μ_a)	thermally thin optically thick	$(1 - i)\ (\mu_b/k_\lambda^b)$ F
(L, μ_s, μ_a)	optically thick thermally thick	$(1 - i)\ (\mu_s/k_\lambda^b)$ F
(L, μ_a, μ_s)	thermally thick optically thick	$-i\ \beta_s\mu_s(\mu_s/k_\lambda^s)$ F

temperature $\theta_s(o,t)$ is not dependent on the absorption coefficient β_s (see Figure 59c) and hence the photoacoustic signal will saturate. Such a case of optically and thermally thick samples ($L > \mu_s > \mu_a$) is very interesting because it offers an opportunity to perform the analysis of the sample in depth. As seen in Table 10, for this situation the photoacoustic signal generated in the coupling gas, does not depend on the properties of the backing material; besides the magnitude of the term $(1-i)(\mu_s/k_\lambda^s)F$ is relatively large when compared to other possible cases in the same table.

By selecting high modulation frequencies f_m, the thermal diffusion length will reduce and it may, by suitable choice be made smaller than μ_a, i.e. $\mu_s < \mu_a$. The magnitude of the photoacoustic signal in this case of thermally thick and optically thick samples, is proportional to the absorption coefficient β_s which (see Table 10) implies that the opaque samples can be studied spectroscopically as well (Figure 59d).

II.8 Depth sampling

The depth profiling by variation of the modulation frequency has been performed on several layered samples. If in addition, the emission frequency of the incident radiation source is being altered, it is possible to record the subsurface distribution of absorbing layers. In such a way the spectra of spinach leaf and apple peel samples have been obtained (82) in the visible region: the authors found clear distinction between the deeper lying layer (~ 35μm) that contains chlorophyll and the top waxy layer (~ 10μm) below the surface.

Hellander et al. (82) studied the leaves of layered india rubber tree, photoacoustically, in 400 to 800 nm visible spectral region, (see Figure 61a) and compared the natural tree leaf to the leaf washed in alcohol and to a chlorophyll extract. The removal of the waxylayer increases the amplitude (curve a) of the photoacoustic signal (in Figure 61) modulation frequency

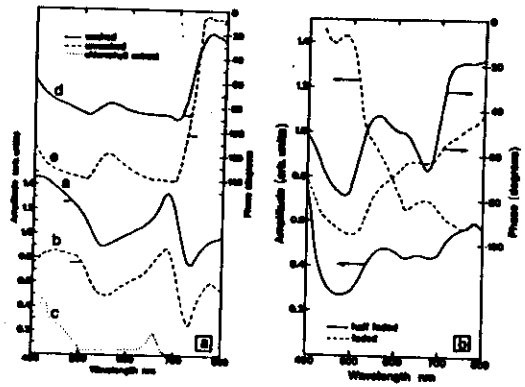

Figure 61a. Amplitude and phase spectra for leaves of india rubber tree: for natural leaf, for leaf washed in alcohol. Also shown is a spectra for an acetone extract of chlorophyll.

61b. Amplitude and phase spectra for a partly faded leaf and a faded leaf (82).

is 113 Hz) compared to intact leaf (curve b), the spectral structure resembles that of the chlorophyll extract (curve c) very much. However, analysis of the phase results shows significant differences at photosynthetically active wavelengths and the infra-red region above 700 nm (curves d and e). This is due to different depth levels at which these wavelengths are being absorbed; i.e. chlorophyll is absorbed at greater depths (below the surface) than the thermal radiation. With the known thermal properties of water it was possible to establish the thickness of the waxy layer (24 microns) as well as to establish that the absorption of chlorophyll layer occurs at about 45 microns deeper than the absorption of the longwave infra-red radiation. Also the proces of leaf lading, characterized by removal of chlorophyll was monitored photoacoustically (Figure 61b) by amplitude and phase delay measurements.

Other experiments involved the determination of depth variation of the colour pigment in the lobster cell (83), and studies on layered structures such as colour negative film (82). At the Ruhr University in Bochum, West Germany, photoacoustics was used to study the depth dependent magnetic properties of multilayered magnetic tapes (84). In biological medical and veterinary practice, this approach was used to investigate metal toxicity on leaves, diffusion of topically applied drugs and water content in the skin (dehydration studies). The experiment is now being prepared in Wageningen to determine non-invasively the amount of lignine content in the membrane of asparagus and artichocke plant in relation to the fibrosity degree.

In recent years non destructive photoacoustic microscopy and imaging have been developed to obtain the information about subsurface irregularities such as thermal or mechanical effects, flaws (2). In principle, the beam of laser (pulsed) or elecron beam radiation is focussed to a small spot. The emission frequency of the laser should be matched to a frequency at which the material is strongly absorbing (see Figure 62). The size of the optical volume V_{op} of the incident beam is determined by the laser spot size and the absorption coefficient of the sample. The absorption of the radiation gives rise to a thermal wave and the diffusion length μ_s will determine the effective thermal volume V_{th}. If the laser is scanned across the sample sur-

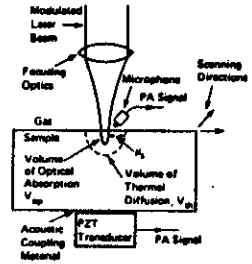

Figure 62. The principle of photoacoustic microscopy (2).

effective thermal volume V_{th}. If the laser is scanned across the sample surface any subsurface defect or abnormality that has a size smaller than V_{op} or V_{th} will affect the optical absorption or thermal properties. These changes can be probed either by gas coupling photoacoustics (detection by microphone or mirage technique in the adjacent gas) or with direct coupling by means of a sensitive piezotransducer in contact with the solid. The subsurface thermal and absorbing microstructures not visually accesssible by optical microscopes, can thus be visualized by the heat waves and the limiting resolution will be determined by the magnitude of V_{th}. The first complete imaging systems ares since recently also commercially available (85, 86).

Complete theoretical analysis for the signal damping and phase delay in layered samples was developed by Hellander et al. (82) in terms of thermal diffusion lengths. For the system (Figure 63) consisting of layer 0 (gas or air), transport layer 1 (sample in condensed phase) and the backing, absorbing layer 2 (solid material). The temperature on the sample - gas interface x = h is given by (62):

$$\theta_s(x=h) = \theta\left[\cosh(h/\mu_1) + \frac{(k_\lambda^1/\mu)_1^2+(k_\lambda^0/\mu_0)(k_\lambda^2/\mu_2)}{(k_\lambda^1/\mu_1)^2(k_\lambda^0/\mu_0 + k_\lambda^2/\mu_2)}\right]\sinh(h_1/\mu_1) \quad (82)$$

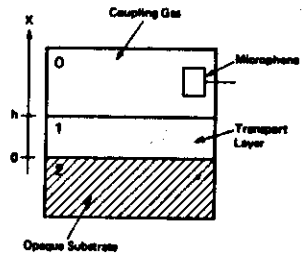

Figure 63. Simple layered structure. The excitation beam can be irradiated from above or underneath (2).

with indices 0,1 and 2 corresponding to the layers (k_λ is not the thermal conductivity squared but the coefficient for layer 2) specified above. The parameter θ is the temperature that is obtained with no transparent layer (h=0), and is given by (62).

$$\theta = [I_o\beta_2/(\beta_2 + \mu_2^{-1})] \cdot (k_\lambda^o/\mu_o + k_\lambda^2/\mu_2)^{-1} \qquad (83)$$

In the above equations μ_1, μ_2 and μ_3 are thermal diffusion lengths in each layer.

The solution of the above equation takes simpler form depending on the relative magnitude of the thermal properties of layers 1 and 2, i.e.

$k_\lambda^1/\mu_1 > k_\lambda^2/\mu_2$ (for most practical applications $k_\lambda/\mu_o << k_\lambda^1/\mu_1$ and k_λ^2/μ_2)

The phase of θ is dependent on the absorption coefficient β_2 of the absorbing layer and the value of k_λ^2/μ_2. For two extreme situations of photoacoustic saturation $\beta_2 >> k_\lambda^2/\mu_2$ i.e. $\mu_s^2 << \mu_2$ the phase is -45° and for $\beta_2 << k_\lambda^2/\mu_2$), i.e. the phase angle becomes -95°(2).

Returning to Figures 59 and 63 representing a transparent solid material placed on top of the opaque backing layer (in case of saturation $L > \mu_s > \mu_s$), the temperature on the sample gas surface is(2).

$$\theta_s(x=h) \sim \text{const } (I_o/\omega^{\frac{1}{2}}) \exp(-h/\mu_s) \cos(\omega t - h/\mu_s - \tfrac{1}{4}\pi) \qquad (84)$$

The photoacoustic signal in gas layer is given by the product of the surface temperature $\theta_s(x=h)$ and the thermal diffusion length of the gas μ_g ($\mu_g < l_g$). The amplitude of the photoacoustic signal S_{PA} and the phase ψ_{PA} are (2):

$$S_{PA} \sim \omega^{-1} \exp[-h\omega^{\frac{1}{2}}/(2a_s)^{\frac{1}{2}}] \qquad (85)$$

and

$$\psi_{PA} = -h\omega^{\frac{1}{2}}/(2a_s)^{\frac{1}{2}} - \tfrac{1}{4}\pi \qquad (86)$$

In orcer to find the thickness h of the layer h of known a_s one measures the S_{PA} at a set of frequencies ω and makes a semilogarthmic plot of $S_{PA} \cdot \omega$ versus the modulation frequency ω. The value of h/a_s is then obtained from the slope of the plot. Alternatively, one can plot the phase lag ψ_{PA} versus $\omega^{\frac{1}{2}}$ and obtain $h/a_s^{\frac{1}{2}}$ from the slope of the straight line (Figure 64). The linear relationship between the ψ_{PA} and $\omega^{\frac{1}{2}}$ is valid (2) for a range of h/μ_s not larger than 0.3.

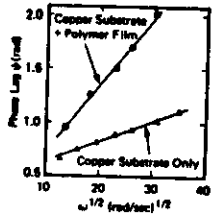

Figure 64. The plot of phase lag Ψ_{PA} versus $\omega^{\frac{1}{2}}$ for uncoated and polymer coated copper substrate. The thickness of the layer can be found from the slope of the diffusivity is known (2).

II.9 Thermal diffusivity

Alternatively one can determine the diffusivity of the sample photoacoustically by phase analysis of the photoacoustic signal. The periodically modulated (ω) optical excitation beam (Figure 64) will reach maximum in the absorbing sample at time intervals given by $\cos \omega t_{opt} = 2n\pi$ with (n=1, 0, 1, 2, 3 etc.) i.e. $t_{opt} = \frac{2n\pi}{\omega}$. On the other hand, the thermal wave in the transparent sample will have maximum (given by $\cos [\omega_{th} - x(\omega/2a_s)^{\frac{1}{2}}] = 2n\pi$. The time lag Δt between the time instants corresponding to maxima of thermal and optical wave at some distance x will then be:

$$\Delta t = \frac{x}{2} \cdot \left[\frac{T}{\pi a_s}\right]^{\frac{1}{2}} \qquad (87)$$

where T represents the period of the modulation $T = 1/f_m$. This time lag is independent of the surface temperature and hence of the incident radiation. The time lag is related to the phase shift $\Delta\phi$ simply through $\Delta\phi = 2\pi \frac{\Delta T}{T}$. Thus by measuring the phase shift (by lock-in amplifier) at certain modulation frequency f_m (thus also specified period T) it is possible to construct the graph Δt versus $T^{\frac{1}{2}}$ (see eqn. (87)) for a solid material with a given a_s. The slope V of the linear plot which is equal to $V = \frac{x}{2}\left[\frac{1}{\pi a_s}\right]^{\frac{1}{2}}$ from eqn. (87) can be used to calculate the thermal diffusivity a_s (Figure 65) from:

from: $$a_s = (\frac{x}{V})^2 \cdot \frac{1}{4\pi} \, . \qquad (88)$$

Although simple, this approach yields very good agreement with results obtained with other methods used to determine thermal diffusivity for a variety of solid materials. Adams and Kirkbright (81) studied spinach leaf

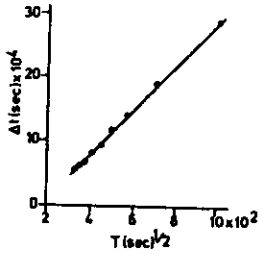

Figure 65. Plot of time lag Δt versus the period of modulation frequency T obtained with glass samples (81).

as layered inhomogenous sample. Upper cuticle layer and the chloroplast layer have different electronic absorption spectra. Contrary to the pigmented layer the cuticle layer is transparent to the optical radiation. Hence the photoacoustic spectra of the two relevant layers are presented at different phase angles relevant to the modulated optical wave.

II.10 Thermal effusivity

When two semi-infinite, homogenous and isotropic solid bodies 1 and 2 (each specified by its density, thermal conductivity and specific heat) at two different initial temperatures θ_1 and θ_2 are brought in contact, the temperature θ_m at the interface of two bodies will be

$$\theta_m = \frac{\sqrt{(k_\lambda \rho c)_1}\ \theta_1 + \sqrt{(k_\lambda \rho c)_2}\ \theta_2}{\sqrt{(k_\lambda \rho c)_1} + \sqrt{(k_\lambda \rho c)_2}} \qquad (89)$$

This 'contact' temperature is dependent on the relative magnitudes of the square root of the product k, ρ and c. The physical quantity $\sqrt{k\rho c}$ is called the thermal effusivity and plays an important role in time dependent surface processes as it relates the heat flux $F_s(t)$ to the surface temperature $\theta_s(t)$ and vice versa (88). If $F_s(t)$ is known, the time dependent surface temperature $\theta_s(t)$ can be found from

$$\theta_s(t) = \frac{1}{\sqrt{(k_\lambda \rho c)_s \cdot \pi}} \int_0^t d\tau \, F_s \, (t - \tau)/\tau^{\frac{1}{2}} \qquad (90)$$

Inversely, for the known temperature the power $F_s(t)$ deposited per unit surface in the solid medium is (88)

$$F_s(t) = \sqrt{\frac{(k_\lambda \rho c)_s}{4\pi}} \left[\int_0^t d\tau [\theta_s(t) - \theta_s(\tau)]/(t - \tau)^{3/2} + \right.$$

$$\left. + 2 \, [\theta_s(t) - \theta_s(o)/\sqrt{t}] \right] \qquad (91)$$

Thermal effusivity $\sqrt{(k_\lambda \rho c)_s}$ appears in both equations as a dominant material parameter. The photoacoustic spectroscopy in frequency domain allows direct determination of the thermal effusivity without a need to calculate it indirectly from literature parameters.
Furthermore, the values $\sqrt{k_\lambda \pi c)_s}$ obtained experimentally by photoacoustic measurements are indeed effective ones taking into account the sample's porosity and the roughness condition of the surface.
Bein et al. (88) showed that at the solid (s)- gas (g) interface shown in Figure 66, the modulated component $\delta_{p(t)}$ of the pressure $p(t) = \bar{p} + \delta p(t)$ in the limiting case (when $\ell_s \to \infty$ (semi-infinite solid) and the effusivity $\sqrt{(k_\lambda \rho c)_g}$ of the gas is much smaller than that of the sample) can be calculated as follows (88)

$$\delta p(t) = C(\omega) \frac{I_0}{\omega} \exp(i\omega t) \, F(\gamma, \ell_g, k_\lambda^g, \rho_g, c_g) \cdot \frac{\eta_s}{\sqrt{(k_\lambda \rho \, c)_s}} \cdot$$

$$\cdot \frac{1}{(1 + \sigma_g/\beta_g)} \qquad (92)$$

where σ_g is the complex quantity defined as $\sigma_g = (1 + i)/\mu_g$.

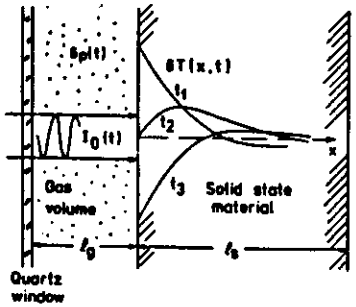

Figure 66 The periodic oscillation δp(t) are taking place in the gas layer (88).

In eqn. (92) $C(\omega)$ represents characteristic response of detection (amplitude and phase) equipment. Since it is only modulation frequency dependent $C(\omega)$ can be eliminated from above equation by performing the measurement on the reference sample as well. Likewise the term F in the above equation contains physical quantities that are representative for the coupling gas and could, just as $C(\omega)$, be taken care of by comparison with a reference sample.
Symbol η_s $(o < \eta_s < 1)$ was introduced to account for the sample's heat conversion efficiency for the incident radiation. The complete expression for normalized photoacoustic amplitude S_{PA} which is obtained by rationing the corresponding amplitudes S^r_{PA} and S^s_{PA} observed with reference and sample is:

$$S_{PA} = \frac{S^r_{PA}}{S^s_{PA}} = \left[\frac{\eta_r}{\eta_s}\right] \sqrt{\frac{(k_\lambda \rho \, c)_s}{(k_\lambda \rho \, c)_r}} \cdot \left[\frac{1 + \sqrt{\frac{2\omega}{a_s \beta_s^2}} + \frac{\omega}{a_s \beta_s^2}}{1 + \sqrt{\frac{2\omega}{a_r \beta_r^2}} + \frac{\omega}{a_r \beta_r^2}} \right]^{\frac{1}{2}}$$

It is convenient to use the reference solid material with the absorption coefficient β_r much smaller than β_s, because for this case the above equation reduces to (88):

$$S_{PA} \cdot \left[\frac{1}{\sqrt{f_m}}\right] = \left[\frac{\eta_r}{\eta_s}\right] \cdot \sqrt{\frac{(k_\lambda \rho\, c)_s}{(k_\lambda \rho\, c)_r}} \cdot \sqrt{\frac{a_r}{2\pi}}\ \beta_r \cdot \sqrt{\frac{1}{f_m}} \cdot \left[1 - \frac{1}{\sqrt{2}}\sqrt{\frac{a_r}{\pi}}\ \frac{\beta}{t}\ \frac{1}{\sqrt{f_m}}\right] \quad (34)$$

As all parameters of the solid reference sample are known and the ratio of conversion efficiencies can be determined by the series of separate measurements (87), it is possible to make a plot of the photoacoustic signal versus $f_m^{-1/2}$, and from this to calculate the thermal effusivity of the sample.

Figure (67) shows the scheme of the Argon ion laser experimental set-up

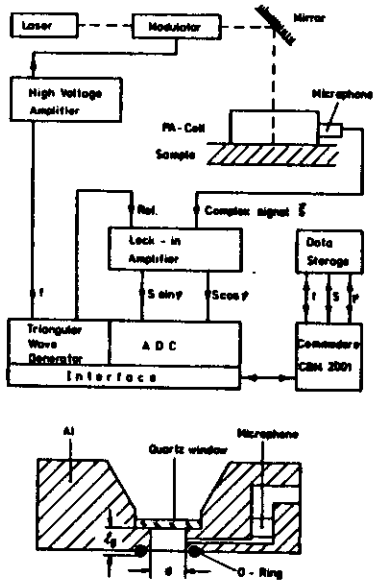

Figure 67. An experimental set up used for measurement of thermal effusivity by frequency domain photoacoustic spectroscopy (87, 88).

used by Krüger et al. (87) at the Ruhr University in Bochum to measure the effusivity of the graphite plate (absorption coefficient $\beta_s = 2 \times 10^5\ cm^{-1}$) Diameter c of the photoacoustic cell (shown below) is 8 mm and the height l_g (equal to the diffusion length in gas) is 6 mm. Microphone is separated from the gas volume by a 1.2 mm diameter and a 15 mm long channel in order to prevent the diffuse light from reaching the membrane. Using the same apparatus the thermal effusivities of various greenhouse glasses have been determined recently (89). The glass material with low $\sqrt{k_\lambda \rho c}$ is preferred as the greenhouse cover material. Typical plot of S_{PA} ($\sqrt{f_m}$) versus ($1/\sqrt{f_m}$) is shown in Figure 68 for a normal borosilicate glass (coated with 20 $\mu g/cm^2$) termed X6A. As the reference sample neutral glass N91 with $(k_\lambda \rho c)^{1/2} = 1480$

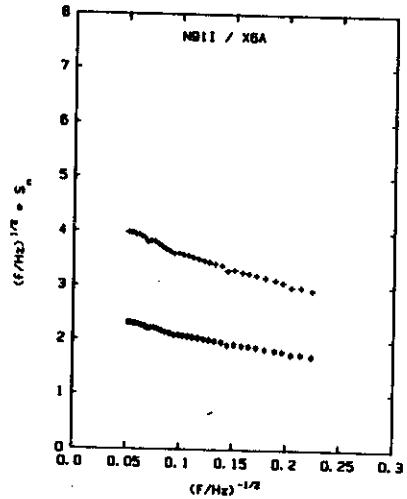

Figure 68. The product of photoacoustics amplitude and $f_m^{1/2}$ plotted versus $f_m^{-1/2}$ for glass X6A. The upper curve (++) is uncorrected and the lower curve is corrected for ratio of heating conversion efficiencies (89).

$W\ m^{-2}K^{-1}sec^{\frac{1}{2}}$, $a_r = 5.3 \times 10^{-7} m^2 sec^{-1}$ and $\beta_r = 91\ cm^{-1}$. The curve indicated by ++++ signs represents S_n / f_m plotted versus $(1/f_m^{\frac{1}{2}})$ while **** trace refers to the same curve but now corrected for the ratio of heat conversion factors, i.e. $S_n / f_m \left(\frac{\eta_s}{\eta_r}\right)$ is plotted versus $(1/f_m)^{\frac{1}{2}}$. For this specific glass (η_s/η_r) is 0.58 which gives $\sqrt{(k_\lambda \rho c)_s} = 1390\ W\ m^{-2}\ K^{-1}\ sec^{\frac{1}{2}}$. This technique also enables the studies of special purpose coated greenhouse glasses. The data obtained are useful when total energy balance of such agricultural object is being considered.

II.11 Some applications to plant matter

Although the photoacoustic spectra of spinach leaf (81) and phytoplankton indicated potential usefulness of this technique, true application to the plant science was initiated by the work of Cahen's group at Weizman Institute of Technology, Rehovot Israel some eight years ago (90). Photochemical changes affect the photoacoustic signal because the quantum efficiencies for these two processes are complementary (light energy absorbed = heat energy released + photochemistry) if other non-radiative relaxation channels are excluded. Cahen et al. observed that the photoacoustic spectrum and the optical spectrum for a photosynthesis active sample (lettuce chloroplast) differ by some amount due to the storage of the part of the absorbed energy in the form of a chemical energy during each modulation cycle.

The photoacoustic signal is proportional to the incident light energy minus the energy stored by a photochemical process. Hence the loss in photoacoustic signal is proportional to the amount of stored chemical energy per modulation cycle. The dependence of the photoacoustic signal and the relative photochemical loss on the modulation frequency $\omega = 2\pi f_m$ is shown in Figure 69 below. Only those intermediates that did not decay during one modulation cycle are relevant in the generation of heat. The intermediate that is being sensed must live 'longer' than the period of the modulation in order to be detected. On the other hand, a build-up time of the intermediate product must be much shorter than the inverse of the modulation frequency.

Consequently by varying the modulation frequency f_m, early (late) intermediates will be detected at high (low) frequencies, making the kinematic study possible (91).

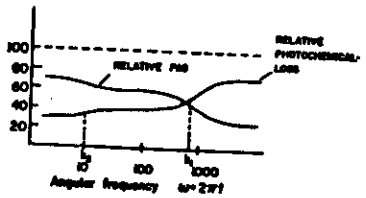

Figure 69. Photoacoustic signal and the photochemical loss as a function of modulation frequency (93).

In addition to the determination of efficiency of the energy conversion of light into heat (and thus indirectly also the efficiency of the conversion of light into chemical energy) it is also possible to use photoacoustics to to probe the gas exchange mechanism in leaves. Canaani (92) showed that the same can be done for lichens and layered algae.

Consider the figure shown in Figure 70 obtained with a tobacco leaf. After being kept in darkness for some time the leaf is irradiated with a modulated optical light of (wavelength 680 nm, intensity 14 W/m^2) over wide frequency range. The photoacoustic signal is measured as a result of non-radiative processes (heating plus the photochemistry and other mechanisms). At low frequency f_m (35 Hz for example) exposure of the leaf to the optical radiation results in a fast increase of photoacoustic signal shortly after the onset time. This is followed by a period of additional, less pronounced increase before the stationary level has been reached after about 2 minutes. At high modulation frequency (292 Hz for example) after initial fast increase, the photoacoustic signal decreases which is due to the expected photosynthesis process (that causes the increase of photochemical loss and hence the decrease of the photoacoustic signal).

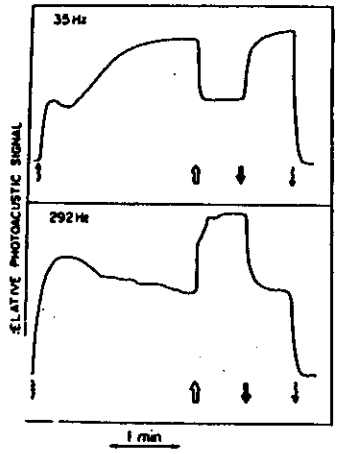

Figure 70. Irradiation of photoacoustic signal obtained from tobacco leaf as a function of time at two modulation frequencies. Wavy arrows indicate the onset and offset of modulated light, while the straight arrows refer to the saturation background light (92).

The differences in the signal-time dependence observed within the first two minutes in the above figure is explained by the effect of oxygen gas evolution that accounts for transport of oxygen from chloroplast to the gas phase. This proces is slow and therefore it can be detected only at low f_m values.

When, after two minutes time, the sample is additionally illuminated with a strong d.c. (unmodulated) light (340 W/m²) source of the same wavelength, two different phenomena are seen. At high modulation frequency (292 Hz) the leaf shows 'normal' pattern i.e. the background d.c. light saturates the photochemical route and all the energy absorbed by the leaf will be released as heat. However, this background light does not affect the nature of the modulated photoacoustic signal. Consequently, saturation of photochemical route means the saturation of chemical loss as well, and therefore the signal is expected to increase. At low frequency (35 Hz) the same

amount of background light produces the opposite effect: the signal decreases which is consistent with the fact that the rate of gas evolution at saturation level, does not vary with light intensity. From the two contributions to the photoacoustic signal (modulated heat and modulated gas exchange) the second mechanism will be eliminated by the background saturation light and the signal will decrease.

Excellent reviews describing the application of photoacoustic spectroscopy to plant science have appeared (94) or are due to be published (92).

Havaux et al. (95, 96) studied the effects of rapid water stress and the effects of leaf dehydration on the photochemical activity, and showed the photoacoustic inhibition as well as the anatomical modifications (evident by modified oxygen evolution and heat diffusion). The experiment was later extended to study (in vivo) the photosynthetic response due to stress in leaves by slowly developing water deficit (Figure 71) in tobacco plants. This was achieved by withholding the water from the soil over several days.

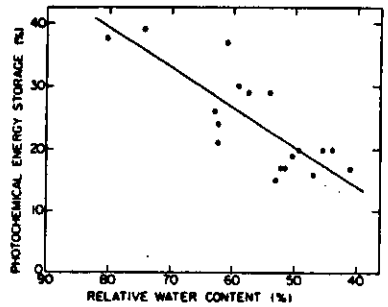

Figure 71. Photochemical energy storage is affected by the water stress produced in the plant (96).

Other photoacoustic experiments used as a diagnostic tool to assess the plant condition, photosynthesis and productivity were carried out (97). These involve the comparison of photoacoustic data collected with different

plants of the same species ("variability test") and the studies of the effect of excessive heat pretreatment. Photoacoustic technique also allows rapid measurements of the effect of photoinhibition on the photosynthesis. Likewise, the speed of response of the plant adaptation to high light intensities can be determined photocacoustically. The effect of soil salinity (25-100 mM NaCl) on the growth and photosynthesis in grapes (Vinis vinifera) has been studied in an attempt to establish the salt tolerance of the plant (97). Reduction of photosynthetic activity by 25% was observed at the largest salinity value. Another useful application of photoacoustics is to study the effect of the environmental "chilling stress" on the agriculturally important plants. For example tomato is a plant that is very sensitive to chilling (injuries in growing zones or yield reduction). This fact imposes restrictions on the length of the growing season as well as on the latitudinal distribution. Therefore efforts are being made to breed a new sort with increased chill resistance (97). Photoacoustic experiments have established that chilling in the dark has much smaller effect on the photosynthesis in tomato than chilling accompanied by large light fluxes (this last fact is due to the reduced quantum yuield of CO_2 uptake caused by photoinhibition). Worthwhile mentioning, is the series of anticipated photoacoustic experiments to study the photosynthesis in Papaya, corn, cotton, pea and other plants at various growth conditions (97). In particular little is known about the leaf ontogesis in Papaya. The knowledge of plant response to various stress factors gained through the photoacoustic measurement is useful as a convenient diagnostic tool and enables one to take decisive precautional measures. Cahen (97) investigated the feasibility of photoacoustic technique in detecting stress conditions in plants caused by the diuron and atrazine herbicides. The kinematics of herbicide penetration was monitored when the plant was sprayed directly and compared to the situation characterized by herbicide treatment through the root system (irrigation). Although the pea plant appears normal several days after the diuron irrigation treatment, its photosynthetic activity is reduced considerably (Figure 72).

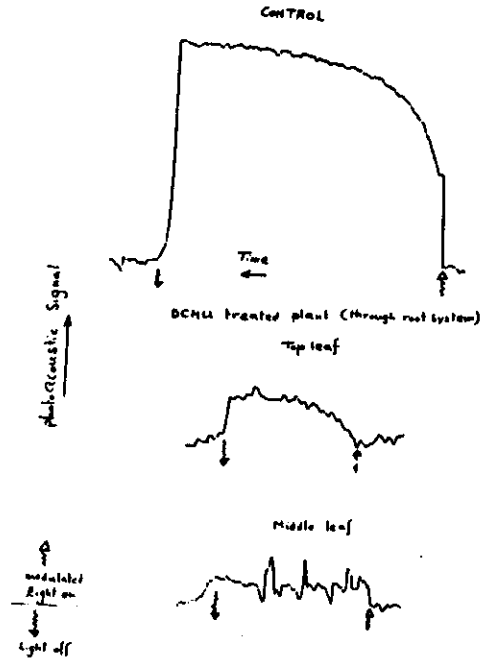

Figure 72. A 40 hours effect of diuron herbicide on the photoacoustic signal observed on leaf pea plant. concentration of 5×10^{-5}M of inhibitor was used and applied through the root (97).

II.12 Olfactory psychophysics

Psychophysics is a new branch of psychology and relates the physical stimulus to the psychological response. One specific physical stimulus is the concentration of the odorant in the ambient air. The psychophysical response is measured in a number of different ways so that ultimately a psychophysical function (Figure 73) is obtained that relates the perceived (sniffing) odor intensity R to the stimulus concentration C_i (each odorant being specified by specific values of k and n constants) through the power law (98):

$$R = k\, C_g^n, \text{ or } \log R = \log k + n \log C_g \qquad (95)$$

Once the psychophysical function is known, it can be used to practical advantage in mesuring the abatement of odor pollution (malodors found in manure, air pollution) or control of odor (perfume for example, tobacco and deodorant industries).

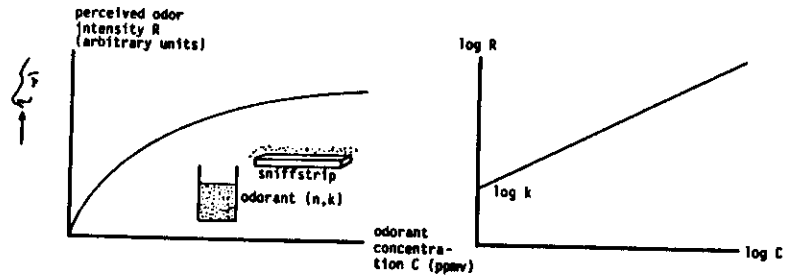

Figure 73. The psychophysical function for an odorant (98).

Two most frequently used methods in odor (threshold) experiments are: olfactometry and the sniffing. The first method is based on diluting the saturated vapour of solid odorant in air to a desired gaseous concentration and presenting the flowing mixture to a human subject.
A drawback of olfactometry is the difficulty (low vapour pressure) associated with preparing concentrations accurately at room temperature.
Sniffing implies exposure of human subject to a 'sniff bottle' containing the liquid odorant in an odorless liquid. The odor sensation is provoked in the brain upon evaporation of the odorant from the liquid to the gas phase and the passage of odorant molecules across the olfactory epithelium. Raoult's law relates the odorant's partial vapour pressure to the odorant concentration in the liquid phase. In practice deviations of Raoult's law are observed (99).

Both methods described above have in common that measurements of the perceived odor intensity R and the concentration are not taken simultaneously. The photoacoustic technique posses both, high sensitivity and the speed of response. There is a good coincidence with the CO_2 laser emission lines (100) for small perfume molecules.

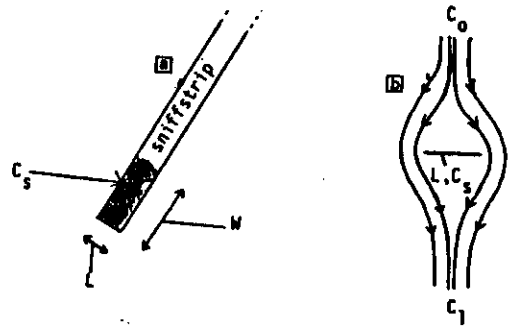

Figure 74. The sniffstrip (a) and geometry (b) of the air flow around the strip (99).

When a sniffstrip with LxW (Figure 74a) being the surface area, wetted by the liquid odorant, is held in air flow ϕ_V ($m^3 sec^{-1}$), the evaporation takes place. The concentration C_g of pure odorant in the air is determined by the saturated vapour concentration C_s (kg m^{-3}) of the odorant on the sniffstrip surface and the initial concentration of the odorant C_o in the air (99):

$$C_g = C_o + L\, W\, k^o\, C_s / \phi_V \qquad (96)$$

where k^o($m\ sec^{-1}$) is the parameter that depends on the air velocity v at the surface, kinematic viscosity ν of air, diffusion coefficient of the odorant D* and length L. This dependence is described by dimensionless

relationship (99):

$$k^{o}L/D^{e} = f(\frac{v\,L}{\nu}, \frac{\nu}{D^{e}}) = C\,Re^{n}Sc^{m} \qquad (97)$$

with Re and Sc being Reynolds and Schmidt numbers (99). The saturated concentration C_s is dependent on temperature τ and the molecular constants A, B and E of the odorant:

$$C_s = \frac{10^{[A - B/(E + \tau)]}}{(273.14 + \tau)} \cdot 0.36 \times 10^{6}\ \text{ppmv} \qquad (98)$$

For the given (Figure 74b) flow around the surface of the sniffstrip C = 0.57, n = 0.5 and m = 0.33. The air flow around the surface is chosen approximately equal to the inhalation rate of the natural sniffing pattern of the human (0.5 liters per second). This flow corresponds to air velocity of about 5 m sec^{-1} over the L x W area (for typical strip size L = 7 mm, W = 14 mm).

III REFERENCES

1. BICANIC, D.D.; Technogida Spectrometrie 2, Stam Tijdschriften, The Hague (1986).
2. TAM, A. in Kliger, D. (Ed.); "Ultrasensitive Laser Spectroscopy", Academic Press, New York (1983).
3. BELL, A.G.; Phil. Mag. 11, 510 (1881).
4. ZHAROV, V.P. and Lethokov V.S.; "Laser OpToacoustic Spectroscopy" Springer Series in Optical Sciences, Vol. 58, Springer Verlag Heidelberg (1986).
5. ADAMOWICZ, R.F. and Koo, P.K.; Appl. Opt. 18, 2938 (1979).
6. KERR, E.L. and Atwood, J.G.; Appl. Opt. 7, 915 (1968).
7. KREUZER, L.B.; J. Appl. Phys. 42, 2934 (1971).
8. TAM, A.C.; Rev. Mod. Phys. 58, 381 (1986).
9. ROSENCWAIG, A.; "Photoacoustics and photoacoustic spectroscopy". John Wiley, New York (1980).
10. GEDROVICS J.; University of Riga, to be published (1987).
11. LETHOKOV, S.V.; "Laser Analytical Spectroscopy", Mir. (1986) (In Russian).
11a. SIGRIST, M.W.; J. Appl. Phys. 60, R83 (1986).
12. DICKER, E; M.Sc.Thesis, Catholic University Nijmegen (1985).
13. ROSENGREEN, L.G.; App. Opt. 14, 1961 (1975).
14. DEWEY, F.D.; Opt. Eng. 13, 483 (1974).
15. PATEL, C.K.N.; Bell Telephone Labs, Murray Hill, N.Y. USA, Priv.-Comm. (1987).
16. PATEL, C.K.N.; Science 202, 157 (1978).
17. BICANIC D.D. and Harren, F.; Anal. Instr. 15, in press (1987).
17a. ANDERSON, P. and Persson, V.; Appl. Opt. 23 192 (1984).
17b. LOPER, G.L. et al.; Appl. Opt. 21, 1648 (1982).
17c. AHLBERG, H. et al.; Appl. Opt. 23, 2902 (1984).
17d. MAYER, A. et al.; Appl. Opt. 17, 391 (1978).
17e. JOVICEVIC, S. et al.; Spect. Lett. 14, 415 (1981).
18. HUBERT, M.H.; Report Ultra Laser Tech. 83-75-1. Mississauga, Canada (1983).

19. LOPER, G.L. et al.; Report prepared for Industrial Environmental Research Laboratory, Environmental Protection Agency, Washington D.C. (1985) Contract 68-03-3171.

20. BECK, S.M. et al.; Report prepared for Environments: Protection Agency Research Triangle Park, N.C. USA, contract number 68-03-3171 (1986).

21. KRAFT, G.H. and Revan, J.W.; Infr. Phys. 21, 337 (1981).

22. VEEKEN, K.; Ph. D. Thesis, Catholic University Nijmegen (1985).

23. SHTRIKMAN, S. and Slatkine, M.; Appl. Phys. Lett. 31, 830 (1977).

24. SIGRIST, M.; ETH Swiss Federal Inst., Zurich. Priv. Comm. (1986).

25. BRUNNER, W. and Junge K.; "Laser-Eine Einfürung", Chapter 3, Hüthig Verlag, Heidelberg (1984).

26. HARREN, F. et al.; Proc. ECOSA Conference Firenze (Italy) (1986) (in press).

27. WRIGHT, W.M. and Stedman, D.H.; Proc. Conf. Acoust. Soc. (USA) Atlanta, Ga. (1980).

28. BERNEGGER, S.,; ETH Swiss Fed. Inst. Zurich, Priv. Comm. (1987).

29. SIGRIST, M. et al.; Proc. Conf. on Diode Lasers and Air Pollution Monitoring. Freiburg, W-Germany (1986).

30. WOLTERING, E.J. et al.; Bedrijfsontwikkeling 15, 980 (1984).

31. WOLTERING, E.J.; Gärtner Rörs und Gartenwelt 85, 1303 (1985).

32. WOLTERING, E.J. and Boerrichter H.; in: "Snijbloemen - kwali-ejte-behoud in afzet keten" Sprenger Instituut, (1986).

33. AIR QUALITY CRITERIA FOR HYDROCARBONS; US Dept. of Health, Education and Welfare Washington (1970).

34. WOLTERING E.J. and Harren F.; to be published (1987).

35. MOOI, J.; Der Forst und Holzwirt, 39, 438 (1984).

36. MOOI, A. and Zalm, A.J. v.d.; Research Rep. EEC-EVN-672-NL. IPO, Research Institute for Plant Protection, Wageningen (1986).

36a. WOLTING, H.G.; Acta Horticul. 174, 351 (1985).

37. POSTHUMUS, A.C. et al.; Bedrijfsontwikkeling 15, 429 (1984).

38. POSTHUMUS, A.C.; Natuur en Techniek, 494 (1981).

39. TONNEIJCK, A.E.G. and Floor H.; Bedrijfsontwikkeling 15, 440 (1984).

40. KOZIOL, M.J. and Whatley, F.R.; "Gaseous Air Pollutant and Plant Metabolism", Butterworths, London 1982.

41. KOCH, K.P. and Lachmann, W.; Appl. Phys. Lett. 32, 289 (1978).

42. JOHNSON, S.; Anal. Proc. 323, 1 (1986).

43. Product Information Booklet; Institute for the Storage and Processing of Agricultural Produce, Wageningen (1986).

43a. VAN ES, A. and Hartmann, K.J. Institute for the the Storage and Processing of Agricultural Produce, Wageningen, Priv. Comm. (1987).

44. LAAR, A.J.M. van der; M.Sc. Thesis. Agricultural University of Wageningen (1987).

45. DAINTY, R.H., Hibbard, C.M.; J. Appl. Bacter. 48, 387 (1980).

46. DAINTY, R.H., Edwards, R.A., Hibbard, C.M.; J. Appl. Bacter.57, 75 (1984).

47. DAINTY, R.H. et al.; AFRC Meat Research Institute Langford, Bristol U.K., Priv. Comm. (1986).

48. JONG, T. de; Ph.D. Thesis, Agricultural University, Wageningen, to be published (1989).

49. BICANIC, D.D. and Bizzarri, A.; to be published (1987).

50. GUREVICH, V.G. et al.; Izmeritel'naya Tekhnika 5, 51 (1985) (in Russian).

51. GERLACH, R. and AMER, N.M.; Appl. Phys. 23, 319 (1980).

52. GERLACH, R. and AMER, N.M.; Appl. Phys. Letts. 32, 228 (1978).

53 KREUZER, L.B.; Anal. Chem. 50, 596A (1978).

54 ZHAROV, V.P. et al.; Jour. Mol Struct. 115, 261 (1984).

55. ZHAROV, V.P.; in: "Laser Analytical Spectrochemistry" (edit. V.L. Lethokov), A. Kliger, Boston and Bristol (1986).

56. KOROBELNIK, G.S. et al.; Sov. Jour. Quant Elek. 15, 68 (1985).

57. ZHAROV, V.P.; Sov. Phys. Dok. 28, 335 (1983).

58. KLIJNSTRA, J.W.; Dept. of Animal Physiol. Agricult. University, Wageningen. Priv. comm. (1987).

59. KRAAN, G. van der et al.; in: "Integrated control of insect pests in the Netherlands". PUDOC, Wageningen (1980).

60. RITTER, F.J. and Persoons, C.J.; in: "Integrated control of insect pests in the Netherlands". PUDOC, Wageningen (1980).

61. WOHLERS, P. and Tjallingii, W.F.; Dept. of Animal Phys. Agricult. University. Wageningen, Priv. Comm. (1987).

62. LEPOUTRE, P. and POULET, J.P.; Proc. Symp. on Laser Photoacoustics, Paper 5, Wageningen (1986).

63. STRAUSS, E.; Proc. Symp. on Laser Photoacoustics, Wageningen (1986).

64. KUYPERS, A.D.; M.Sc. Thesis, Free University, Amsterdam (1985).

65. PATEL, C.K.N., and Tam, A.; Rev. Mod. Phys. 53, 517 (1981).

66. STRAUSS, E.; University of Oldenburg, West-Germany, Priv. Comm. (1986).

67. KITAMORI, T. et al.; J. Appl. Phys. 58, 268 (1985).

68. KITAMORI, T. et al.; J. Appl. Phys. 55, 4005 (1984).

69. TAM, A.C. and Patel, C.K.N.; Appl. Opt. 18, 3348 (1979).

70. FANG, H. and Swofford, L.; in: "Ultrasensitive Laser Spectroscopy", Kliger (Ed.) Academic Press (1983).

71. BICANIC, D.D. et al.; Appl. Phys. A in press (1987).

72. Product Guide. General Analytical Corp. Norwalk, Ct. (USA) (1986).

73. WILKS, P.A.Jr.; General Anal. Corp. Norwalk, Ct. (USA) Priv. Comm. (1986).

74. NORDAL, P.E. and Kanstad, S.O.; Opt. Comm. 24, 95 (1978).

75. WEIMER, W.A. and Dovichi, N.J.; Appl. Phys. 59, 225 (1986).

76. DOVICHI, N.J. and Harris, J.M.; Anal. Chem. 52, 2338 (1980).

77. NOLAN, T.G. and Dovichi, N.J.; in press (1987).

78. DOVICHI, N.J. et al.; Anal. Chem. 56, 1700 (1984).

79. NORDE, W.; Advances in Colloid and Interface Science 25, 267 (1986).

80. FOURNIER, D. and Boccara, A.C.; In: "Photoacoustic Effect". Coufal et al. (Eds.).Viewieg, Braunschweig (1984).

81. ADAMS, M.J. and Kirkbright, G.F.; Spec. Letts. 9, 255 (1976).

82. HELANDER, P. et al.; J. Appl. Phys. 52, 1146 (1981).

83. MACHENTUM, R. et al.; Nature 279, 265 (1979).

84. PELZL, J.; Proc. Symp. on Laser Photoacoustics, Wageningen, 1986.

85. RYAN, T.; Product Catalogue, EDT, London, (1986).

86. McCLELLAND, J.F.; Product Catalogue, MTEC Photoacoustics Inc. Ames, Iowa, (USA) (1987).

87. KRÜGER, S.. Diploma Arbeit. Ruhruniversität Bochum (1986).

88. BEIN, B. et al.; J. Nucl. Mat. 128, 945 (1984).

89. KRÜGER, S. and Bicanic, D.D.; to be published (1987).

90. MALKIN, S. and Cahen, D.; Photochem. Photobiol. 29, 803, (1979).

91. BULTS, G.; Biochim. Biophys. Acta 679, 452 (1982).

92 MALKIN, S. and Canaani, O.; Review, submitted for publ. Physiologia Plantarum (1987).

93. BULTS, G. Proc. Symp. on Laser Photoacoustics Wageningen (1987).

94. BRASLAWSKY, S.; in: "Primary Processes in Biology and Medicine", Bensasson, R.V. et al. (Eds.), Plenum Publishers (1985).

95. HAVAUX, M. et al.; Plant Physiol. 82, 827 (1986).

96. HAVAUX, M. et al.; Plant Physiol. 82, 834 (1986).

97. CAHEN, D.; Weizmann Inst. of Science, Rehovot, Israel, Priv. Comm. (1987).

98. BICANIC, D.D. and Schiet, F.T.M.; Proc. 4th Topic Conf. on Photoacoustics, Montreal (1985).

99. SCHIET, F.T.M.; M.Sc. Thesis, Agricultural University Wageningen (1986).

100. BICANIC, D.D. and Schiet, F.T.M.; Chem. Senses 10, 252 (1985).